

Aus der Klinik für Diagnostische und Interventionelle Radiologie
des Universitätsklinikum Heidelberg

Ärztlicher Direktor: Prof. Dr. med. Hans-Ulrich Kauczor

OPTIMIZATION AND STANDARDIZATION OF COMPUTED
TOMOGRAPHY PERFUSION AND DEVELOPMENT OF
LOW RADIATION EXPOSURE CT PERFUSION
ALTERNATIVE FOR CLINICAL APPLICATIONS IN
ONCOLOGIC IMAGING

Inaugural dissertation
zur Erlangung des Doctor scientiarum humanarum (Dr. sc. hum.)
an der
Medizinischen Fakultät Heidelberg
der
Ruprecht-Karls-Universität

vorgelegt von

NEHA VATS

aus

Haryana, India

March, 2024

Dekan: Herr Prof. Dr. Michael Boutros
Doktorvater: Herr Prof. Dr. med. Hans-Ulrich Kauczor
Doktorandenberater: PD Dr. sc. hum. Wolfram Stiller
Betreuer: Dr. sc. hum. Stephan Skornitzke

The only thing standing between you and your goal is the story you
keep telling yourself as to why you can't achieve it.

Jordan B. Peterson

Contents

Abbreviations	viii
List of Figures	ix
List of Tables	xi
1 Introduction	1
1.1 Pancreas	1
1.2 Pancreatic tumors	2
1.3 Diagnostic methods for pancreatic tumors	3
1.4 Computed Tomography (CT)	4
1.4.1 Principle	5
1.4.2 Image reconstruction	6
1.4.3 Type of CT imaging techniques	7
1.5 CT perfusion	7
1.5.1 Acquisition parameters	8
1.5.2 Radiation dose	10
1.5.3 Interconnection of CT acquisition parameters	10
1.5.4 Mathematical models	11
1.5.4.1 Compartment model	11
1.5.4.2 Deconvolution model	13
1.5.5 Clinical applications	20
1.6 Motivation and background	21
1.7 Objectives	23
1.8 Structure	24
1.9 Contribution of others	24
2 Materials and methodology	25
2.1 Dataset	26
2.1.1 The search strategy for research articles	26
2.1.1.1 Inclusion and exclusion criteria for research articles	26
2.1.2 Clinical dataset	28
2.1.2.1 Acquisition of clinical dataset	28
2.1.2.2 Inclusion and exclusion criteria of clinical dataset .	28
2.2 Region of interest (ROI) selection	31
2.3 Motion correction of the clinical dataset	32
2.4 Data extraction from research articles	33
	iii

Contents

2.5	Statistical analysis of data extracted from research articles	34
2.6	Noise-correction of BF measurements	36
2.6.1	Statistical analysis	42
2.6.2	Validation	45
2.7	First-pass analysis (FPA)	45
2.7.1	FPA approach 1 (FPA1)	46
2.7.2	FPA approach 2 (FPA2)	46
2.7.3	Perfusion maps	48
2.7.4	Statistical analysis	49
2.7.5	Radiation exposure and acquisition time	49
3	Results	51
3.1	Meta-analysis of pancreatic CT perfusion studies	51
3.1.1	Distribution of study parameters over the years	52
3.1.2	Comparison of pancreatic clinical entities based on quantitative measurements	55
3.1.3	Effects of CT examination parameters and perfusion model on the quantitative measurements	57
3.2	Noise-correction algorithm analysis	61
3.2.1	Digital perfusion phantom	61
3.2.2	Validation on clinical dataset	65
3.3	First pass analysis	67
3.3.1	FPA1	67
3.3.2	FPA2	69
3.3.3	Validation using Maximum slope model	69
4	Discussion	77
4.1	Meta-analysis of pancreatic CT perfusion studies	79
4.2	Development of noise correction algorithm	81
4.3	First pass analysis	83
4.4	Limitations and future developments	85
4.5	Conclusion	89
5	Summary	91
6	Zusammenfassung	93
7	Bibliography	97
8	Personal publications	109
8.1	First authorship peer-reviewed journal contributions	109
8.2	Co-authorship peer-reviewed journal contributions	110
8.3	Manuscript under preparation	110
8.4	First and co-authorship conference contributions and proceedings	110
A	DICOM	115
		iv

B	Softwares	117
B.1	Syngo.via	117
B.2	SOPHIA	118
B.2.1	Grassroots DICOM (GDCM)	120
B.2.2	ROOT	120
B.2.3	Insight Segmentation and Registration Toolkit (ITK)	123
C	Statistics	125
C.1	Student's t-test	125
C.2	ANOVA	127
C.3	ANCOVA	128
C.4	Linear regression analysis	129
C.5	Box-and-whisker plots	130
C.6	Contrast to noise ratio (CNR)	131
C.7	Model error	132
C.8	Random error	132
C.9	Bland-Altman analysis	133
C.10	Pearson's correlation coefficient	134
C.11	Coefficient of variation (COV)	135
C.12	SAS (Statistical Analysis System)	135
D	Addition of varied noise samples during the development of noise correction algorithm	137
E	Additional approach to obtain the optimized acquisition time for FPA - an extension of FPA1	139
	Curriculum Vitae	141
	Acknowledgements	143
	Eidesstattliche Verischerung	145

Abbreviations

AIF	Arterial Input Function
ANCOVA	Analysis of covariances
ANOVA	Analysis of variances
BF	Blood Flow
BV	Blood Volume
CNR	Contrast to Noise Ratio
COV	Coefficient of Variation
CTDI	Computed Tomography Dose Index
CT	Computed Tomography
DCE-CT	Dynamic Contrast Enhanced - Computed Tomography
DICOM	Digital Imaging and Communications in Medicine
DLP	Dose Length Product
DW-MRI	Diffusion weighted - Magnetic Resonance Imaging
FE	Field Extraction Product
FPA	First Pass Analysis
GDCM	Grassroots DICOM
GTBF	Ground Truth Blood Flow

Abbreviations

GTBV	Ground Truth Blood Volume
HU	Hounsfield Unit
IQR	Interquartile Range
IRF	Impulse Response Function
ITK	Insight Segmentation and Registration Toolkit
MRI	Magnetic Resonance Imaging
MSM	Maximum Slope Model
MTT	Mean Transit Time
NET	Neuroendocrine Tumor
PACS	Picture Archiving and Communication Systems
PDAC	Pancreatic Ductal Adenocarcinoma
PET	Positron Emission Tomography
ROI	Region of Interest
SAS	Statistical Analysis Software
SD	Standard Deviation
SOPHIA	Software for Physics and Image Analysis
SPN	Solid Pseudopapillary Neoplasm
TAC	Tissue Attenuation Curve
TTD	Time to Drain
TTP	Time to Peak
TTS	Time to Start

List of Figures

Figure 1.1	Anatomy of the pancreas in the human body	2
Figure 1.2	CT scan of the upper abdomen of the human body	5
Figure 1.3	Depiction of a CT scanner and its components	6
Figure 1.4	Dynamic contrast-enhanced CT (DCE-CT) images	8
Figure 1.5	Single compartment model of tissue perfusion	13
Figure 1.6	Double compartment model of tissue perfusion	14
Figure 1.7	IRF for adiabatic approximation of tissue homogeneity model	19
Figure 1.8	Tissue time attenuation curve (TAC).	20
Figure 2.1	Flowchart illustrating a basic overview of the thesis	27
Figure 2.2	Dynamic CT image with marked regions of interest (ROIs)..	32
Figure 2.3	Arterial input function (AIF) of a digital perfusion phantom	37
Figure 2.4	Impulse response function (IRF) of a digital perfusion phantom	38
Figure 2.5	Tissue attenuation curves (TACs) of a digital perfusion phan- tom	39
Figure 2.6	Noise-impacted tissue attenuation curves (TACs) of a digital perfusion phantom	40
Figure 2.7	Tissue attenuation curves (TACs) of a pancreatic adenocar- cinoma patient	41
Figure 2.8	An example of a digital perfusion phantom	42
Figure 2.9	An example of a BF map obtained from a digital perfusion phantom	43
Figure 2.10	The flow chart of the noise correction algorithm	44
Figure 2.11	First pass analysis 1 (FPA1) acquisition protocol	47
Figure 2.12	First pass analysis 2 (FPA2) acquisition protocol	48
Figure 3.1	Flowchart illustrating the meta-analysis process	53
Figure 3.2	Histogram distribution of data extracted from selected studies	54
Figure 3.3	Linear regression plots of the number of studies, sample size, and CT examination parameters	56
Figure 3.4	Boxplots for comparing the reported results of quantitative measurements	59
Figure 3.5	W-ANOVA Tukey grouping for comparing the weighted means of quantitative measurements	61
Figure 3.6	Boxplots comparing the effect of acquisition parameters on quantitative measurements	62
		ix

List of Figures

Figure 3.7	An example of ground truth, noise-impacted and noise-corrected blood flow perfusion maps	63
Figure 3.8	Absolute difference, model error, and random error curves in noise-correction algorithm	65
Figure 3.9	Bland-Altman plots for digital perfusion phantom	66
Figure 3.10	Bland-Altman plot for clinical dataset between the noise-impacted and noise-corrected blood flow measurements	67
Figure 3.11	An example of noise-impacted and noise-corrected blood flow perfusion maps for clinical data	69
Figure 3.12	First pass analysis (FPA) and maximum slope model (MSM) perfusion maps	70
Figure 3.13	Box plot analysis at different acquisition timings of FPA2	73
Figure 3.14	Correlation curves between FPA2 and MSM	74
Figure 3.15	Comparison of effective dose and scan time between MSM and FPA	75
Figure A.1	DICOM file representation consisting of image data and meta-data	116
Figure B.1	Screenshot of the syngo.via software	119
Figure B.2	Screenshot of SOPHIA Viewer software	121
Figure B.3	Screenshot of SOPHIA Perfusion software	122
Figure C.1	A box-plot graphical representation	131
Figure D.1	Digital perfusion phantom images generated by adding varied noise samples	138

List of Tables

Table 1.1	Glossary of symbols used to describe CT perfusion mathematical models	12
Table 2.1	Acquisition protocol for the contrast-enhanced dynamic abdominal CT	29
Table 2.2	Demographic information of pancreatic adenocarcinoma patients	31
Table 2.3	An overview of the dimensions of the Region of Interest (ROI) delineated on the dynamic CT image	32
Table 3.1	Number of studies (number of patients) reporting the quantitative parameters	52
Table 3.2	Mean \pm SD of the quantitative parameters	57
Table 3.3	Overview of the statistical analysis reported by the studies . .	58
Table 3.4	Effects on quantitative measurements	60
Table 3.6	Absolute difference, model error, and random error in noise-correction algorithm	63
Table 3.5	Mean \pm SD blood flow (BF - ml/100ml/min) measurements and CNR for digital perfusion phantom	64
Table 3.7	Mean \pm SD blood flow (BF - ml/100ml/min) measurements and CNR for clinical dataset	68
Table 3.8	Mean \pm SD blood flow (BF - ml/100ml/min) for circular ROI using FPA1, FPA2 and MSM	71
Table 3.9	Mean \pm SD blood flow (BF - ml/100ml/min) for polygonal ROI using FPA1, FPA2 and MSM	72
Table E.1	Mean \pm SD blood flow (BF - ml/100ml/min) ROI using additional FPA approach	140

*I have by no means always been numbered among
those who pluck the fruit. I have been repeatedly
only one of those who planted or cared for the trees.*

Philipp Lenard

1

Introduction

This chapter provides a basic understanding of the idea behind this thesis. It begins with a general introduction of the pancreas and pancreatic tumors in Sections 1.1 and 1.2, respectively. Following this, the Section 1.3 provides the diagnostic methods used for the detection of pancreatic tumors. Afterward, the basic principle of computed tomography (CT), the technical setup of CT scanners, and various CT imaging techniques are described in Section 1.4. The CT technique which is an important focus of this thesis i.e., CT perfusion has been thoroughly described in Section 1.5. This section includes a description of CT perfusion with its acquisition parameters and an explanation of the radiation dose. Furthermore, the mathematical models used in CT perfusion have been described in detail following the clinical applications of CT. The maximum slope model (MSM) and the deconvolution model have been provided in Sections 1.5.4, respectively. The chapter also provides insight into the motivation and background behind this work in Section 1.6. The main objectives of this thesis are included in Section 1.7. The first chapter concludes with information on the overall structure of this thesis and the contributions of others to this work, as detailed in Sections 1.8 and 1.9.

1.1 Pancreas

The pancreas is a vital organ located in the abdominal region of the human body behind the stomach (Longnecker 2021). Anatomically, it is divided into three main regions: the head, body, and tail. The head is located on the right side of the abdomen, the body is located behind the stomach, and the tail extends to the left side of the abdomen as shown in Figure 1.1. The pancreas plays a crucial role in maintaining overall health and homeostasis of the body. It performs endocrine functions, that is, producing hormones such as insulin and glucagon that help regu-

Introduction

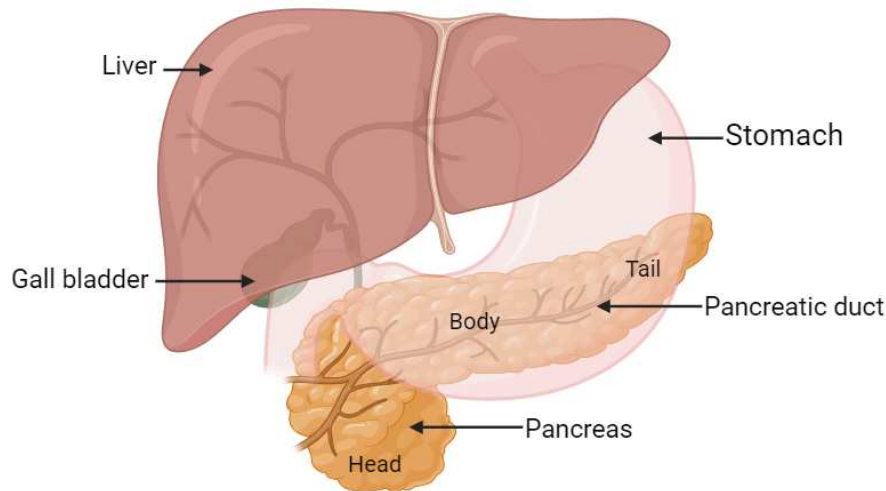


Figure 1.1: Anatomy of the pancreas in the human body. The pancreas is located behind the stomach and is divided into head, body, and tail regions.

late blood sugar levels, and exocrine functions, such as producing digestive enzymes that help digest food, especially proteins (Karpińska & Czauderna 2022). Therefore, proper functioning of the pancreas is essential for maintaining homeostasis and overall metabolic health in the human body.

A variety of medical conditions lead to abnormal functioning of the pancreas, such as:

1. Pancreatitis - inflammation of the pancreas
2. Pancreatic tumor
3. Cystic fibrosis
4. Diabetes

1.2 Pancreatic tumors

Pancreatic tumor is one of the most common types of cancer in humans with a high mortality rate. It is the eighth most common cancer in women and the tenth most common cancer in men (American Society of Clinical Oncology (ASCO) Cancer.Net 2023). A pancreatic tumor is caused by the abnormal or uncontrolled growth of cells in the pancreas. It can be benign (non-cancerous) or malignant (cancerous). This abnormal growth can occur due to genetic cell mutation, smoking, excessive alcohol consumption, obesity, age, chronic pancreatitis, or family history.

There are several types of pancreatic tumors (Mostafa et al. 2017):

1.3. Diagnostic methods for pancreatic tumors

1. Pancreatic adenocarcinoma or pancreatic ductal adenocarcinoma (PDAC): This is the most common type of pancreatic tumor, accounting for about 85% of all cases. It usually starts in the cells that line the pancreas, and is most often found in the head region of the pancreas. They are difficult to diagnose, mostly detected at a later stage, and hence they are difficult to treat. These are aggressive tumors. The prognosis remains poor despite advances in treatment procedures. They have a very high mortality rate (estimated 90% dying at 1 year despite the treatment) (Puckett & Garfield 2023, McGuigan et al. 2018, Wang et al. 2021).
2. Pancreatic neuroendocrine tumors (NETs): These are tumors that start in the hormone-producing cells of the pancreas. They can be functioning (producing hormones) or non-functioning (not producing hormones). NETs are less common than pancreatic adenocarcinoma and tend to grow more slowly.
3. Pancreatic cysts: These are fluid-filled sacs that develop in the pancreas. Most pancreatic cysts are benign and do not cause symptoms, but some can become cancerous over time.
4. Solid pseudopapillary neoplasms (SPNs): These are rare tumors that usually affect young women. They are typically slow-growing and have a low risk of spreading to other parts of the body.
5. Acinar cell carcinoma: This is a rare type of pancreatic cancer that starts in cells that produce digestive enzymes in the pancreas. It tends to grow slowly and may not cause symptoms until it has reached an advanced stage.

Pancreatic tumors have a high mortality rate and are difficult to diagnose, often detected at later stages when treatment options are limited. Improved diagnostic methods are crucial for early detection, accurate diagnosis, and better treatment outcomes for patients with pancreatic tumors. Therefore, there is a need for advanced imaging techniques to enhance the detection and evaluation of pancreatic tumors.

1.3 Diagnostic methods for pancreatic tumors

Pancreatic tumors can be diagnosed by biopsy, that is extraction of a small tissue sample from the suspected area and examination in the laboratory. However, the location of the pancreas makes it difficult to extract the biopsy sample. Thus, medical imaging techniques are preferred as non-invasive techniques for the better detection and diagnosis of pancreatic tumors (Zhao & Liu 2020). The imaging techniques used for diagnosis are (Puckett & Garfield 2023):

1. Computed Tomography (CT): CT uses X-rays from different angles and provides detailed, multi-dimensional images (usually 3-dimensional or more) of

Introduction

the pancreas and the surrounding organs. In some cases, a special iodinated contrast (dye) called contrast medium is injected into a vein to show better differences in the tissues (see Figure 1.2). A detailed explanation of CT is given in Section 1.4.

2. Ultrasound/ Sonography: It uses ultrasonic (high frequency) sound waves to generate two-dimensional images of the pancreas, and surrounding soft tissues of the body.
3. Magnetic Resonance Imaging (MRI): MRI provides detailed three-dimensional images of the pancreas and surrounding organs using powerful magnetic and radio waves. In MRI, a special gadolinium-based contrast (dye) may be used to obtain better contrast between the tissues.
4. PET (Positron Emission Tomography) or PET-CT: PET provides multi-colored images of the pancreas and surrounding organs. In PET, a tracer (radioactive sugar substance) is injected into the human body and illuminates the cells that use more energy on the scan. As tumor cells use more energy, they appear brighter on the PET scan. In PET-CT or PET-MRI, CT / MRI provides anatomical information on the tissue, while PET provides metabolic information on the tissue. PET is usually combined with CT for the diagnosis of pancreatic tumors and is called PET-CT. Sometimes, it may also be combined with MRI, and called PET-MRI.

Among all the above-mentioned diagnostic techniques, CT is the most commonly used imaging technique for evaluating the pancreas and diagnosing pancreatic tumors (Almeida et al. 2018). CT is preferred over ultrasound as it can provide detailed images of the pancreas and surrounding tissues. Also, CT is preferred over MRI (Puckett & Garfield 2023, Chen et al. 2016) as it has an excellent temporal resolution, is less expensive, is faster, and is more easily available. CT can be used to diagnose pancreatitis, pancreatic cysts, pancreatic tumors, and other conditions affecting the pancreas. It can also be used to guide biopsies or other procedures in the pancreas.

1.4 Computed Tomography (CT)

Computed Tomography is a medical imaging technique that combines computer processing (computed) with the acquisition of cross-sectional slices (tomo) to generate detailed visual images (graph) of the body's internal structures. Thus, the term 'Computed Tomography' can be deconstructed into 'Computed' (computer processing), 'tomo' (slices), and 'graph' (images).

The first commercial CT scanner was invented by physicist Allan MacLeod Cormack and electrical engineer Godfrey N. Hounsfield (Hounsfield 1980) in 1972 (Patel & De Jesus 2023, Jung 2021). It is a non-invasive medical imaging technique

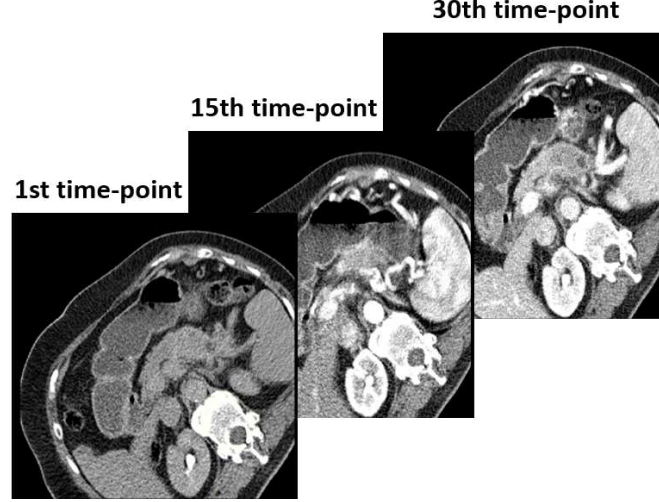


Figure 1.2: Single slice from CT scan of the upper abdomen of the human body displaying the location of the pancreas outlined by yellow marker, and the aorta outlined by the red marker. The enhancement due to the contrast agent injected can also be seen on the image.

that uses ionizing radiation or X-rays to generate detailed cross-sectional images or slices (tomographic images). CT scans provide more detailed information than normal X-ray scans. CT can produce images of bones, blood vessels, soft tissues, and organs, thus playing a key role in the detection, diagnosis, and monitoring of the response to treatment of various diseases (Patel & De Jesus 2023, Liu 2018).

1.4.1 Principle

During a CT scan, the patient lies on a table that moves through a circular opening in a machine called a gantry. X-ray beams are projected through the body from various angles, and detectors on the other side of the scanner measure the amount of radiation that passes through the body (Goldman 2007). **The basic principle of CT is that the density of the tissue through which the X-rays pass can be measured by calculating the attenuation coefficient of the X-ray (Jung 2021).** Different amounts of attenuation occur on X-rays depending on the type of tissue through which they pass. Tissues with higher attenuation appear brighter on the scan, and tissues with lower attenuation appear darker on the scan. The greater the difference in attenuation within the tissues, the greater the contrast on the CT images. The density or attenuation coefficient (μ) of the measured tissue is represented by the CT number or the Hounsfield unit (HU) (Jung 2021). The CT number can be represented as:

$$CTnumber(x, y, z) = 1000 * \frac{\mu(x, y, z) - \mu_{water}}{\mu_{water}} [HU] \quad (1.1)$$

where μ and μ_{water} are the attenuation coefficients of the tissue of interest and

Introduction

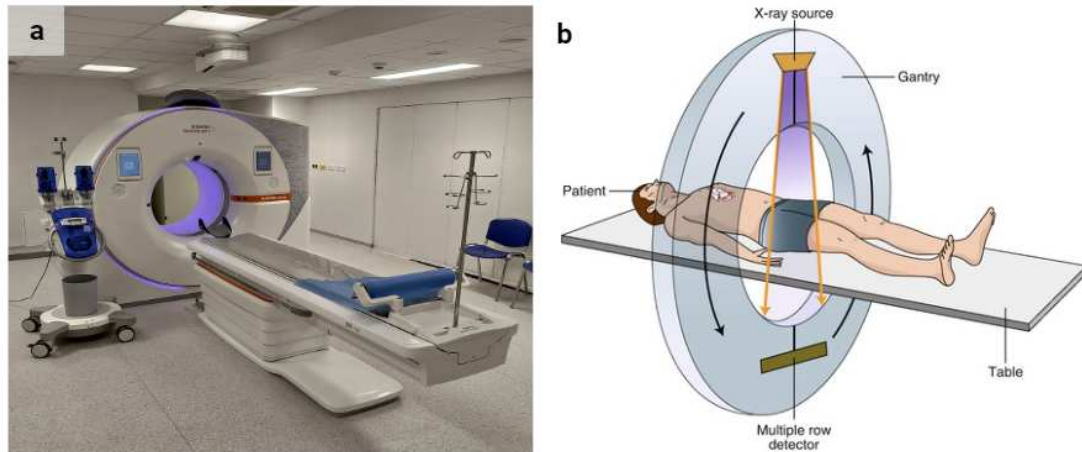


Figure 1.3: (a) Depiction of a modern CT scanner (Vendiš 2022), (b) main components of the CT scanner, including the gantry, the x-ray tube, the detector array, and the CT table (Garnett 2020).

the water, respectively. Thus, by equation 1.1, the CT number and hence the enhancement in the CT image is zero for the voxel containing water. The computer then processes this information of CT numbers of different tissue regions to create detailed cross-sectional CT images of the examined body part.

1.4.2 Image reconstruction

The CT numbers are then processed to reconstruct detailed cross-sectional CT images or slices of the body's internal structures. To reconstruct the image, mathematical algorithms such as filtered back projection (FBP) or iterative reconstruction techniques are used.

Filtered back projection involves applying filters to the raw data before back-projecting them to form an image. While FBP is relatively fast, it may produce images with artifacts, especially in cases of limited data or irregular sampling.

Iterative reconstruction methods, on the other hand, iteratively refine an initial image estimate to better match the measured data. These techniques often provide higher image quality and better noise reduction compared to FBP. However, they are computationally intensive and require more processing time.

Recent advancements in CT technology have led to the development of more sophisticated reconstruction algorithms, such as statistical iterative reconstruction and model-based iterative reconstruction. These approaches take into account statistical properties of the measured data and incorporate detailed models of the imaging system and patient anatomy to further improve image quality and reduce radiation dose.

Overall, image reconstruction in CT is a complex yet essential process that enables clinicians to obtain detailed and accurate images for diagnosing various medical conditions, treatment planning, and monitoring patient progress.

1.4.3 Type of CT imaging techniques

There are several types of CT imaging techniques (Jiang Hsieh 2021), including:

1. Single slice CT: This technique uses a fan-shaped X-ray beam, and the detector, which rotates around the patient's body and produces cross-sectional images of the internal organs. It generates a single slice image per scan.
2. Spiral CT/ Helical CT: This technique uses a fan-shaped X-ray beam and detector (or multidetector) which moves along a helical path around the patient's body as the table moves through the CT scanner and produces a series of continuous images (Liu 2018).
3. Multislice CT/ Multidetector CT: This technique uses multiple rows of detectors to capture more images in a single rotation of the X-ray tube, resulting in higher resolution and faster scanning times.
4. Dual-energy CT: This advanced imaging technique uses two different X-ray energies, which acquire two datasets showing different attenuation levels. It improves diagnostic accuracy and reduces the need for additional tests.

Dual-energy CT can also be combined with multislice and helical CT scanners to enhance diagnostic capabilities. Multislice CT and dual-energy CT are often utilized in conjunction with helical CT. While multislice CT allows for the rapid acquisition of multiple slices, and dual-energy CT provides additional information about tissue composition, combining them with the helical scanning technique enhances overall imaging efficiency and diagnostic potential.

Despite the widespread use of CT in clinical practices, it is still an active area of research. The advancement in CT with research has enabled faster scanning times, higher-resolution images, and more accurate diagnosis. One of the most effective advancements of CT is the development of a non-invasive imaging technique that provides physiological information about the tissue along with anatomical information. This technique is called CT perfusion.

1.5 CT perfusion

CT perfusion (Miles & Griffiths 2003) is a non-invasive functional imaging technique that enables the measurement of physiological parameters along with anatomical information about the tissue. It has become a valuable tool in the diagnosis and detection of the diseases that influence tissue perfusion.

Introduction

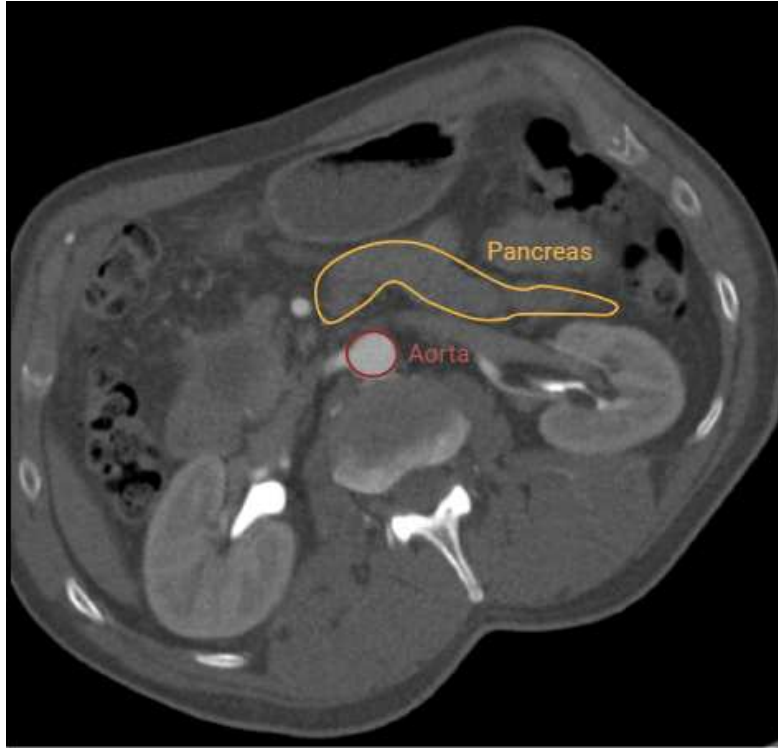


Figure 1.4: Dynamic contrast-enhanced CT (DCE-CT) images at the 1st, 15th, and 30th acquisition time-point of a single slice of a pancreatic adenocarcinoma patient

This technique involves the injection of a short bolus of 40-50 ml of contrast agent at a high flow rate of 4-6 ml/s into the patient's bloodstream followed by a 40 ml flush of saline at a similar flow rate (Petrulia et al. 2010). In general, CT contrast media is a colorless and transparent iodine compound, that is, a substance that X-rays cannot penetrate. Acquisition of CT perfusion involves acquiring a baseline unenhanced CT image, that is, without contrast CT image, followed by sequential acquisition of dynamic CT images after intravenous injection of an iodine-based contrast agent as represented by the Figure 1.4. Thus, CT perfusion is also referred to as **dynamic contrast-enhanced CT (DCE-CT)**. The acquired CT images are then analyzed by applying mathematical models to generate perfusion maps, which provide hemodynamic and physiological information on the tissue. This tissue physiological information helps in the early and more accurate diagnosis of various diseases, such as stroke, brain tumors, cancer, cardiovascular diseases, and liver diseases.

1.5.1 Acquisition parameters

CT perfusion images are acquired using specific settings and techniques, which are referred to as CT perfusion acquisition parameters. These parameters include acquisition and reconstruction parameters, injections of the contrast material pro-

tol, and radiation dose (Zussman et al. 2011). The acquisition parameters (Miles & Griffiths 2003) for CT perfusion can vary depending on the specific clinical application. It is important to select the appropriate acquisition parameters to optimize image quality while minimizing radiation exposure to the patient. Some of the acquisition parameters are:

1. **Scan time (s):** It represents the total amount of time taken for the complete acquisition of all the dynamic CT images. Total scan time can range from 30 to 70 seconds, depending on the specific clinical application, but it is crucial to ensure that the scan is not too short to accurately assess perfusion or too long, which would waste radiation dose.
2. **Tube voltage (kVp):** The voltage applied to the X-ray tube used in the CT scanner. Lower kVp values (70-90 kVp) are recommended for CT perfusion imaging to reduce radiation exposure to the patient while maintaining diagnostic image quality.
3. **Tube current (mA):** The amount of current flowing through the X-ray tube. The optimal mA setting depends on the scanner type and the patient's body size. The tube current-time product (mAs) is another technical parameter used in CT perfusion imaging, obtained by multiplying the tube current by the tube rotation time (in seconds).
4. **Slice thickness (mm):** It represents the thickness of a single slice. Determines the resolution of CT perfusion images. A thinner slice thickness can provide higher-resolution images but may increase radiation exposure to the patient.
5. **Axial coverage (cm):** The length of the scanned area along the z-axis. The size of the coverage can vary depending on the number of slices acquired in a single rotation. 64 or 128-slice coverage in a single rotation allows a coverage size of 3–8 cm.
6. **Contrast material protocol:** Contrast material protocols include the amount, rate, and timing of injection of contrast agent to the patient. The injection rate (ml/s) and volume (ml) can affect the accuracy of the perfusion parameters. It can vary depending on the clinical application but typically ranges from 3-5 ml/s for a total volume of 40-60 ml.
7. **Radiation dose:** The amount of radiation exposure to the patient in CT perfusion acquisition. It is important to minimize radiation dose while maintaining image quality.

Introduction

1.5.2 Radiation dose

The effective radiation dose (Alomary et al. 2022), which is a measure of the total radiation dose delivered to the patient in CT perfusion can be quantified by Dose Length Product (DLP) as represented by equation 1.3. The measurement unit for the effective radiation dose is milliSieverts (mSv). DLP is an important metric used to quantify radiation exposure from CT acquisitions. DLP (milligray-centimeters (mGy.cm)) is calculated by the product of the volumetric CT dose index (CTDIvol - mGy) with scan length (cm).

$$DLP = CTDI_{vol} * (scan\ length) \quad (1.2)$$

$$Effective\ dose = DLP * k \quad (1.3)$$

where “ k ” (mSv/mGy.cm) is a conversion factor depending on the body part being examined (Bhatt et al. 2017). DLP takes into account both the intensity and the duration of radiation exposure. The CTDIvol and DLP can vary widely depending on the specific imaging protocol. For CT perfusion imaging, the DLP can range from a few hundred to several thousand mGy.cm, depending on the specific imaging protocol and the size of the scanned volume. The radiation dose (mSv) to the patients is thus, estimated by the multiplication of DLP with the conversion factor for CT examinations (Yu et al. 2018).

1.5.3 Interconnection of CT acquisition parameters

CT acquisition parameters are interconnected, influencing both image quality and radiation dose. Adjustments in parameters such as tube current, tube voltage, slice thickness, and pitch directly impact the amount of radiation exposure a patient receives and the quality of resulting images. Understanding the interconnection between CT acquisition parameters and radiation dose is crucial for the radiologists. There is a direct relationship between certain acquisition parameters and radiation dose. For example, increasing tube current or tube voltage typically increases radiation dose but also improve image quality by reducing noise. Additionally, tube current and tube voltage influence the amount and quality of X-ray photons generated.

However, some parameters can be adjusted to maintain image quality while reducing dose. For instance, reducing slice thickness can improve spatial resolution without increasing dose. Thinner slices provide higher resolution but may increase noise levels. Reconstruction algorithm influences image appearance and noise levels. Iterative reconstruction techniques can reduce noise while maintaining image quality compared to FBP.

Optimization of these CT acquisition parameters is necessary to balance the trade-off between image quality and radiation dose. Radiologists often adjust these parameters based on the clinical indication and patient characteristics to achieve diagnostic images with the lowest possible radiation dose.

1.5.4 Mathematical models

Mathematical models are applied to the CT perfusion images to obtain valuable perfusion information of the tissue by representation of two important curves: the arterial input function (AIF) and tissue attenuation curve (TAC). The AIF represents the concentration of contrast agents in the arteries over time, while the TAC reflects the concentration of contrast agent in the tissue of interest over time. The calculation of AIF from small arteries can result in an underestimation of perfusion due to partial volume effects. A study by Cenic et al. (Cenic et al. 1999) examined the effect of partial volume effects on CT measurement and demonstrated that this underestimation is negligible when dealing with arteries with internal diameters exceeding 1.73 mm. Therefore, the largest artery in the body, that is, the aorta, is used to calculate the AIF, and thus partial volume effects can be avoided. In Figure 1.2, the aorta can be seen in the CT scan of the upper abdomen of the human body marked by a red outline. This understanding of the AIF is a prerequisite for constructing mathematical models of CT perfusion images. The mathematical models thus, encompass the representation of these attenuation curves and involve solving sets of differential equations or convolution integrals to estimate perfusion parameters such as blood flow, blood volume, and others. These models can be classified as follows based on their applications in tissue perfusion analysis (Hansen et al. 2013):

1.5.4.1 Compartment model

These models consider tissue as a compartment and use trace kinetic analysis to obtain tissue perfusion information. These are also called tracer-kinetic models. The kinetic perfusion parameters are obtained based on the assumption that the relationship between the concentration of the injected iodine-based contrast agent in the tissue and the attenuation of the X-rays is almost always linear. These can be classified as single- or double-compartment models. The single-compartment model uses Fick's principle and considers tissue as a single compartment as shown in Figure 1.5, whereas, a double-compartment model divides the tissue into two compartments, that is, the intravascular and extracellular-extravascular spaces as represented by Figure 1.6. The double-compartment model includes the exchange of bloodstream-containing contrast agents between the intravascular and extracellular-extravascular space as shown in the Figure 1.6. The single-compartment model provides estimates of arterial flow, whereas the double-compartmental model provides estimates of blood volume and the permeability of the tissue system.

Introduction

Symbol	Description	
AIF	Arterial input function	
$C_a(t)$	Concentration of contrast agent at arterial inlet	
$C_e(t)$	Concentration of contrast agent in extracellular-extravascular space	
$C_i(t)$	Concentration of contrast agent in intravascular space, i.e. blood plasma	
$C_t(t)$	Concentration of contrast agent in tissue	
$C_v(t)$	Concentration of contrast agent at venous outlet	
E	Extraction fraction	
F	Flow	
FE	Flow extraction product	
$h(\tau)$	Probability density function of blood transit time	
IRF	Tissue impulse response function	
$K(t)$	Tissue impulse residue function	
$M_t(t)$	Amount of contrast agent injected	
MTT	Mean transit time	
$R(t)$	Residue function	
ρ_t	Mean density of tissue	
t	Time	
TAC	Tissue attenuation curve	
TTD	Time to drain	
TTP	Time to peak	
V_t	Volume of contrast agent in tissue	
V_e	Volume of contrast agent in extracellular-extravascular space	12

Table 1.1: Glossary of symbols used to describe CT perfusion mathematical models

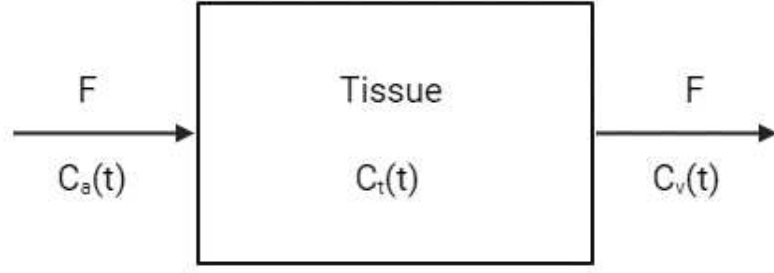


Figure 1.5: Single compartment model of tissue perfusion. $C_a(t)$ represents the arterial input concentration of the contrast agent into the tissue with flow rate F , $C_t(t)$ is the concentration of the contrast agent accumulated in the tissue, and $C_v(t)$ represents the venous outflow concentration of the contrast agent from the tissue with similar flow rate F

Fick's principle:

One of the most basic ways to model tissue perfusion is Fick's principle (Konstas et al. 2009a). In the vascular system, the concentration of contrast agent cannot be measured, but only the average concentration of contrast agent in the tissue can be measured. Thus, Fick's principle considers tissue as a single compartment, where the contrast agent enters through the arterial inlet with the bloodstream and exits through the venous outlet, as shown in the Figure 1.5.

If the injected contrast agent enters and exits the tissue system with blood flow F as illustrated in Figure 1.5, then the temporal change of the contrast agent mass (concentration \times volume) inside the tissue at time t is described by Fick's principle using equation 1.4:

$$\frac{dM_t(t)}{dt} = V_t \frac{dC_t(t)}{dt} = F[C_a(t) - C_v(t)] \quad (1.4)$$

where $M_t(t)$ is the total amount of contrast agent injected into the patient, $C_a(t)$ is the arterial input concentration of the contrast agent into the tissue with flow rate F , $C_t(t)$ is the concentration of the contrast agent of volume V_t accumulated in the tissue, and $C_v(t)$ represents the venous outflow concentration of the contrast agent from the tissue with similar flow rate F .

1.5.4.2 Deconvolution model

These models consider tissue as a "black box" and use the deconvolution method to obtain tissue perfusion information. This model is based upon one of the oldest mathematical theories, the indicator dilution theory, as explained below:

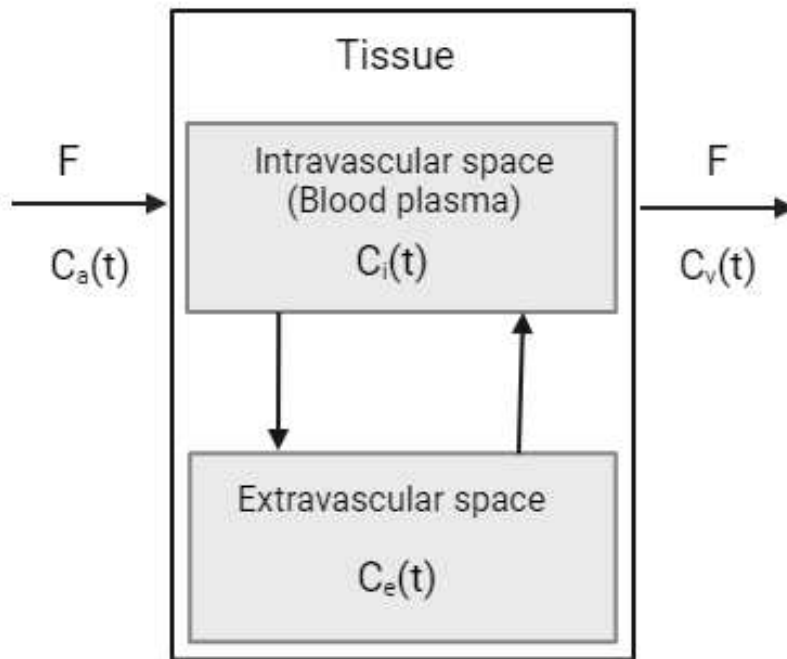


Figure 1.6: Double compartment model of tissue perfusion. The tissue has been divided into two compartments, namely, the intravascular space or blood plasma, and the extracellular-extravascular space. The contrast agent that enters the tissue of interest through the artery is distributed between the two compartments inside the tissue and exits the tissue through veins. $C_a(t)$ represents the arterial input concentration of contrast agent in tissue with flow rate F , $C_i(t)$ is the concentration of contrast agent accumulated in the blood plasma of the tissue, $C_e(t)$ is the concentration of contrast agent leaking into the extracellular-extravascular space of tissue, and $C_v(t)$ represents the venous exit concentration of contrast agent from tissue with similar flow rate F

Indicator dilution theory:

The indicator dilution method (Miles & Griffiths 2003, Zierler 1962) is based on the application of the Stewart-Hamilton principle, which is also derived from Fick's equation (Stewart, 1897). The main principle is that the perfusion BF is proportional to the amount of blood that has diluted an introduced indicator, which is a contrast agent in CT perfusion. This theory is based on the assumptions of system linearity i.e. the system/ tissue must be constant throughout, and time invariance i.e. the flow and volume throughout the measurement must be constant; the contrast agent must exhibit the same distribution of transit times as blood. This theory states that the BF can be calculated using the total amount of contrast agent injected (M_t) and the amount of contrast agent transferred within the

measurement region.

$$F = \frac{M_t}{\int_0^\infty C_t(t) dt} \quad (1.5)$$

The mean transit time (MTT), that is, the mean time taken by the contrast agent to pass through the measurement region, can be calculated as

$$MTT = \frac{\int_0^\infty C_t(t) \cdot t dt}{\int_0^\infty C_t(t) dt} \quad (1.6)$$

Thus, blood volume V can also be computed using the product of F and MTT .

$$V = F \cdot MTT \quad (1.7)$$

The most commonly used perfusion mathematical models in CT perfusion (Miles & Griffiths 2003) are:

1. Maximum slope model (MSM)

This single-compartment model is based on the observation that the maximum slope of the contrast agent TAC is directly proportional to BF in the tissue. The maximum slope model is a relatively simple and fast method to estimate blood flow.

The MSM is a method used to calculate the BF of the tissue during the injection of a contrast agent. MSM (Mottola & Bevilacqua 2021) works on the principle of conservation of mass within the system as stated by Fick's principle in equation 1.4.

$$\frac{dM_t(t)}{dt} = V_t \frac{dC_t(t)}{dt} = F[C_a(t) - C_v(t)] \quad (1.8)$$

As MSM is a single-compartment model, it restricts the measurement time before the venous outflow of the contrast agent, thus assuming the venous outflow of the contrast agent to be zero, that is

$$C_v(t) \simeq 0$$

Equation 1.8 can be written as

$$V_t \frac{dC_t(t)}{dt} \simeq F \cdot C_a(t) \quad (1.9)$$

Equation 1.9 can be modified as

$$\frac{dC_t(t)}{dt} \simeq \frac{F}{V_t} C_a(t) \quad (1.10)$$

Introduction

As flow F and volume V_t is assumed to be constant, it can be implied from equation 1.10 that $C_t(t)$ reaches its maximum slope when $C_a(t)$ reaches its maximum value. Thus, perfusion, i.e. flow per unit volume (ml/100ml/min) can be calculated from equation 1.10 as

$$\frac{F}{V_t} = \frac{\max \frac{dC_t(t)}{dt}}{\max C_a(t)} \quad (1.11)$$

Thus, MSM allows one to calculate the flow of the tissue from the maximum upslope of TAC and the maximum of the AIF.

$$Flow = \frac{\text{Maximum upslope of TAC}}{\text{Maximum of AIF}} \quad (1.12)$$

Thus, MSM provides the perfusion of the tissue from the maximum gradient of the TAC, which corresponds to the phase of maximum enhancement of the contrast agent. This phase typically occurs shortly after the injection of the contrast agent, during the first pass of the contrast through the tissue. Thus, MSM allows for the calculation of blood flow with a comparatively short acquisition time, which further reduces the radiation exposure to the patient and image artifacts caused due to the breathing motion of the patient. However, due to the zero venous outflow assumption, the MSM method may lead to an underestimation of higher perfusion values at a high flow rate.

2. Deconvolution model

This model involves deconvolution between the measured TAC and the AIF to obtain a residue function, also called the impulse residue function (IRF). From the calculated IRF, the tissue perfusion measurements, such as blood flow and blood volume, can be quantified.

The deconvolution model is based on the principle of indicator dilution theory. This model (Fieselmann et al. 2011, Mottola & Bevilacqua 2021) states that the (dimensionless) residue function $R(t)$ quantifies the relative amount of contrast agent present in the tissue of interest at time $t = 0$, as

$$R(t) = \begin{cases} 1 - \int_0^t h(\tau) d\tau & t \geq 0 \\ 0 & t < 0 \end{cases} \quad (1.13)$$

where $h(\tau)$ is the probability density function of blood transit time. According to indicator dilution theory, as stated above, TAC can be computed as

$$C_t(t) = F \cdot \rho_t \cdot \int_{-\infty}^{\infty} C_a(\tau) R(t - \tau) d\tau = F \cdot \rho_t \cdot (C_a \otimes R)(t) \quad (1.14)$$

Here, the variables $C_t(t)$ and $C_a(t)$ can be measured and are known, while the values of F , $R(t)$, and ρ_t (mass density of the tissue) are unknown. A residue function $k(t)$ is introduced to calculate the perfusion parameters. The $K(t)$ is generally referred to as the impulse residue function or the impulse response function (IRF), as it represents the amount of contrast agent remaining within the system after a unit bolus.

$$K(t) = F \cdot \rho_t \cdot R(t) \quad (1.15)$$

Replacing $C_a(t)$ with AIF, $K(t)$ with IRF, and using equation 1.15, equation 1.14 can be written as

$$C_t(t) = AIF \otimes IRF \quad (1.16)$$

Hence, the deconvolution model states that the amount of contrast agent in the tissue can be calculated by the convolution of the amount of contrast agent injected in the artery (AIF) and the residue contrast agent in the tissue, i.e., IRF.

In addition, $K(t)$ or IRF can be calculated using AIF and $C_t(t)$ using the deconvolution method. The IRF basically represents the TAC resulting from an idealized scenario of injecting a single unit of tracer instantaneously. IRF is characterized by an almost instantaneous rise to a plateau, as the contrast material enters and remains within the tissue, which then decays as the contrast material exits the tissue (Miles 1991, Miles & Griffiths 2003). Thus, the IRF obtained by using the deconvolution of the TAC and the AIF can be used to calculate the perfusion measurements of the system or tissue as explained below.

$$F = \frac{1}{\rho_t} \cdot \max(IRF) \quad (1.17)$$

$$MTT = \frac{1}{\max(IRF)} \cdot IRF \quad (1.18)$$

$$V = MTT \cdot F = \frac{1}{\rho_t} \cdot IRF \quad (1.19)$$

Introduction

$$TTP = \operatorname{argmax}_t (C_t(t)) = \operatorname{argmax}_t (AIF \circledast IRF) \quad (1.20)$$

MTT can be calculated by dividing the area under the IRF curve by the height of the curve. As the IRF curve's height is standardized to 1, the area under the curve represents MTT. As V is derived by multiplying F and MTT, consequently, the area under the perfusion-scaled IRF yields V (MTT multiplied by perfusion, represented by F). (Miles & Griffiths 2003). This model, while offering greater accuracy compared to the maximum slope model, is also characterized by increased complexity and a longer processing time. Furthermore, it is difficult to obtain a unique solution for the deconvolution equation 1.16, especially the solution with meaningful information for CT perfusion analysis. To solve this deconvolution problem, a model-based deconvolution method is introduced. In this method, instead of calculating the IRF directly from the measured values, a modeled IRF is fitted to the data. This approach is an **adiabatic approach to the tissue homogeneity model** as explained by Lawrence et al. (Lawrence & Lee 1998, St Lawrence S. & Lee 1998, Skornitzke 2016). It assumes that for the first pass of the contrast agent, IRF is constant, and then while the contrast agent exits the tissue, IRF decreases exponentially. Thus, the resulting IRF is given by the equation 1.21

$$IRF(t) = \begin{cases} 0 & t < TTS \\ F & TTS < t < TTD \\ EF \cdot e^{-EF \frac{t-TTD}{V_e}} & t > TTD \end{cases} \quad (1.21)$$

where E is the extraction fraction, V_e is the volume in the extracellular-extravascular space, TTD is the total time taken by the contrast agent from the start of injection to drain i.e. $TTD = TTS + MTT$ (Figure 1.7), and the other parameters are as explained in the above sections.

This model is fit to the acquired data in each voxel, to obtain the solution, so that TAC or $C_t(t)$ can be optimized as

$$C_t(t) = (AIF \circledast IRF)(t) = \int_0^t C_a(\tau) IRF(t - \tau) d\tau \quad (1.22)$$

3. **Patlak model:** This double-compartment model determines perfusion in tissue based on the accumulation of contrast agents in the tissue over time. A Patlak graph extracted from a TAC measured in the tissue is used to quantify the blood volume and permeability of the tissue. A linear regression of the Patlak graph gives the transfer constant between the vascular compartment and extracellular space represented by the slope of the graph, and blood volume represented by the intercept of the graph.

The choice of mathematical models to analyze CT perfusion and generate perfusion maps depends on the specific application and the clinical condition to be

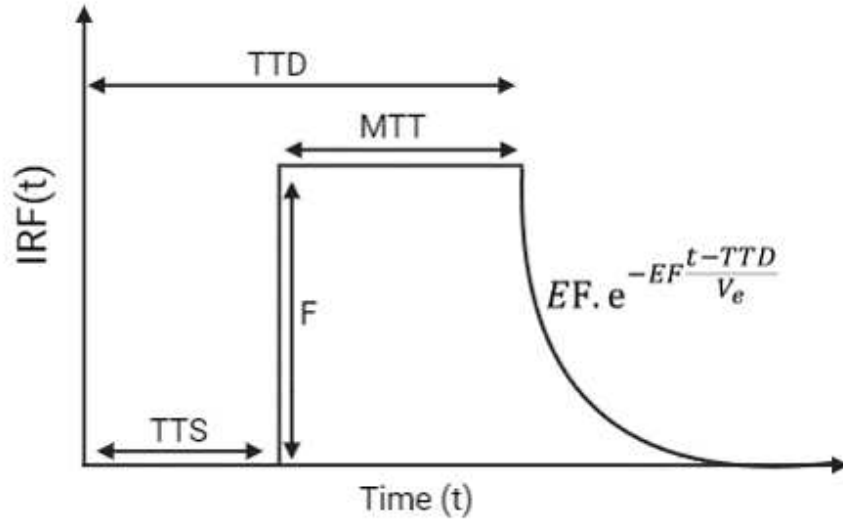


Figure 1.7: Ideal IRF for the adiabatic approximation of tissue homogeneity model. TTS is the time to start, MTT is the mean transit time, TTD is the time to drain, F is the blood flow, E is the extraction fraction, and V_e is the volume in the extracellular-extravascular space.

addressed. These mathematical models provide physiological information in terms of quantitative perfusion parameters (Bivard 2013, Petralia et al. 2010), such as:

1. **Blood flow (BF - ml/100ml/min):** BF is defined as the amount of arterial blood delivered through the volume of tissue per unit time. BF is often referred to as 'perfusion' (Cuenod & Balvay 2013).
2. **Blood Volume (BV - ml/100ml):** BV is defined as the volume in blood vessels within a given tissue.
3. **Permeability (ml/min/100ml):** It represents the flow of molecules through the capillary membranes in a certain volume of tissue.
4. **Flow extraction product (FE - ml/min/100 ml):** FE is a product of the BF and contrast agent extraction fraction, which is the fraction of contrast agent that reaches the tissue and leaks into the extracellular-extravascular space.
5. **Mean transit time (MTT - s):** MTT is the mean time it takes the contrast agent to pass through a specific tissue region.
6. **Time to peak (TTP - s):** TTP is the time taken by the contrast agent to reach its maximum concentration in a specific area of tissue.
7. **Time to start (TTS - s):** TTS is the time it takes the contrast agent to reach the tissue from the injected region.

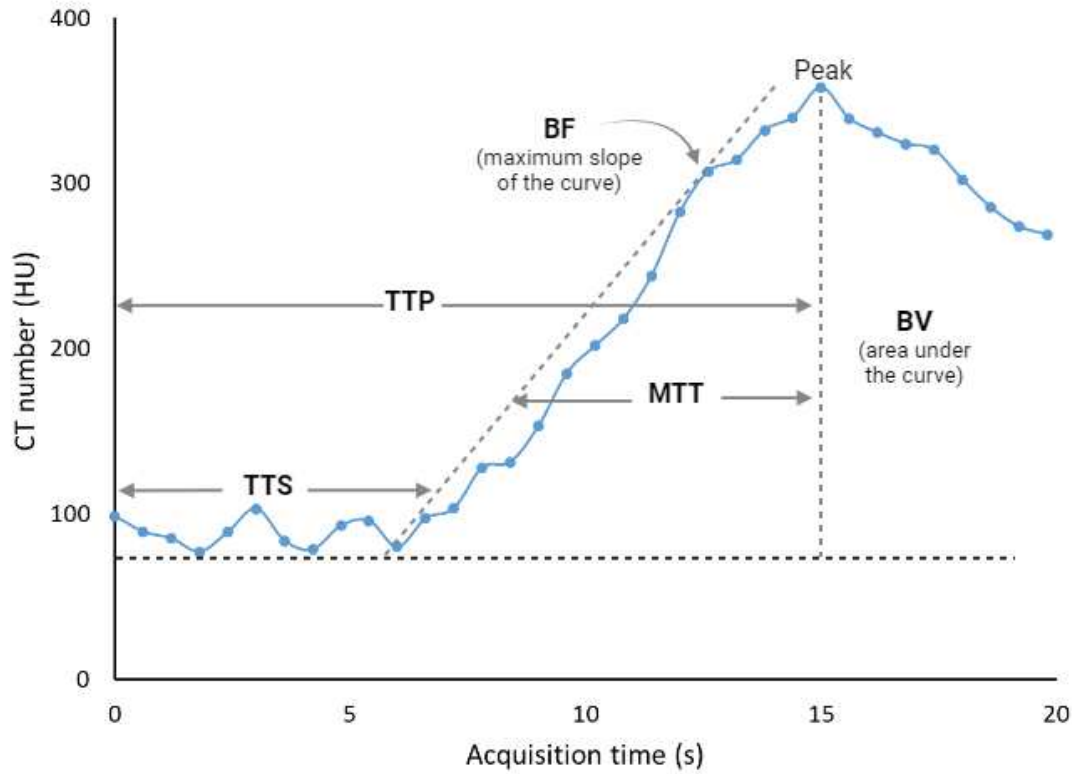


Figure 1.8: The tissue time attenuation curve (TAC) of healthy tissue in pancreatic adenocarcinoma patients. The following perfusion parameters can be computed from the TAC curve: Blood volume (BV) = area under the curve; Blood flow (BF) = gradient of wash-in of the curve; Time to start (TTS) = time to reach the tissue; Time to peak (TTP) = time to the maximum of the curve; Mean transit time (MTT) = time from wash-in to wash-out of contrast agent.

1.5.5 Clinical applications

Early clinical applications of CT perfusion focused primarily on the assessment of brain conditions, particularly in patients with ischemic stroke (Konstas et al. 2009b,a). This technique proved valuable for distinguishing brain regions with reduced blood flow (ischemia) from healthy brain tissue (Aksoy & Lev 2000). Additionally, CT perfusion plays a pivotal role in the diagnosis and prognosis of various neurological disorders, such as brain tumors, vasospasms, and infections. Studies have explored the use of CT perfusion to assess liver perfusion (Kim et al. 2014), particularly in the evaluation of liver lesions and diseases. Furthermore, CT perfusion extended its reach to areas such as the thorax, abdomen (Hansen et al. 2013, Kanda et al. 2012), myocardium (Kitagawa et al. 2018) and prostate, helping to detect and diagnose tumors throughout the body. This expansion of applications found significance in oncology (Petrulia et al. 2010), facilitating the precise evaluation and delineation of tumors and aiding radiologists in treatment planning.

In particular, CT perfusion has been used in dynamic contrast-enhanced acquisitions of the pancreas to detect pancreatic tumors and diseases (Mathy R. M., Fritz F. , Mayer P., Klauss M., Grenacher L., Stiller W. , Kauczor H.-U., Skornitzke S. 2021, Bao et al. 2019, Kandel et al. 2009). Some studies demonstrated the potential of quantitative perfusion measurements through CT perfusion as important biomarkers for detecting PDAC (Mathy R. M., Fritz F. , Mayer P., Klauss M., Grenacher L., Stiller W. , Kauczor H.-U., Skornitzke S. 2021, O’Malley et al. 2022, D’Onofrio et al. 2013), even in difficult cases that appear isodense to the surrounding tissue on conventional CT images (Delrue et al. 2011), and allow therapy response assessment for treatment of PDAC (Hamdy et al. 2019). Furthermore, CT perfusion can be used to assess the severity of pancreatitis (Bize et al. 2006), as well as to distinguish pancreatic diseases (Gaspard d’Assignies et al. 2009, Hosoki 1983), that is, to improve the difficult differentiation between mass-forming pancreatitis and PDAC (Aslan et al. 2019, Klaus et al. 2013).

1.6 Motivation and background

Several studies have been performed to find optimal study parameters for CT perfusion measurements. These studies have also revealed that the quantitative results of CT perfusion measurements can vary based on CT examination parameters and evaluation procedures, such as depending on the temporal sampling rate (Wintermark et al. 2004, Klotz et al. 2015), the image noise (Skornitzke et al. 2019), the motion correction (Chu et al. 2018, Skornitzke et al. 2015), the mathematical perfusion model (Schneeweiß et al. 2016), and even the employed version of the post-processing software (Goh et al. 2011). That is, based on acquisition parameters and evaluation settings, different quantitative results can be expected for the same measurement, limiting the comparability of measurements between studies and clinical practice (Sanelli et al. 2004, Koell et al. 2021). Therefore, standardization of acquisition protocols and evaluation procedures is necessary to achieve reliable and clinically meaningful measurements. This thesis aims to provide a comprehensive overview of the study parameters and evaluation procedures used in clinical CT perfusion studies of the pancreas employing a quantitative meta-analysis. Additionally, statistical analysis is performed to confirm the results of the individual study on the potential applications of perfusion CT, as well as to identify the acquisition parameters with the strongest influence on the quantitative results for further investigation and standardization.

Furthermore, some studies have highlighted the negative impact of image noise on the precision of CT perfusion measurements (Skornitzke et al. 2019, Juluru et al. 2013). To address this issue, a noise correction algorithm has been developed using the digital perfusion phantoms. Digital phantoms have been preferred for noise correction algorithm development over clinical image data, as the ground truth of actual perfusion measurements are unknown and the measurements are influenced by noise in case of clinical datasets. Therefore, digital perfusion phantoms have been proposed, allowing the generation of image data from known set of pre-defined

Introduction

parameters (Manniesing et al. 2016, Pianykh 2012). With this approach, data can be customized for each study, avoiding problems of clinical CT perfusion acquisitions, such as radiation exposure to patients, image noise of unknown magnitude, or patient motion. In this approach, a noise correction algorithm has been developed using the digital perfusion phantoms to quantitatively evaluate and correct the influence of image noise on the accuracy of CT perfusion BF measurements. Furthermore, the results obtained using the phantom are applied to retrospectively validate the developed algorithm on an earlier CT perfusion study dataset and provide an estimate of the precision of the measured parameters.

In addition, the relatively high radiation exposure to patients during CT perfusion acquisition limits its clinical use. It has been reported that the radiation dose associated with CT perfusion is often significantly greater than that of a standard unenhanced or contrast-enhanced CT scan, primarily due to the extended duration of the scan. For instance, Mnyusiwalla et al. found that CT perfusion assessments for acute stroke patients resulted in an average effective dose of 4.9 mSv, which is approximately twice the radiation dose encountered in a routine head CT examination (Mnyusiwalla et al. 2009). Subsequently, with advances in CT technology, such as increasing spatial coverage, the radiation dose in CT perfusion is approximately 3 times higher than that of a routine CT examination of the head (Abels et al. 2011). Therefore, lowering radiation dose in CT perfusion while preserving essential diagnostic information is critical.

Nonetheless, previous studies have endeavored to reduce radiation dose by reducing tube voltage, reducing temporal sampling, employing iterative reconstruction, or exploring dual-energy CT quantitative iodine concentration maps as potential alternatives to traditional CT perfusion (Stiller et al. 2015, Donahue & Wintermark 2015, Nakayama et al. 2005, Xie et al. 2013). Although CT perfusion is commonly used to evaluate pancreatic tumors, some research has shown that MRI can also provide quantitative perfusion parameters using techniques such as intra-voxel incoherent motion (IVIM) or diffusion-weighted MRI (Mayer et al. 2021, Do R. K., Reyngold M., Raudyal R., Oh J. H., Konar A. S., LoCastro E., Goodman K. A., Dave A. S. 2020, Luna et al. 2016), with similar diagnostic performance for pancreatic adenocarcinoma but without associated radiation exposure (Mayer et al. 2021, Chen et al. 2016, Kovač et al. 2019). Overall, these dose-reduction approaches have been shown to be effective in reducing radiation doses in CT perfusion imaging while maintaining diagnostic accuracy. However, it is important to note that each approach has its own limitations and potential trade-offs. Regardless, CT perfusion remains the preferred choice for quantitative perfusion measurements due to its cost-effectiveness, speed, and widespread availability (Chen et al. 2016). Over time, various mathematical models have been developed to calculate the tissue perfusion parameters from dynamic CT scans, translating tissue TAC into physiological parameters such as BF, BV, permeability, and MTT (Miles & Griffiths 2003). Although this physiological information helps in the diagnosis of pancreatic disease, it also requires multiple volume acquisitions to obtain perfusion

measurements, leading to relatively high radiation exposure.

An approach to reducing radiation exposure in CT perfusion is the dynamic CT perfusion model with first-pass analysis (FPA), which requires only two acquisitions at two-time points (Hubbard et al. 2018, Zhao et al. 2020). This potentially significantly reduces radiation exposure. The FPA technique has previously been implemented for myocardial perfusion measurements in phantom and animal studies (Hubbard, Malkasian, Zhao, Abbona & Molloy 2019, Hubbard et al. 2022, 2016). Studies have also shown the potential of the FPA technique in the diagnosis and detection of pulmonary diseases. Hubbard et al. have implemented a timing optimization technique for the two-volume scans required for the FPA perfusion measurement. They proposed a mathematical relationship between contrast bolus injection time and contrast bolus time to peak for the prospective acquisition of the two first-pass volume scans (Hubbard, Malkasian, Zhao, Abbona & Molloy 2019). However, to date, no studies have investigated the potential of the FPA technique in the diagnosis of pancreatic diseases. This thesis aims to validate the FPA technique for the accurate detection and diagnosis of pancreatic adenocarcinoma and optimize the timing of the two-volume scans required for clinical application in the pancreas. To this end, the FPA technique was to be validated against MSM.

1.7 Objectives

The overarching goal of this thesis is to optimize and standardize CT perfusion technique and enhance our understanding and application of CT perfusion in oncologic imaging specifically, pancreas. Therefore, this thesis begins with a comprehensive quantitative meta-analysis of clinical CT perfusion studies of the pancreas, with a focus on evaluating study parameters and evaluation procedures. Additionally, statistical analysis will be employed to confirm the findings from individual studies regarding potential applications of perfusion CT. Furthermore, the aim is to identify the acquisition parameters that exert the most significant influence on quantitative results, facilitating further investigation and standardization.

In addition, an algorithm has been developed using the digital perfusion phantoms to quantitatively correct the impact of image noise on the precision of CT perfusion BF measurements. Furthermore, the algorithm developed will be validated using clinical data of pancreatic adenocarcinoma patients from a previous CT perfusion study, providing an estimate of the accuracy of the measured perfusion parameters.

Furthermore, this research aims to investigate and validate a low radiation dose alternative to CT perfusion, FPA technique for the accurate detection and diagnosis of pancreatic adenocarcinoma and optimize the timing of the two-volume scans required for clinical application in pancreatic imaging, comparing it against the reference CT perfusion method, MSM to assess its effectiveness and reliability.

1.8 Structure

The following chapters will first provide the materials and methods related to the meta-analysis, the development of noise correction algorithm and the implementation of FPA in Chapter 2. Subsequently, the results of these evaluations will be provided in Chapter 3. Chapter 4 will focus on discussing the results and the conclusions drawn from the thesis. Finally, Chapters 5 and 6 will offer a concise summary in English and Zusammenfassung in German, respectively, encompassing the thesis's objectives, methods used, the attained results, and a comprehensive discussion.

1.9 Contribution of others

This research project was supported by the German Federal Ministry of Education and Research (BMBF) under Grant number 031L0163. The patient data used in this thesis was acquired at the Clinic for Diagnostic and Interventional Radiology, University Hospital Heidelberg, Germany by experienced radiologists (Dr. Philipp Mayer, Dr. Franziska Kortes (previously named as Franziska Fritz), Prof. Dr. Miriam Klauß, Prof. Dr. Lars Grenacher). Regions of interest (ROIs) on the patient dataset were marked by an experienced abdominal radiologist (Dr. Franziska Kortes). The research articles for the meta-analysis were collected, compiled, and assessed for data extraction by me and my doctoral supervisor (Dr. Stephan Skornitzke) individually to eliminate any potential bias. An in-house software developed by my doctoral supervisor (Dr. Stephan Skornitzke) was used for the computation of MSM perfusion maps (Stiller et al. 2015).

Imagination is more important than knowledge. For knowledge is limited, whereas imagination embraces the entire world, stimulating progress, giving birth to evolution.

Albert Einstein

2

Materials and methodology

In this chapter, a detailed description of the materials used and the methods developed in this thesis will be provided. This chapter includes the meta-analysis of CT perfusion within the context of pancreatic research articles as described in (Skornitzke, Vats, Mayer, Kauczor & Stiller 2023). Additionally, it explores the intricacies of correcting noise in blood flow (BF) perfusion measurements by using digital perfusion measurements, followed by the implementation of a novel CT perfusion technique, referred to as FPA (Vats et al. 2023).

First, information on data set collection, process of image acquisition, and inclusion-exclusion criteria for including a suitable data set for this study is provided in Section 2.1. ROI markings on the pancreatic parenchyma and carcinoma regions within the dynamic CT images of the selected data set are thoroughly explained in Section 2.2. The information about the data extracted from the research articles has been provided in Section 2.4. Moving forward, the statistical analysis performed on the data extracted from the research articles is provided in Section 2.5. In addition, Section 2.6 details the noise correction approach for correcting BF measurements with the help of digital perfusion phantoms and includes subsequent statistical analyses and validations. Following this, the implementation of the low-dose FPA technique in CT perfusion, along with its validation process using the MSM model, is explained in the following Section 2.7. The statistical results derived from the FPA analysis and the calculation of radiation dose and acquisition time using the FPA technique are presented in further detail in Sections 2.7.4 and 2.7.5.

In addition, a comprehensive view of supplementary methods and analysis techniques beyond the primary focus of this thesis is provided in the Appendix. A comprehensive overview of the study design is provided by a flow chart in Figure 2.1.

2.1 Dataset

2.1.1 The search strategy for research articles

A comprehensive search in the PubMed database using specific keywords 'pancreas' or 'pancreatic', 'dynamic' or 'perfusion', and 'computed tomography' or 'CT' was conducted. The search objective was to identify published studies related to CT perfusion of the pancreas with a focus on evaluating study parameters and evaluation procedures. The aim was to identify the acquisition parameters that exert the most significant influence on quantitative measurements and to determine the spectrum of parameters used, and to use those values as reference values for the development of a noise correction algorithm. The main focus was specifically on the research articles published and indexed before July 3, 2020, resulting in a total of 491 articles published from 1982 to 2020. To ensure the relevance of these articles, each article was initially screened by reviewing their titles and abstracts, ultimately identifying 117 eligible studies. In the subsequent step, all suitable studies were then read and assessed independently by a medical physics PhD student and a medical physics PostDoc, who possesses extensive experience in the field. Any discrepancies or disagreements regarding the inclusion or exclusion of studies were resolved through consensus-based discussions in two cases. This rigorous process was carried out to compile a complete and accurate data set from relevant research on pancreatic CT perfusion.

2.1.1.1 Inclusion and exclusion criteria for research articles

In the selection criteria, the research studies meeting the following conditions were ultimately incorporated into the analysis:

1. reported original data,
2. included original human data,
3. included a minimum of five datasets, or more,
4. included measurements of the pancreas or pancreatic pathologies, and
5. reported quantitative perfusion parameters derived from CT perfusion

All study designs, both prospective and retrospective, were included. Studies featuring cohorts that exhibited overlap with previously published research were excluded as they did not contribute original data. Articles reporting different perfusion measurements for the same patient collective were consolidated as a single study since patient data were acquired only once. Reviews, animal studies, case reports, and studies with less than five patients were excluded from consideration. To

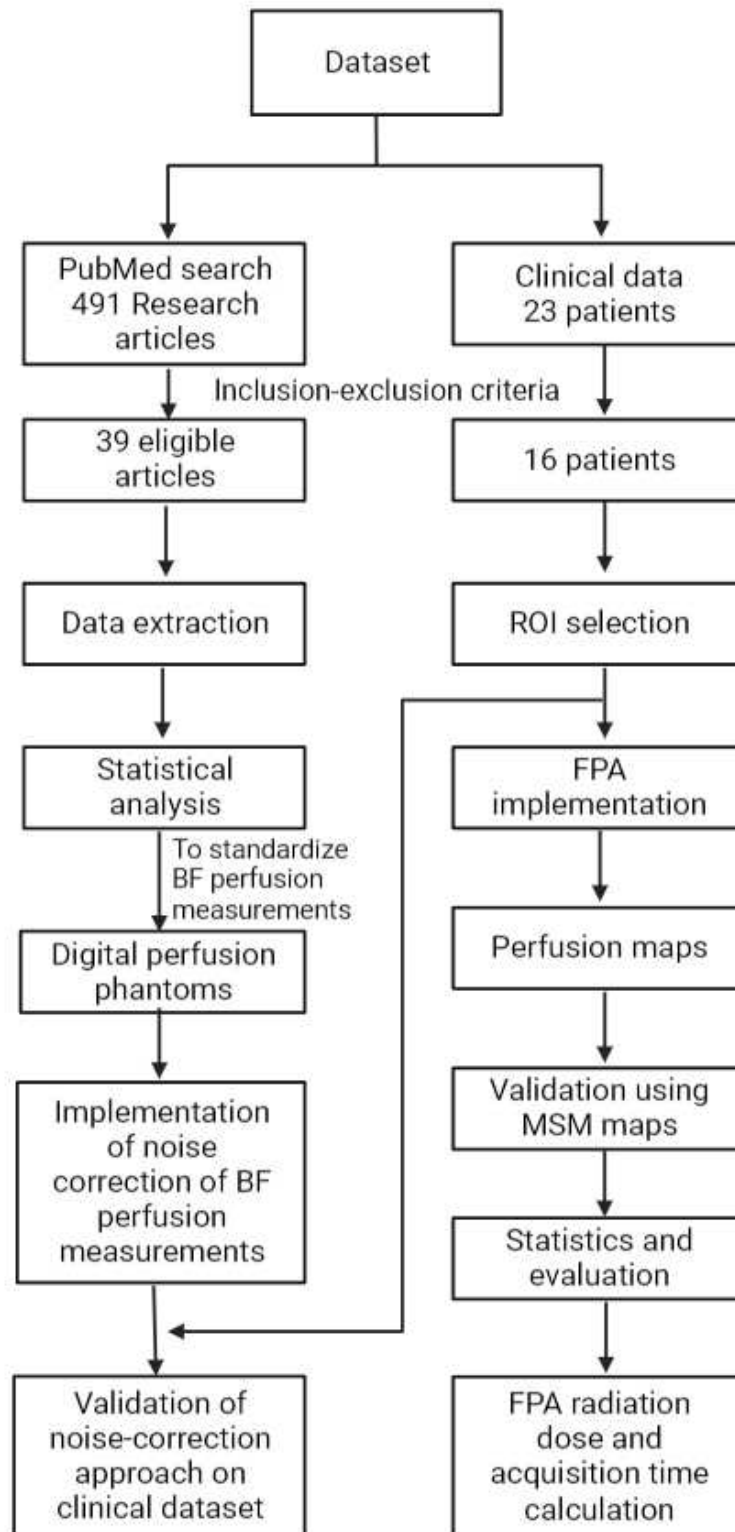


Figure 2.1: Flowchart illustrating a basic overview of the thesis

Materials and methodology

effectively distinguish perfusion CT from conventional contrast-enhanced CT studies, only studies reporting quantitative perfusion parameters were included. Although both CT perfusion and contrast-enhanced multiphase CT involve contrast-enhanced imaging techniques, they serve different purposes. CT perfusion focuses on assessing blood flow and tissue perfusion in a specific organ like the pancreas, while contrast-enhanced multiphase CT captures images at various time points to provide detailed information about vascular structures and tissue enhancement patterns in different phases. Contrast-enhanced multi-phase CT includes scanning at various phases such as arterial, portal venous, and delayed phases to obtain tissue enhancement. Therefore, studies including contrast-enhanced multiphase CT were excluded from the meta-analysis. Consequently, a total of 39 articles, encapsulating 37 distinct studies, were ultimately incorporated into this thesis.

2.1.2 Clinical dataset

In this retrospective analysis, data from 23 patients diagnosed with pancreatic adenocarcinoma, comprising 13 females and 10 males, as detailed in the study conducted by Mayer et al. in 2021, (Mayer et al. 2021) were systematically examined. The study protocol was approved by the local ethics committee of the Heidelberg University Hospital and was conducted in accordance with the ethical standards of the World Medical Association (Declaration of Helsinki). All subjects provided written informed consent before undergoing CT scanning for study participation.

2.1.2.1 Acquisition of clinical dataset

The contrast-enhanced dynamic abdominal CT acquisitions were performed using a dual-source dual-energy CT scanner (SOMATOM Definition Flash; Siemens Healthineers, Germany). Preceding the dynamic acquisition, 80 ml of non-ionic iodinated contrast agent (Ultravist 370; Schering, Germany) was intravenously injected at a rate of 5.0 ml/s, followed by a 40 ml bolus of saline solution (NaCl). The dynamic CT acquisition started with a delay of 13 seconds after the initiation of the contrast-agent injection. The image acquisition consisted of 34 axial dynamic CT acquisitions with a temporal spacing of 1.5 seconds, over a period of 51 seconds (acquisition time 0.5 seconds, cycle time 1.5 seconds) at a tube voltage of 80 kVp/140 kVp using automated tube current modulation with reference values of 270 mAs/ 104 mAs. The scan coverage was 19.2 mm. Image reconstruction was performed using a soft tissue kernel B30f and 0.6 mm slice thickness. The detailed dynamic CT acquisition protocol for abdominal CT is described in Table 2.1.

2.1.2.2 Inclusion and exclusion criteria of clinical dataset

The study employed specific inclusion and exclusion criteria for patient selection. The inclusion criterion required identifying cases of pancreatic adenocarcinoma in prior clinical examinations, while the exclusion criteria encompassed patients with previous treatment of pancreatic adenocarcinoma, suspicion of hypervascular

Dynamic CT acquisition protocol	
Contrast agent	Ultravist 370
Contrast volume (ml)	80
Injection rate (ml/s)	5
Gantry rotation time (s)	0.5
Cycle time (s)	1.5
Delay (s)	13
Scan type	axial
Tube potential (kVp)	80/ 140
Tube current-time product (mAs)	270/ 104
Number of acquisitions	34 dynamic
Total acquisition time (s)	51
Temporal spacing (s)	1.5
Scan coverage (mm)	19.2
Slice thickness (mm)	0.6
Collimation (mm)	34 * 0.6
Reconstruction kernel	B30f

Table 2.1: Acquisition protocol for the contrast-enhanced dynamic abdominal CT

tumors, manifested hyperthyroidism, decreased kidney function, known hypersensitivity to the iodinated contrast agent, inability to reproduce the required breathing technique, and/or denial of consent, as previously described in Mayer et al.’s work, (Mayer et al. 2021).

The application of these exclusion criteria resulted in the exclusion of four patients due to histological diagnoses other than pancreatic adenocarcinoma and three patients due to excessive breathing motion during dynamic data acquisition. As a result, the final analysis included 16 out of the initial 23 patients. The detailed

Materials and methodology

demographic characteristics (Mayer et al. 2021, Skornitzke, Mayer, Kauczor & Stiller 2023) of these 16 patients are summarized in Table 2.2.

Patient demographics	
Number of patients	16
Pathology	Pancreas
Tumor type	Pancreatic adenocarcinoma
Median age (interquartile range)	61.5 (54–79 years)
Sex	
Female	9
Male	7
Tumor location	
Pancreatic head	14
Pancreatic body/ tail	2
Grading	
G1	0
G2	8
G3	4
Not available	4
T stage (Tumor)	
T1	1
T2	7
T3	4
Not available	4

M stage (Metastasis)	
M0	12
Not available	4
N stage (Node)	
N0	3
N1	3
N2	6
Not available	4

Table 2.2: Demographic information of pancreatic adenocarcinoma patients

2.2 Region of interest (ROI) selection

ROIs were marked on the dynamic CT images by an experienced abdominal radiologist (refer to Figure 2.2). A reference image was selected from the dynamic CT image series of a patient containing both non-neoplastic pancreatic parenchyma and carcinoma within the same slice. The entire pancreatic region was demarcated by a polygonal ROI (ROI1 - highlighted in yellow) using an in-house build software (Pahn et al. 2016). For precise delineation of specific areas, additional polygonal ROIs (ROI4 and ROI5 - distinguished in blue) were meticulously drawn around the carcinoma and pancreatic parenchyma, encapsulating each tissue separately. Circular ROIs (ROI2 and ROI3 - marked in pink) were strategically positioned within the polygonal ROIs, ensuring exclusive inclusion of the respective tissue types with a high level of confidence and excluding surrounding tissues or blood vessels. Moreover, to measure the AIF, a circular ROI was placed inside the abdominal aorta of the reference image. Subsequently, these meticulously defined ROIs were replicated from the reference image to all other images of the dynamic series of individual patients. Figure 2.2 visually represents the ROIs marked on a dynamic CT image of a patient diagnosed with pancreatic adenocarcinoma, while Table 2.3 provides a comprehensive overview of the sizes of the marked ROIs on the dynamic CT images. This meticulous approach ensures precision in the analysis of CT perfusion parameters in pancreatic research studies.

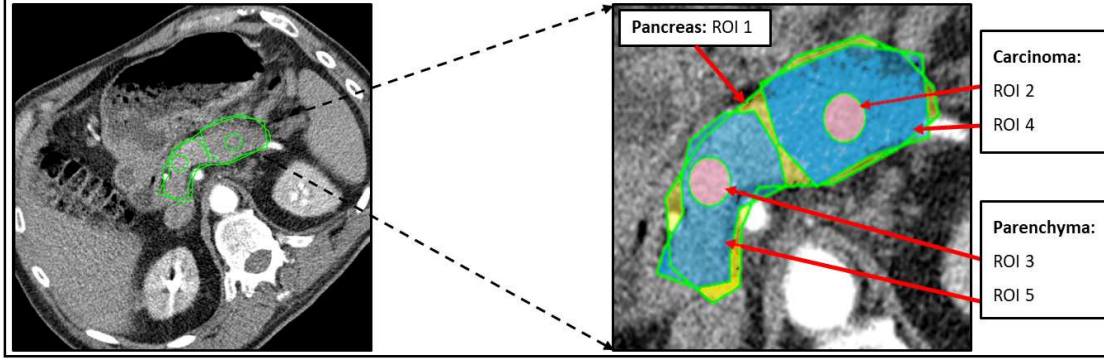


Figure 2.2: Dynamic CT image from the dynamic CT sequence of a pancreatic adenocarcinoma patient with marked regions of interest (ROIs). The entire pancreatic region is delineated by polygonal ROI1 in yellow, while the carcinoma region is marked by polygonal ROI4 in blue. Within the carcinoma region, a small circular ROI2 in pink is specified to encompass only carcinoma tissue, excluding surrounding tissues or blood vessels. Similarly, the parenchyma region is identified by a polygonal ROI5 in blue, and within it, a small circular ROI3 in pink is placed to encompass solely parenchyma tissue, excluding any other tissues or blood vessels. This detailed annotation provides a comprehensive understanding of the specific areas of interest within the dynamic abdominal CT image

ROI sizes [mean \pm SD] (mm ²)	
Circular ROI	
Carcinoma (ROI2)	97.3 \pm 47.9
Parenchyma (ROI3)	76.0 \pm 47.4
Polygonal ROI	
Carcinoma (ROI4)	763.5 \pm 576.0
Parenchyma (ROI5)	2508.3 \pm 1105.8

Table 2.3: An overview of the dimensions of the Region of Interest (ROI) delineated on the dynamic CT image

2.3 Motion correction of the clinical dataset

During the acquisition of dynamic CT images, the patient's breathing motion may cause spatial misalignment. This misalignment can lead to inaccurate perfusion measurements. To address this misalignment, motion correction becomes crucial. In this process, all images from the dynamic series are registered to a common

reference image, aiming to restore spatial alignment across different acquisitions. Various motion correction algorithms have been proposed in the literature. However, in this thesis, motion correction was performed using an in-house developed software. The software utilizes a deformable motion correction technique for dynamic CT images, as detailed by Skornitzke et al. (Skornitzke et al. 2015). Any acquisitions that could not be successfully registered to the chosen reference image were systematically excluded from the subsequent evaluation, ensuring the accuracy of the perfusion measurements.

2.4 Data extraction from research articles

Data extraction from all included research studies was conducted collaboratively by a medical physics PhD student and a medical physics Postdoc, who possesses extensive experience in the field. The extraction process was carried out independently, and any disagreements in data extraction were addressed through consensus-based discussions, successfully resolving disagreements in five instances. The extracted data included study parameters and reported mean values of quantitative perfusion parameters such as BF, BV, and permeability. The selection of these parameters was guided by their relevance to perfusion analysis based on the established guidelines as outlined by Miles et al. (Miles et al. 2012), to ensure that the chosen parameters align with established standards and enhance the credibility of the data extraction process. The study parameters extracted were:

1. Sample size
2. CT examination parameters
 - (a) Acquisition parameters
 - i. Tube potential
 - ii. Tube current-time product
 - iii. Anatomical coverage
 - iv. Total acquisition time
 - v. Lowest temporal sampling
 - vi. Highest temporal sampling
 - vii. Use of variable temporal sampling
 - (b) Reconstruction parameters
 - i. Slice thickness
 - (c) Contrast agent information
 - i. Amount of contrast agent
 - ii. Iodine concentration
 - iii. Total amount of iodine
 - iv. Injection rate
 - v. Use of saline flush

Materials and methodology

- (d) Dose information
 - i. Effective dose
- 3. Post-processing information
 - (a) Perfusion model
 - (b) Types of post-processing software

Many studies used various temporal sampling rates; for example, some studies adopted a sampling rate of one acquisition per second during the initial 30 seconds, followed by a sampling rate of one acquisition every 5 seconds for the subsequent 60 seconds. Therefore, the lowest temporal sampling rate and the highest temporal sampling rate employed in each study were considered separately for individual analysis.

Subsequently, all the quantitative measurements reported in these studies were categorized into four distinct groups to determine if there were statistical differences among parameters within these pathologies. This categorization was based on the clinical entities highlighted and examined within the respective studies. The four resulting categories based on the clinical entities reported in these studies were as follows:

1. **Normal pancreas:** This category encompasses individuals without any pancreatic pathology and incorporates measurements obtained from non-pathologic pancreatic tissue, parenchyma.
2. **Pancreatitis:** Studies including patients diagnosed with pancreatitis, that is the inflammation of the pancreas, were included in this group.
3. **PDAC:** This category was dedicated to studies incorporating patients with PDAC, a common type of pancreatic cancer (refer to Section 1.2).
4. **Non-PDAC:** This grouping covers various pathologies other than pancreatitis and PDAC. Conditions such as insulinoma or endocrine tumors (refer to Section 1.2) were included, despite their physiological distinctions, due to the limited number of studies available for each specific pathology.

2.5 Statistical analysis of data extracted from research articles

To ensure data integrity, the outliers were systematically excluded by applying the criterion of $\text{mean} \pm 1.96 * \text{standard deviation (SD)}$ of parameter values. This rigorous approach was adopted due to the presence of studies reporting exceptionally high measurement values. Following outlier exclusion, the statistical analysis was performed using Excel 2016 (Microsoft Corp.) and SAS software (version 9.2, SAS Institute, Cary, N.C., USA). For all the study parameters mentioned in Section

2.4, histogram distribution plots were calculated for qualitative analysis of the parameter distributions. Medians and interquartile ranges (IQRs) were computed. The year-wise means were determined for the number of studies, sample size, and CT examination parameters. Linear regression plots were used using these mean values to analyze trends in these study parameters over the years.

Additionally, mean values and standard deviations of reported perfusion values were calculated for each pathology. A weighted analysis of variances (W-ANOVA) was performed to compare the mean values of the reported perfusion values of different pancreatic pathologies to each other while weighting the measurements by the number of patients in the individual study. Since the number of patients in each study might vary, weighting the measurements by the number of patients in each study ensures that studies with larger sample sizes have more influence on the analysis, thereby reducing bias. Following the W-ANOVA, a Student's t-test was performed to compare the reported perfusion values of different pancreatic pathologies to each other. Using the t-test in conjunction with W-ANOVA was to identify any statistically significant differences in reported perfusion values between specific pairs of pancreatic pathologies, providing insights into potential variations in perfusion characteristics across different pathological conditions.

Subsequently, a comprehensive weighted analysis of covariance (W-ANCOVA) was performed to evaluate the effect of individual CT examination parameters on the reported perfusion values, simultaneously taking into account the influence of various clinical entities. In this case, the individual CT examination parameters serve as the continuous variables known as covariates. W-ANCOVA helps in addressing for the potential confounding factors introduced by these parameters when evaluating the relationship between reported perfusion values and clinical entities. It's important to note that significance was determined at the conventional threshold of $p < 0.05$.

A qualitative box-plot analysis was performed for those CT acquisition parameters that showed a statistically significant effect on the quantitative measurements with respect to the pancreatic pathologies. To this end, quantitative measurements were separated into two groups based upon CT acquisition parameters (i.e., for each acquisition parameter, a low-value and a high-value group), where the threshold value between the two groups was determined using the K-means clustering algorithm, visualizing differences in quantitative measurements based on acquisition settings. Moreover, a comparative evaluation of total acquisition time and the effective dose was undertaken between studies employing single temporal sampling and those utilizing variable temporal sampling. This comparative analysis was executed using the Student's t-test to discern any significant differences between the two sampling approaches.

2.6 Noise-correction of BF measurements

To address the negative impact of image noise on the accuracy of CT perfusion BF measurements, a noise correction algorithm was developed. This algorithm was developed using digital perfusion phantoms, which are the computational simulations representing an organ or tissue system in the form of digital data, that is, image data. Digital phantoms are preferred over physical phantoms, where the phantom is a physical object instead of digital data, due to their ability to simulate a wide range of scenarios, cost-effectiveness, and easy availability. These digital phantoms were designed to replicate CT perfusion imaging conditions, allowing a quantitative assessment of the impact of image noise on the precision of CT perfusion BF measurements. Although dynamic CT data offers valuable perfusion information, it can often be challenging to interpret due to variations in acquisition protocols and patient physiology. Furthermore, the absence of a definitive ground truth for the actual BF and the influence of noise complicate the accuracy of the measurements. To address these issues, digital perfusion phantoms were proposed, allowing the generation of CT image data from predetermined parameters as proposed by Manniesing et al. (Manniesing et al. 2016). This approach offers a solution to problems associated with clinical CT perfusion acquisitions, such as radiation exposure to patients, uncertainties related to image noise levels, and patient motion due to breathing.

The noise correction algorithm for perfusion measurements was developed based on the deconvolution based mathematical modeling approach as explained in Section 1.5.4. This approach aimed to generate TACs with well-defined perfusion parameters, considered ground truth parameters. The ground truth parameters were selected on the basis of the results obtained from the meta-analysis. TACs were obtained by forward convolution of the IRF with the AIF and simulated into the digital perfusion phantoms. TACs were specifically generated for both tissue types, i.e., pancreatic parenchyma and carcinoma, based on the predefined set of parameters for each tissue type. The forward convolution is an inverse technique of the deconvolution approach discussed in Section 1.5.4. This technique explains that the concentration of contrast agent or attenuation in the tissue of interest, i.e., TACs can be calculated through the forward convolution of AIF and IRF. The algorithm was implemented using MATLAB R2022a (MathWorks; USA) and the digital phantoms were evaluated on a commercially available workstation (syngo.via Body perfusion VB10B; Siemens Healthineers) using deconvolution (Pahn et al. 2016). This comprehensive noise correction approach using the simulated digital perfusion phantoms aimed to assess and correct noise effects in pancreatic perfusion measurements. The entire process of algorithm development and noise correction of BF measurements is as described below:

Step 1: AIF was obtained by averaging the AIFs from the cohort of 59 pancreatic adenocarcinoma patients. Figure 2.3 shows the resulting AIF after the averaging process.

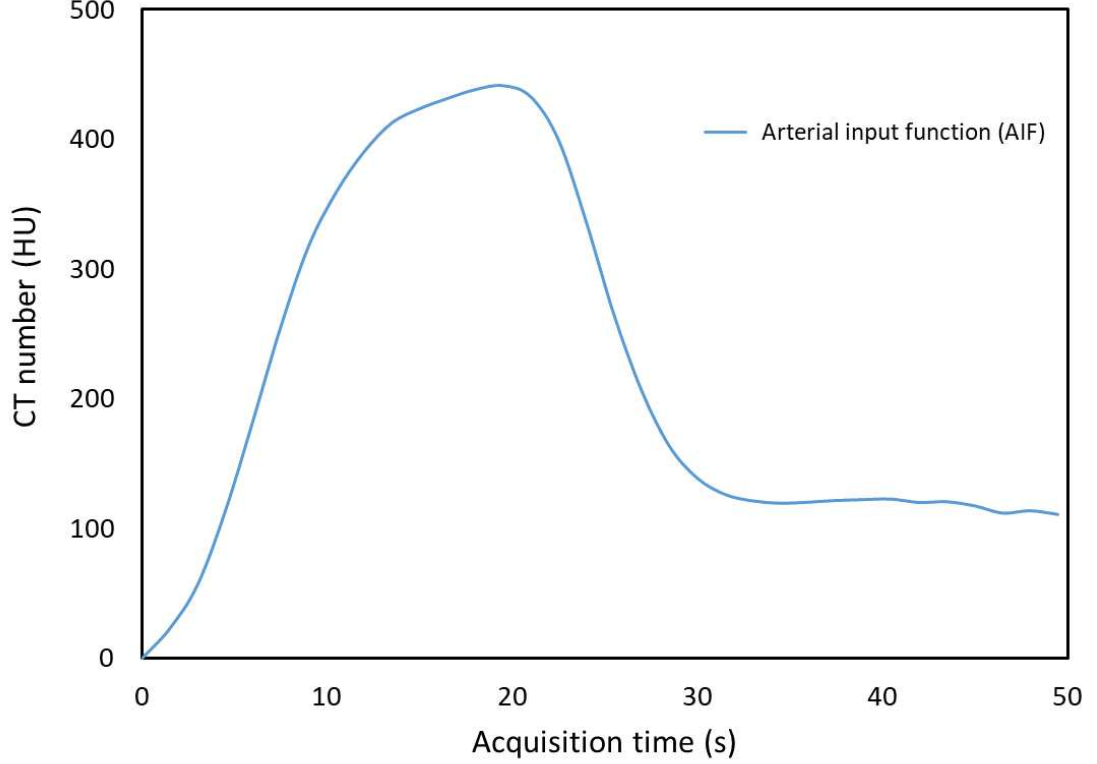


Figure 2.3: An arterial input function (AIF) of a digital perfusion phantom with zero baseline and temporal sampling rate of 1.5 seconds, generated by averaging the AIFs from a cohort of 59 pancreatic adenocarcinoma patients

Step 2: IRF was generated using the function defined by the adiabatic approximation to the tissue homogeneity model as described in equation 1.21.

$$IRF(t) = \begin{cases} 0 & t < TTS \\ F & TTS < t < TTD \\ EF \cdot e^{-EF \frac{t-TTD}{V_e}} & t > TTD \end{cases} \quad (2.1)$$

The ground truth perfusion parameters were chosen to be F (ground truth blood flow is abbreviated as GTBF) of 5-420 ml/100 ml/min, comprising 28 sets, with 14 designated for pancreatic parenchyma and 14 for pancreatic adenocarcinoma. These parameters included fixed values of 0.1, 5 seconds, and 5 seconds for E , TTS , and MTT , respectively. Thus, TTD , denoted as the sum of TTS and MTT , becomes equal to 10 seconds. The ground-truth volume (GTBV) was obtained from the product of GTBF with MTT . Subsequently, V_e was calculated using the equation 2.2

$$V_e = 1 - \frac{GTBV}{100} - 0.02 \quad (2.2)$$

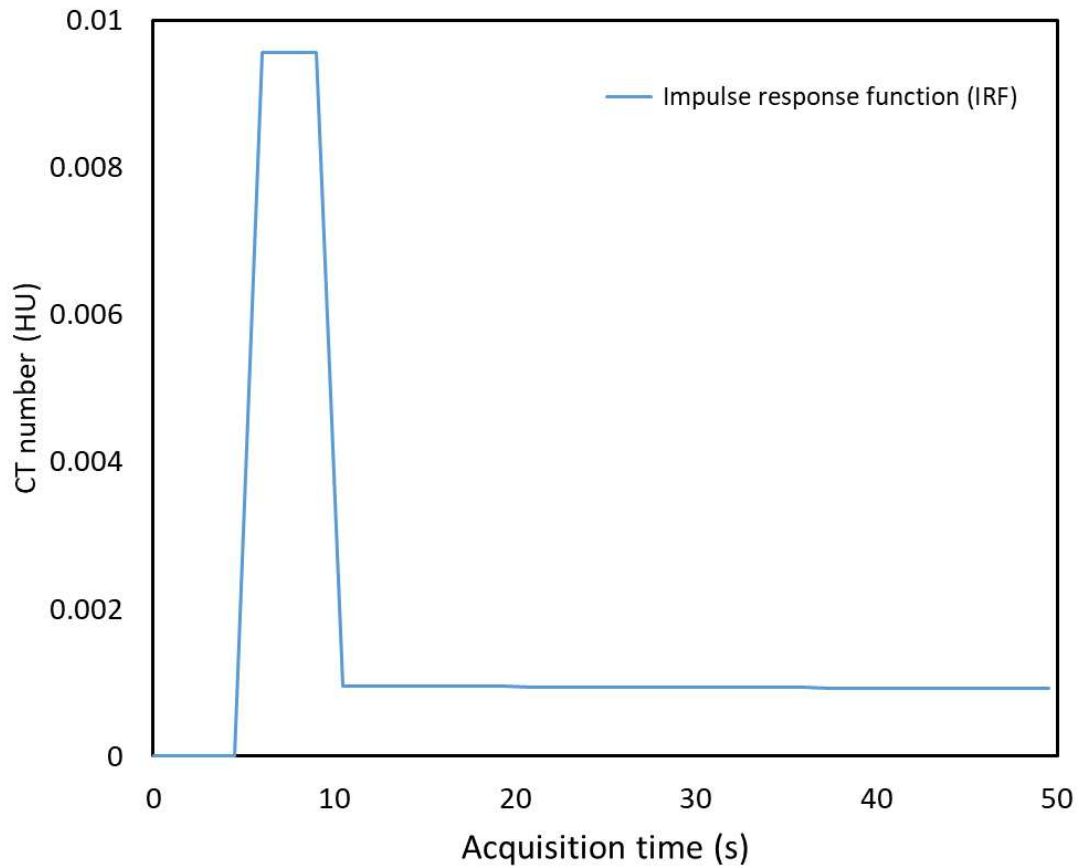


Figure 2.4: An example of an impulse response function (IRF) of a digital perfusion phantom. The IRF was generated using the equations 2.1 and 2.2 in step 2 using the ground truth blood flow (GTBF) of 5-420 ml/100 ml/min, $E=0.1$, $TTS=5$ seconds, and $MTT=5$ seconds. These ground truth values are chosen depending on the meta-analysis results. E is the extraction fraction, TTS is the time to start, and MTT is the mean transit time

These ground truth values were chosen based on the spectrum of parameters obtained from the meta-analysis results. An example of a generated IRF from the above equation is shown in Figure 2.4.

Step 3: As explained by equation 1.22, TACs are the result of the convolution of AIF and IRF. Thus, TACs for digital perfusion phantoms were derived using the following equation 2.3

$$TAC = AIF \otimes IRF \quad (2.3)$$

TACs were specifically created for both tissue types, pancreatic parenchyma, and pancreatic carcinoma, guided by the predefined set of ground truth perfusion parameters. Figure 2.5 shows an example of the TAC generated using the above process for both tissue regions.

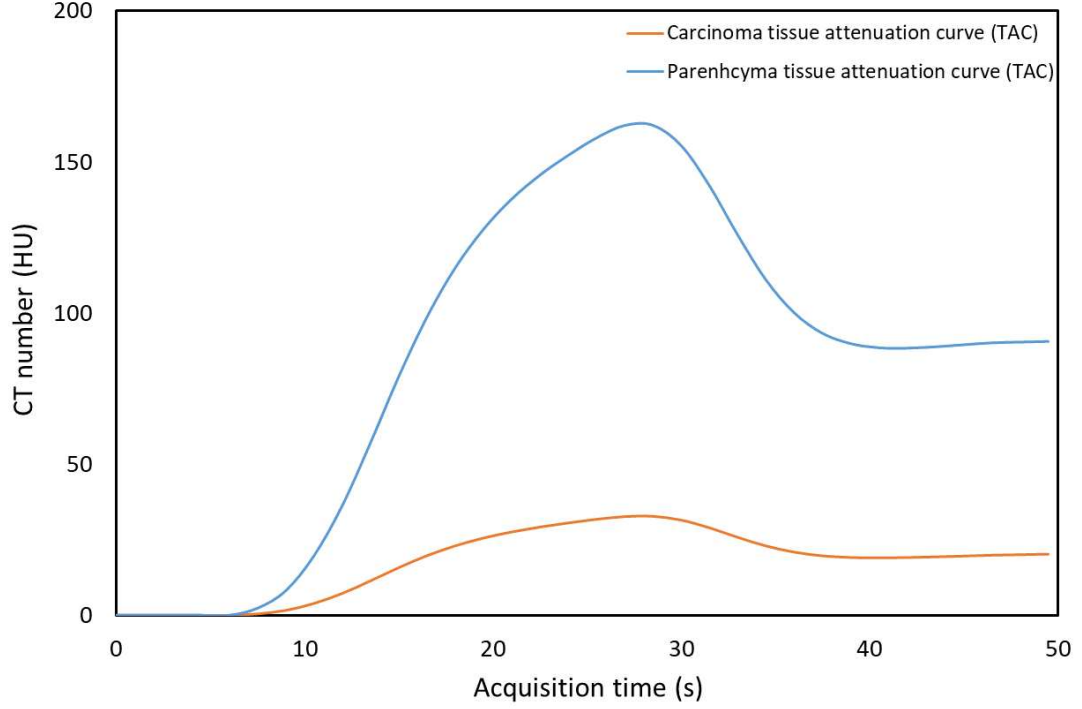


Figure 2.5: An example of tissue attenuation curves (TACs) for a digital perfusion phantom generated using the equation 2.3 for both tissue types, pancreatic carcinoma and parenchyma

Step 4: To investigate the impact of image noise present in CT perfusion acquisitions on perfusion measurements, 2×576 random Gaussian noise samples were introduced into the TACs generated in Step 3. Each random sample had a mean μ of 0 HU and a standard deviation σ of 25 HU. Thus, 2×576 noise-impacted TACs were obtained from a single independent TAC, each with adding random samples of Gaussian noise. Figure 2.6 represents an example of noise-impacted TACs generated for both tissue regions after the introduction of noise to the TACs.

An example of TACs from pancreatic parenchyma and carcinoma tissue regions of a pancreatic adenocarcinoma patient is shown in Figure 2.7.

Step 5: To evaluate these noise-impacted TACs and calculate the perfusion parameters, these TACs were represented in the form of digital images. Each digital image consisted of a 512×512 pixel matrix with 512×504 pixels of size 4×4 , each containing the TACs, and an additional 50×8 pixel region on the right side containing the AIF. The square regions of size 4×4 pixels containing TACs were determined based on the smoothing strength of the CT perfusion software employed. When setting the parameter for smoothing strength to 0 mm, a size of 4-by-4 pixels was the smallest size that would yield pixels containing the expected results (i.e., the 2-by-2 patch in the middle of the region will yield values matching ground truth) undisturbed by filtering when evaluating a digital perfusion phan-

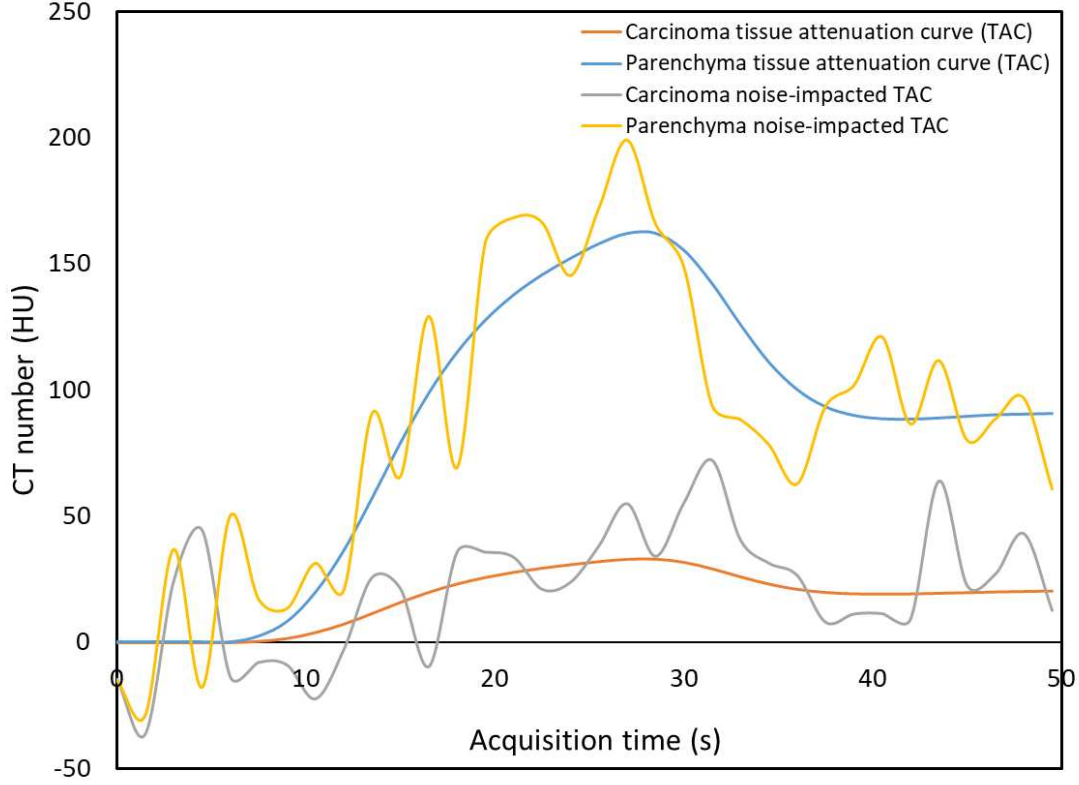


Figure 2.6: An example of noise-impacted tissue attenuation curves (TACs) for a digital perfusion phantom for both tissue types, pancreatic carcinoma and parenchyma

tom (Skornitzke et al. 2019).

A single digital perfusion phantom series is comprised of 34 such digital images made up of 16128 (28 sets of ground truth values * 576 random noise samples) TACs. All phantom images were stored in the DICOM format. DICOM, that is, Digital Imaging and Communications in Medicine, is an international standard protocol for storing and managing medical image data (Mustura et al. 2008, Wikipedia contributors 2023a). A detailed explanation of the DICOM format has been given in the Appendix A. An illustrative example of an image from the DICOM series of digital perfusion is presented in Figure 2.8.

Step 6: These noise-added digital perfusion phantoms were evaluated on a commercially available CT perfusion workstation (syngo.via Body Perfusion by Siemens Healthineers). The evaluation utilized the deconvolution mathematical model, leading to the computation of BF perfusion maps. Subsequently, these BF maps were exported in DICOM format for further analysis. An illustrative example of a BF perfusion map generated from the DICOM series of a digital perfusion phantom is presented in Figure 2.9. The algorithm was developed to correct these noise-impacted simulated BF measurements.

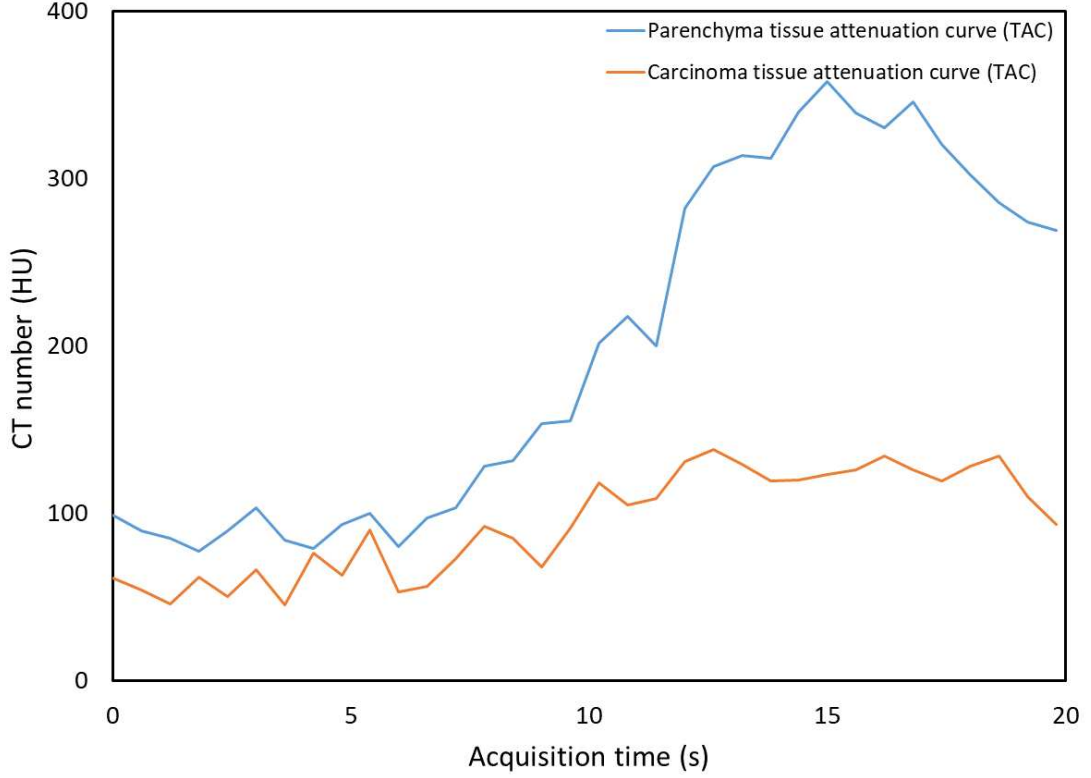


Figure 2.7: An example of tissue attenuation curves (TACs) from pancreatic parenchyma and carcinoma tissue regions of a pancreatic adenocarcinoma patient

The flow chart of the noise correction algorithm is shown in Figure 2.10 for a better understanding of the steps below.

Step 7: BF perfusion maps computed using syngo.via software were then evaluated using the MATLAB-based build software to obtain the perfusion measurements for each TAC, resulting in 16128 BF values (28 sets of ground-truth values multiplied by 576 random noise samples). The process involved calculating the average of 576 BF values derived from 576 TACs within each set. Consequently, 28 noise-affected BF measurements were obtained, represented as BFD. The BF values below zero were truncated (that is set to zero) as the BF measurements have no physiological significance for values below zero. The algorithm is implemented to correct the impact of image noise on these BFD measurements.

Step 8: To correct the impact of added noise on BFD, IRF is computed based on these BFD values. This IRF is convolved with AIF and TACs are obtained (follow Step 3). To address image noise, 2 x 576 random samples of Gaussian noise were introduced to the TACs (Step 4), and 2 sets of digital phantom series were generated. These phantom series were evaluated using syngo.via to obtain

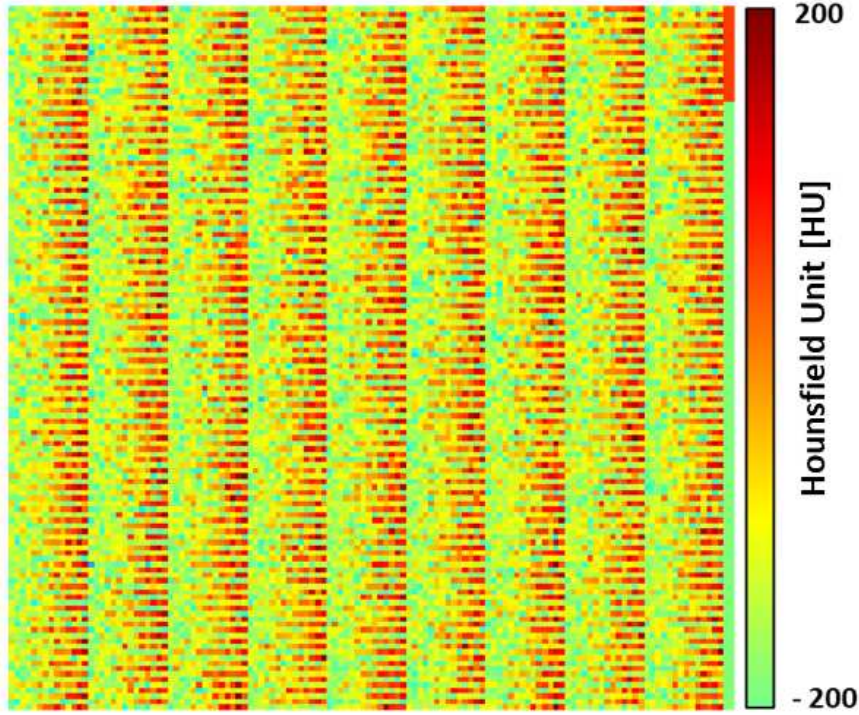


Figure 2.8: An example of an image from the DICOM series of a digital perfusion phantom made up of 16128 (28 sets of ground truth values * 576 random noise samples) tissue attenuation curves (TACs). The top right corner of the phantom image represents the arterial input function (AIF).

BF maps. The 2 sets of noise-impacted BF measurements (BF1, BF2) were calculated based on 2 sets of 576 noise levels to avoid bias due to randomness. The averaging of these two sets was then performed to derive the mean noise-impacted BF (BFavg) measurements.

Step 9: For noise correction, difference between BFD and BFavg was computed as the noise correction in BF perfusion measurements was estimated based on the differences between the BFavg and the BFD measurements. This difference was then added to the noise-impacted BFD to obtain the first noise-corrected BF measurement, BFDcorr1 as illustrated in equation 2.4. The steps 8 and 9 were performed iteratively until the noise-corrected BF value of that iteration (BFDcorr(i)) were closely aligned with the ground truth value ($BFDcorr \approx GTBF$).

$$BFDcorr(i) = BFD + (BFD - BFavg(i)) \quad (2.4)$$

2.6.1 Statistical analysis

Statistical analysis was performed using Excel 2016 (Microsoft Corp.). The absolute differences between the BFDcorr values with each iteration and GTBF were

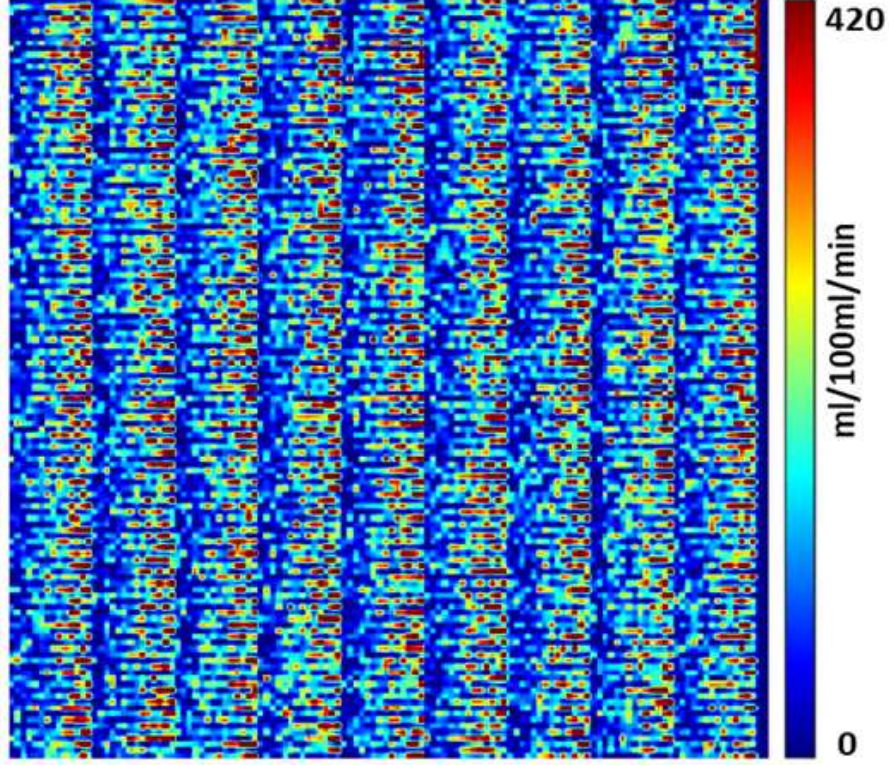


Figure 2.9: An example of a BF map obtained from a digital perfusion phantom using commercially available CT perfusion software (syngo.via Body perfusion VB10B, Siemens Healthineers)

calculated, followed by the calculation of the mean absolute difference and the linear regression analysis for each iteration. Furthermore, the contrast-to-noise ratio (CNR) being the parameter for evaluating the image quality depending on noise was computed with each iteration. The calculation of CNR is explained below from equation 2.5, 2.6, and 2.7.

Mathematically, the CNR is expressed as:

$$CNR = \frac{Contrast}{Noise} \quad (2.5)$$

Where:

- Contrast refers to the difference in signal intensity or contrast between two tissue regions. Therefore, contrast is calculated using average of difference between BFcorr values of carcinoma region from parenchyma region for all simulated datasets.

$$Contrast = \frac{\sum (BFDcorr(Parenchyma) - BFDcorr(Carcinoma))}{number\ of\ datasets} \quad (2.6)$$

- Noise represents random fluctuations or standard deviation in pixel values of the image, that is the average of standard deviations (σ) of parenchyma and

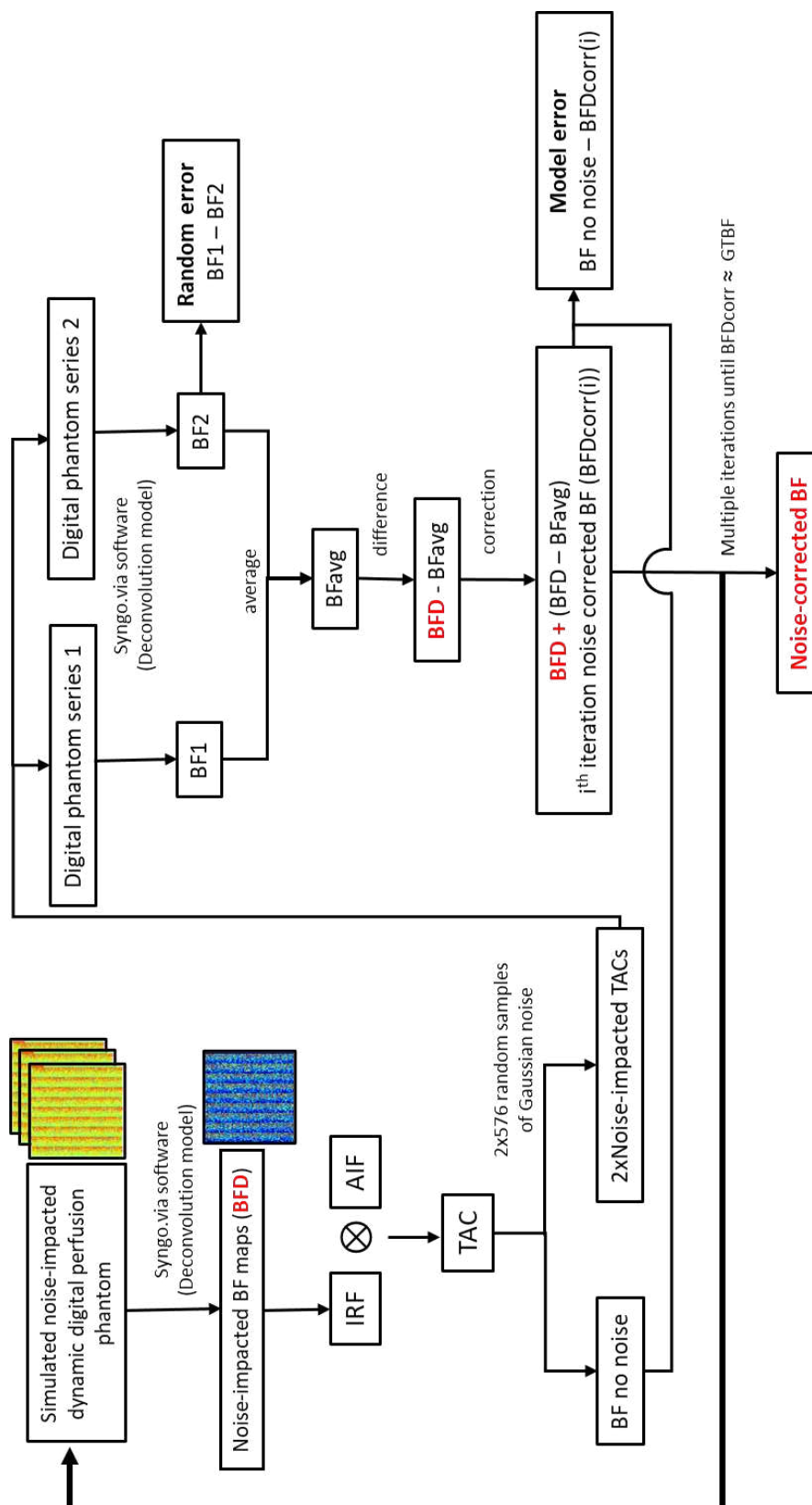


Figure 2.10: The flow chart of the noise correction algorithm. BFD represents the noise-impacted BF measurements computed for simulated digital perfusion phantom, which need to be corrected. IRF is the Impulse response function, AIF is the Arterial input function, TAC represents tissue attenuation curve, and GTBF is the ground truth blood flow. BFDcorr(i) represents the noise-corrected BF measurement for the i^{th} iteration. The random error and model error are also shown in the flow chart. This process is repeated iteratively until $BFDcorr \approx GTBF$

carcinoma tissue regions in this case.

$$Noise = \frac{\sigma_{BFDcorr(Parenchyma)} + \sigma_{BFDcorr(Carcinoma)}}{2} \quad (2.7)$$

Additionally, the model error and the random error were determined for each iteration (see Figure 2.10). Random error calculation involves calculating the absolute difference between BF1 and BF2 with each iteration, as shown in the flowchart. Similarly, the calculation of model error includes the calculation of absolute difference between the BFDcorr value without noise and the noise-impacted BFD value for each iteration (refer to Figure 2.10).

The Bland-Altman analysis was performed to assess the agreement between noise-impacted BFD and noise-corrected BF (BFDcorr) measurements. Simulated BF perfusion values for different pancreatic pathologies i.e., pancreatic parenchyma and carcinoma were compared using a Student's t-test.

2.6.2 Validation

The efficacy of the noise correction algorithm was validated using a clinical dataset 2.1.2 sourced from a prior CT perfusion study (Mayer et al. 2021) involving 14 patients diagnosed with pancreatic adenocarcinoma. Different pancreatic pathological regions, that is, pancreatic parenchyma (ROI3) and carcinoma (ROI2) (refer to Figure 2.2, were analyzed using the algorithm to obtain noise-corrected BF measurements. The noise-impacted BF measurements calculated using the deconvolution model from a previous study (Mayer et al. 2021, Koell et al. 2021) were used for correction and validation of the algorithm.

2.7 First-pass analysis (FPA)

The FPA dynamic CT perfusion model involves a simplified approach with only two volume acquisitions performed at two distinct time points. FPA proposes that the average perfusion (P_{avg}) within a tissue compartment of interest is proportional to the first-pass entry of the contrast material mass into that compartment over time (dM_c/dt), further normalized by the incoming contrast material concentration (C_{in}) and compartment tissue mass (M_t). The underlying assumption in this model is that contrast material does not exit the tissue compartment during measurement duration. This relationship is mathematically expressed in the equation 2.8 (Hubbard et al. 2018)

$$P_{avg} = M_t^{-1} (C_{in}^{-1} \frac{dM_c}{dt})_{avg} \quad (2.8)$$

where dM_c/dt is derived from the integrated change in TACs over time, while C_{in} is approximated from the AIF. Additionally, P_{avg} is proportional to the rate of

Materials and methodology

change in contrast material concentration within the compartment (that is, the average change in tissue attenuation (ΔHU_{avg}) over time). Thus, the voxel-by-voxel perfusion (P_{FPA}), which reflects the perfusion at the level of individual image voxels, can be derived by using the change in voxel-by-voxel concentration (ΔHU) as indicated in equation 2.9 (Hubbard et al. 2018)

$$P_{FPA} = P_{avg} \frac{\Delta HU}{\Delta HU_{avg}} \quad (2.9)$$

The FPA approach only requires two CT volume scans, where the first volume scan should be acquired at the baseline (t_{base}) of the AIF curve while the second one should be acquired at the peak (t_{max}) of the AIF as suggested by Hubbard et al. in their study from 2018 (Hubbard et al. 2018), shown in Figure 2.11. Adapting the proposed acquisitions to the pancreas, the first volume scan at t_{base} was selected when the AIF just exceeds 120 Hounsfield units (HU) (Skornitzke et al. 2018). However, in clinical practice, the timing of the second volume scan at t_{max} is not known before acquisition. Therefore, an approach to approximate the timing of t_{max} in clinical practice was implemented and compared to the theoretical optimum of an acquisition at t_{max} . In this thesis, these two volume scans were retrospectively selected from the 34 dynamically acquired volume scans based on the calculated timing and FPA models were implemented based on the in-house developed software SOPHIA and external software libraries using C++.

2.7.1 FPA approach 1 (FPA1)

In the first FPA implementation (FPA1), the first volume scan was selected as the scan where the contrast agent bolus exceeded the threshold of 120 HU in the abdominal aorta, that is, t_{base} . For the second scan, the acquisition timing where the AIF reached its maximum (t_{max}) was determined retrospectively, according to the theoretical definition stated by Hubbard et al. (Hubbard et al. 2018). Thus, in this approach, volume scans at t_{base} and t_{max} were selected from 34 dynamically acquired volume scans, and were used to calculate FPA1 BF perfusion maps. However, it's important to note that FPA1 is only a theoretically possible technique since the peak of AIF (t_{max}) is not known a priori. The graphical representation of the acquisition timings of FPA1 is illustrated in Figure 2.11.

2.7.2 FPA approach 2 (FPA2)

In the second FPA implementation (FPA2), the scan at t_{base} was selected as the first volume scan, while the timing to select the second scan was adapted from Hubbard et al. (Hubbard, Malkasian, Zhao, Abbona & Molloy 2019). Based on the studies by Garcia et al. (Garcia et al. 1999) and Han et al. (Han et al. 2000), Hubbard et al. proposed that the temporal center of the contrast agent bolus (t_p) maintains the highest contrast agent concentration and peak enhancement of the contrast agent. The timing of this temporal center can be approximated by one-half of the injection time ($t_i/2$) plus a fixed dispersion delay (d), as described by

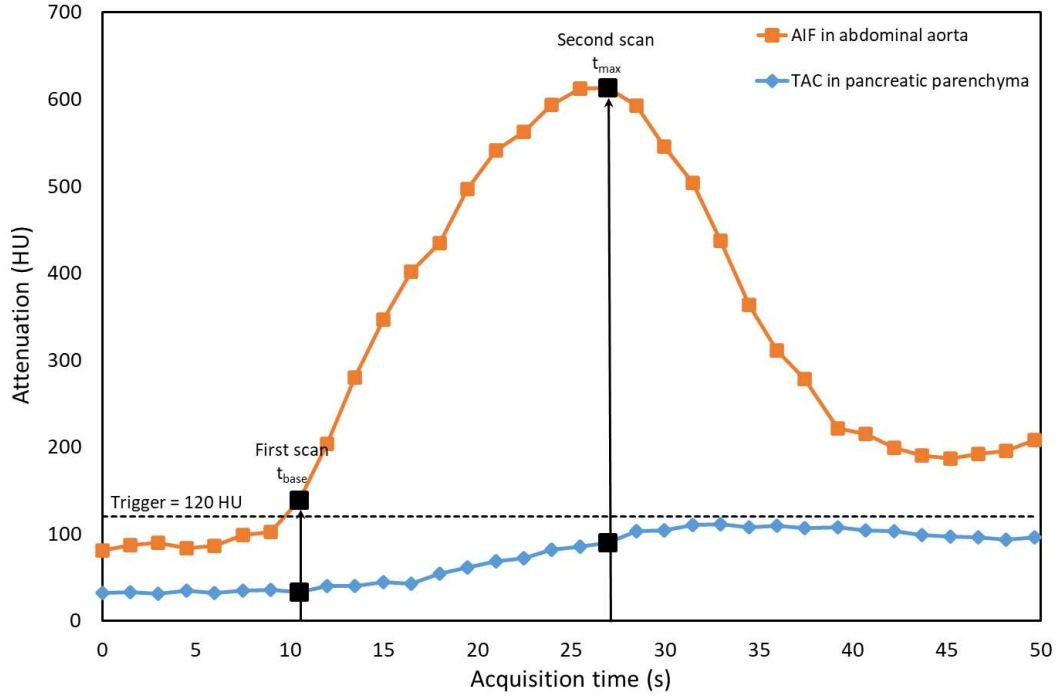


Figure 2.11: First pass analysis 1 (FPA1) acquisition protocol. A tissue attenuation curve (TAC) of an ROI placed inside the pancreatic parenchyma and arterial input function (AIF) in the abdominal aorta. All 34 scans of a dynamic CT acquisition as used in maximum slope model (MSM) are represented by squared boxes on the curves. Two black-colored boxes represent the two-volume acquisitions required in FPA: the first scan is marked after crossing the threshold of 120 HU (t_{base}) and the second scan is marked at the peak of the AIF (t_{max}). t_{base} time of baseline acquisition of AIF, and t_{max} time of peak acquisition of AIF

equation 2.10). The graphical representation of the acquisition timings of FPA2 is illustrated in Figure 2.12.

$$t_p = \frac{t_i}{2} + d \quad (2.10)$$

where t_i is the duration of contrast agent injection, that is, 16 seconds for the clinical data set used in this dissertation, and therefore $t_i/2$, representing half of this duration, equates to 8 seconds. To determine a suitable dispersion delay 'd', perfusion maps were generated using ten different values for 'd', resulting in ten different acquisition times for the second volume scan. Compared to the myocardium, a higher degree of dispersion can be expected for the pancreas; therefore, ten acquisition times (t_1 – t_{10}) were evaluated, contrasting with the five different timings employed by Hubbard et al. (Hubbard, Malkasian, Zhao, Abbona & Molloy 2019). The dispersion delay 'd' was iteratively incremented from 0 to 13.5 seconds with intervals of 1.5 seconds, resulting in a range of t_p values including 8 seconds, 9.5

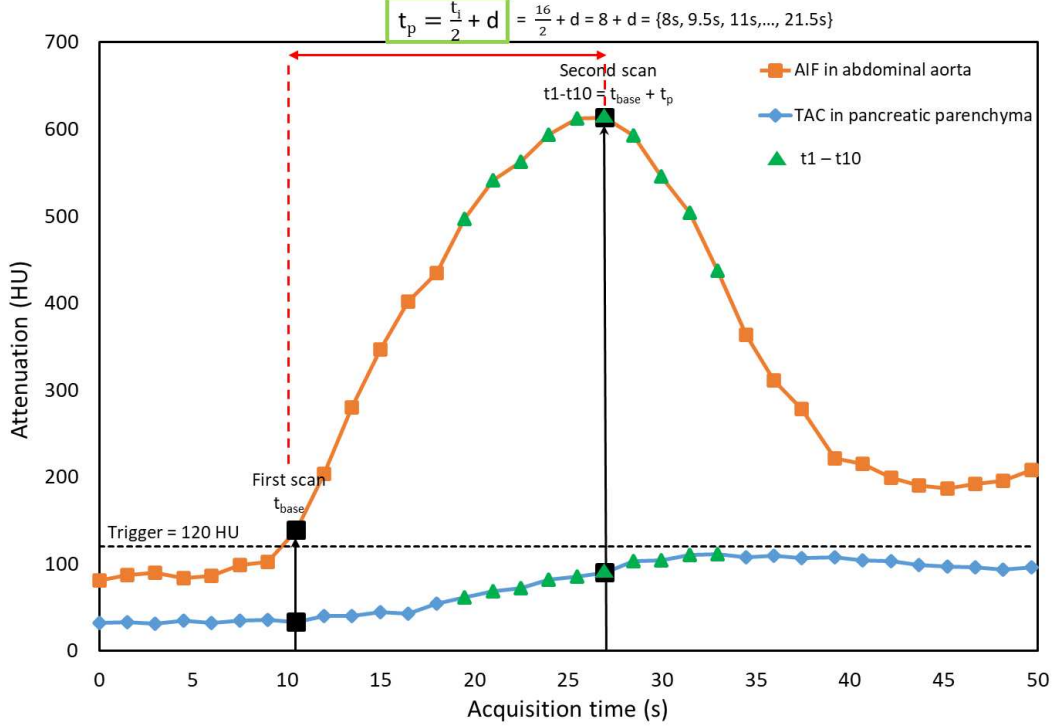


Figure 2.12: First pass analysis 2 (FPA2) acquisition protocol. A tissue attenuation curve (TAC) of an ROI placed inside the pancreatic parenchyma and arterial input function (AIF) in the abdominal aorta. All 34 scans of a dynamic CT acquisition as used in maximum slope model (MSM) are represented by squared boxes on the curves. Two black-colored boxes represent the two-volume acquisitions required in FPA: the first scan is marked after crossing the threshold of 120 HU (t_{base}) and the second scan is taken ' t_p ' seconds after the first scan, as marked by green triangles on the curve from t_1 – t_{10} . ' d ' dispersion delay, t_{base} time of baseline acquisition of AIF, t_i time taken for contrast injection, t_{max} time of peak acquisition of AIF, t_p time at the temporal center of the bolus

seconds, 11 seconds, and so forth, up to 21.5 seconds. Thus, the volume scan at t_p time after the first scan was retrospectively selected as the second scan from 34 dynamically acquired volume scans. BF perfusion maps were computed at ten different acquisition times (t_1 – t_{10}) using the FPA2 CT perfusion approach.

2.7.3 Perfusion maps

BF perfusion maps (ml/100 ml/min) were generated from the 80 kVp images using both the FPA approaches, FPA1 Section 2.7.1 and FPA2 Section 2.7.2. Circular ROIs (ROI2 and ROI3 Section 2.2) were used to assess mean BF perfusion values to ensure a higher degree of confidence relative to the respective tissue types. A more comprehensive voxel-based analysis was performed which allows for the examination of individual voxel within an ROI, providing insights into spatial variability that may not be captured by averaging. For voxel based analysis across the entire

tissue region of each tissue type, polygonal ROIs (refer to Section 2.2) designated as ROI4 and ROI5 were used to obtain BF values for each voxel.

In addition, BF perfusion maps were also computed using the MSM model. These maps were used as a reference for validating the perfusion maps generated through FPA. The MSM method requires all 34 volume scans for perfusion measurement. In this thesis, MSM perfusion maps were generated using in-house build software that implements MSM using a curve fitting model as described previously in (Stiller et al. 2015).

The mean \pm SD was calculated for BF perfusion values obtained using FPA1, FPA2, and MSM, considering both the circular ROIs (ROI2 and ROI3) and the polygonal ROIs (ROI4 and ROI5) for respective tissue regions (refer to Figure 2.2). Circular ROIs focus solely on the designated tissue areas without encompassing other tissues or blood vessels. Thus, BF values calculated using circular ROIs provided a higher degree of confidence in the respective tissue types. In contrast, polygonal ROIs were used for the voxel-based assessment of BF maps.

2.7.4 Statistical analysis

Statistical analysis was performed using Excel 2016 (Microsoft Corporation; USA), SAS software (version 9.4, SAS Institute; USA), and MATLAB R2022a (MathWorks; USA). Mean and SD values of the BF were calculated for ROI2 to ROI5. The differences in BF values between carcinoma and parenchyma tissue were assessed using the student's t-test for the mean values of ROI2 and ROI3, as well as for all voxels included in ROI4 and ROI5. The linear correlation between FPA and MSM measurements was evaluated by calculating Pearson's correlation coefficient (r). Correlation was assessed for the mean values measured in the circular ROIs (ROI2 and ROI3) and also, for all voxels in the polygonal ROIs (ROI4 and ROI5). Coefficient of variation (COV) were calculated to measure the sensitivity of perfusion values to variations in acquisition timing when using FPA2. Box-whisker plots were generated to compare the perfusion values at varying acquisition times and for different tissue regions.

2.7.5 Radiation exposure and acquisition time

The radiation dose to the patients was determined by multiplying the radiation exposure, calculated as DLP, by the conversion factor, k (ICRP 2002, Harrison et al. 2021) for abdominal CT examinations ($k = 0.0153 \text{ mSv/mGy}\cdot\text{cm}$) (Deak et al. 2010), where DLP is the product of CTDIvol with scan length. The acquisition time was estimated by the total amount of time taken for the complete acquisition of all dynamic CT images. The total acquisition time for FPA was estimated from the start of the bolus monitoring to the acquisition time of the second volume scan.

*Science is but a perversion of itself unless it has as
its ultimate goal the betterment of humanity.*

Nikola Tesla

3

Results

The findings of this thesis are outlined in the subsequent chapter. Initially, the findings and results of the statistical analysis from the meta-analysis are presented in Section 3.1. Following that, Section 3.2 illustrates the results of the noise-correction algorithm analysis applied to BF perfusion measurements computed through digital perfusion phantoms. Additionally, the validation results for the noise correction algorithm using the clinical dataset are provided in Section 3.2.2.

Furthermore, Section 3.3 provides the perfusion measurements of both FPA techniques (FPA1 and FPA2), followed by validation results of FPA using MSM in Section 3.3.3. The section also presents the correlation results between FPA and MSM. Afterward, the section provides results about the reduction in radiation dose with reduced acquisition time using the novel FPA technique.

Some of the results of this chapter have already been published by Vats et al. in (Skornitzke, Vats, Mayer, Kauczor & Stiller 2023, Vats et al. 2023, 2024, 2022, 2021).

3.1 Meta-analysis of pancreatic CT perfusion studies

In total, 491 published research articles were collected for the meta-analysis based on the search strategy mentioned in Section 2.1.1. After selection based on title and abstracts, 117 articles were selected for full text screening. Of these, 39 articles reporting 37 studies were finally included in this thesis based on the inclusion criteria mentioned in Section 2.1.1.1. Figure 3.1 shows a flow chart illustrating the selection of studies, inclusion criteria, and data extracted from selected studies for

Results

the meta-analysis.

A summary of information on the number of studies and the corresponding number of patients reporting each quantitative perfusion parameter (BF, BV, and permeability) for the respective clinical entity is shown in Table 3.1.

Number of patients (number of studies)					
Clinical entities		Normal pancreas	Pancreatitis	PDAC	Non-PDAC
Perfusion parameters	Blood flow	30 (983)	10 (281)	20 (591)	4 (231)
	Blood volume	18 (707)	9 (270)	14 (458)	5 (249)
	Permeability	13 (448)	5 (111)	10 (306)	3 (57)

Table 3.1: Number of studies (number of patients) reporting the quantitative parameters (blood flow, blood volume, and permeability) for the respective clinical entity. PDAC - Pancreatic ductal adenocarcinoma

3.1.1 Distribution of study parameters over the years

Figure 3.2 a-l shows the histogram distribution of the study parameters extracted from the selected research articles. Over the years, a broad spectrum of values for numerous parameters has been reported. For example, the number of patients has a median (IQR) of 36.0 (27.3-57.0), while the effective dose is characterized by a median of 8.8 (4.9-11.6) mSv. CT acquisition parameters, including anatomical coverage (69.0 (29.4-105.0) mm), tube potential (95.0 (80.0-100.0) kVp), tube current-time product (100.0 (100.0-150.0) mAs), and total acquisition time (51.0 (40.0-79.5) seconds), also exhibit considerable variability.

In contrast, the parameters related to contrast agent administration demonstrate a notable uniformity, with less variance around the median values of 50.0 (40.0-50.0) ml for contrast agent volume, 17.5 (15.2-18.5) g of iodine, and an injection rate of 5.0 (5.0-5.0) ml/s. Temporal sampling rates show medians of 1.5 (1.0-2.0) seconds and 2.0 (1.3-7.3) seconds for the lowest and highest values, respectively. The median slice thickness was recorded as 5.0 (3.0-5.8) mm.

Regarding the type of post-processing software, most of the research studies preferred to use vendor software as compared to third-party or in-house software. In addition, MSM emerges as the most frequently used perfusion model to quantify pancreatic perfusion parameters, followed by the deconvolution model.

3.1. Meta-analysis of pancreatic CT perfusion studies

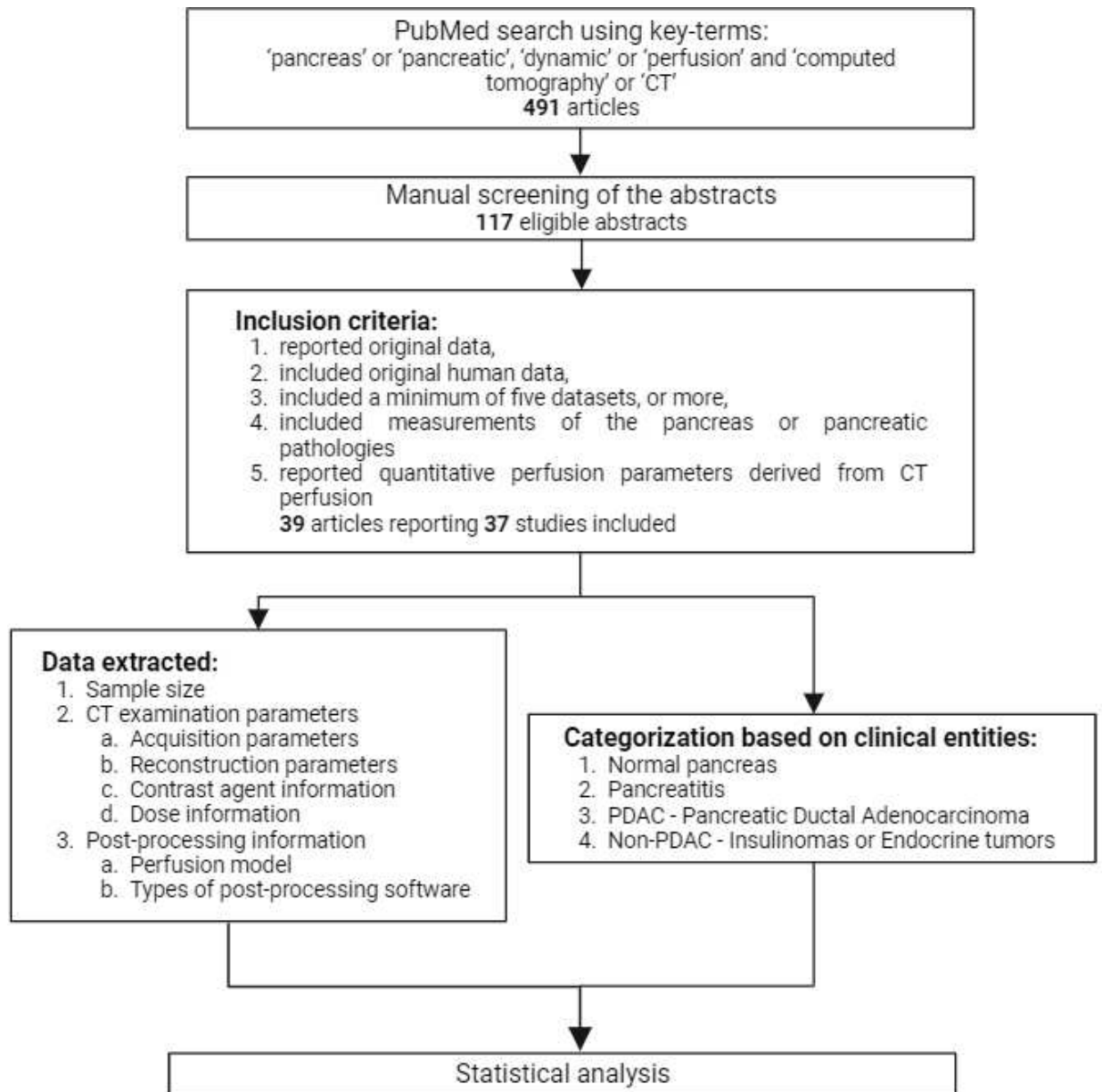


Figure 3.1: Flowchart illustrating the meta-analysis process

Results

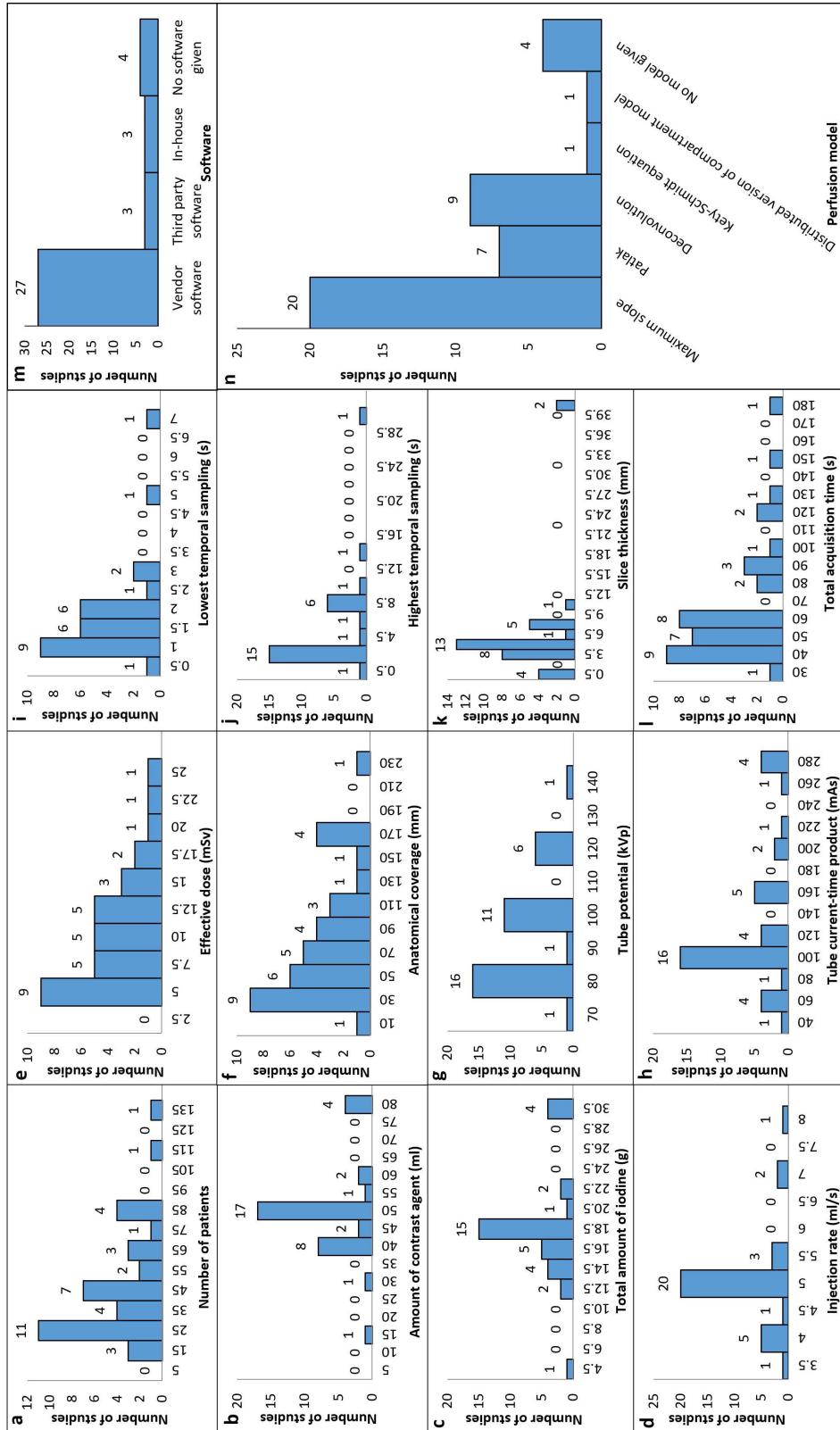


Figure 3.2: Histogram distribution of: (a) sample size (number of patients), (b–l) CT examination parameters, and (m) post-processing software and (n) perfusion model used to calculate the perfusion parameters by the selected studies, respectively. Please note that values higher than the highest histogram bin were put into the highest histogram bin. The total count of studies in the histogram (n) is greater than the total number of studies, as some of the reported studies have used more than one perfusion model for the analysis (i.e., maximum slope model (MSM) and Patlak analysis) (Skornitzke, Vats, Mayer, Kauczor & Stiller 2023)

3.1. Meta-analysis of pancreatic CT perfusion studies

Figure 3.3 presents linear regression graphs illustrating the mean values of the number of studies, sample size, and CT examination parameters in different years, offering a visual representation of the temporal changes in these parameters. Since 2010, both the number of studies and the patient population per study have exhibited a steady increase. Likewise, there is an upward trajectory in the amount of contrast agent used, which leads to an increase in iodine levels. Interestingly, no significant trend is observed in the injection rate.

Examining the tube potential, it is noted that there is a slight decrease in mean values, while the tube current-time product shows a gradual increase. On the contrary, the total acquisition time and effective dose do not show any pronounced trend over the years. However, the anatomical coverage exhibits a notable increasing trend. The slice thickness has decreased over time, reaching a mean minimum value of 2.5 mm.

In terms of temporal parameters, the lowest temporal sampling rate shows a significant decrease, indicating shorter intervals between individual acquisitions. On the other hand, the highest temporal sampling rate shows only a marginal decline. These observations collectively highlight the evolving landscape of CT examination practices and underscore the dynamic nature of key parameters over the years.

3.1.2 Comparison of pancreatic clinical entities based on quantitative measurements

The Mean \pm SD values for quantitative parameters, including BF, BV, and permeability, were calculated for various clinical entities and are presented in Table 3.2. Comparisons among different groups showed that the PDAC group exhibited the lowest averaged values for all parameters when compared to pancreatitis, normal pancreas, and non-PDAC groups. In particular, non-PDAC demonstrated the highest mean BF, while the normal pancreas exhibited the highest mean BV and permeability.

The findings were further illustrated through box-plot representations in Figure 3.4, depicting the distribution of quantitative parameters (BF, BV, and permeability) within different pancreatic pathologies. Additionally, Figure 3.5 displays W-ANOVA Tukey results showing significant differences in mean BF ($p < 0.001$) and BV ($p < 0.001$) between various pancreatic pathologies and normal pancreas. On the contrary, the permeability did not show a significant difference ($p = 0.11$).

Further analysis using Student's t-test following W-ANOVA indicated significant differences in BF and BV between normal pancreas/pancreatitis, normal pancreas/PDAC, and PDAC/non-PDAC groups ($p < 0.05$, respectively). Moreover, distinctions were observed in BF between pancreatitis/PDAC and pancreatitis/non-PDAC groups ($p < 0.05$). These comprehensive statistical insights underscore the

Results

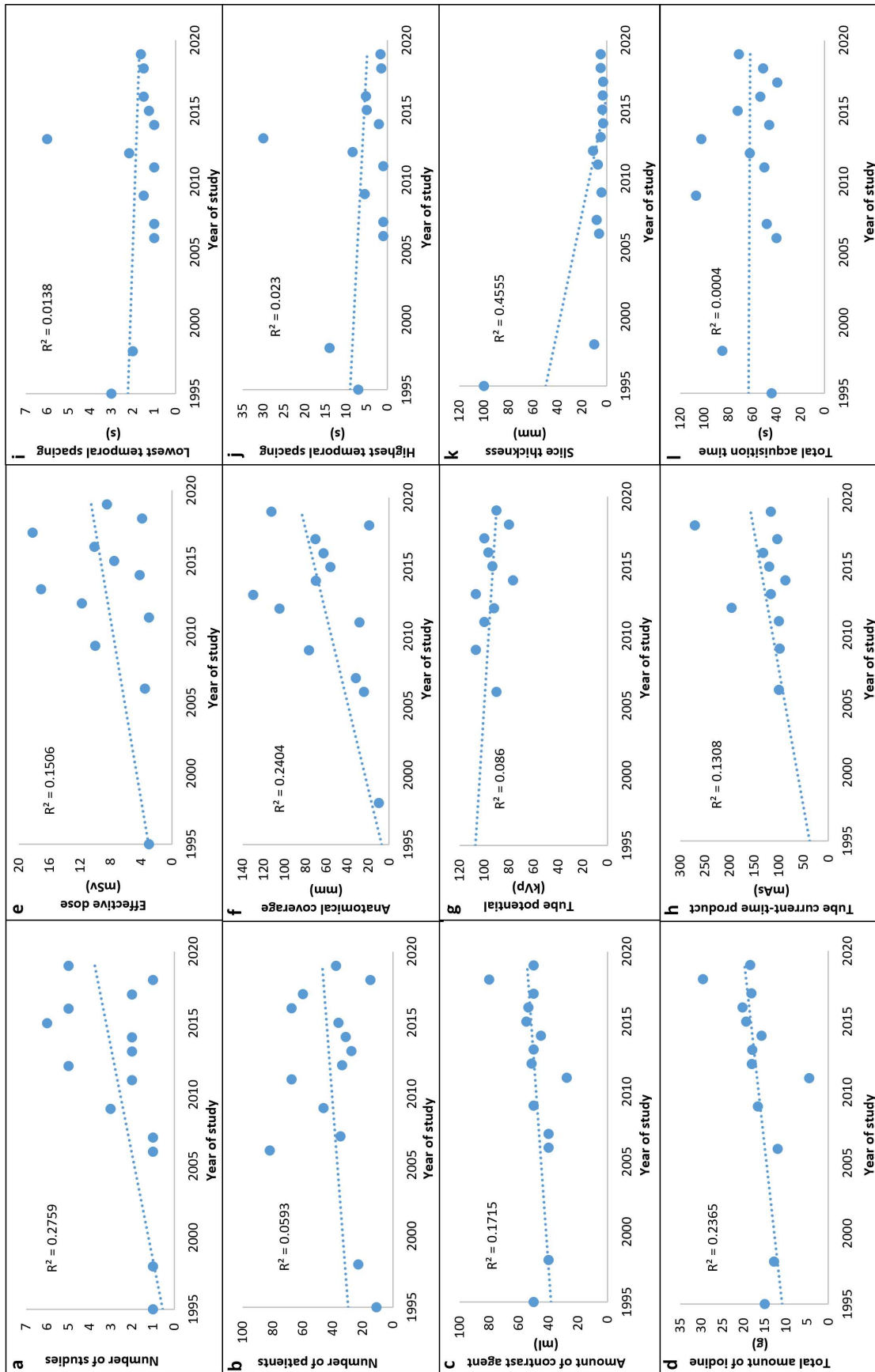


Figure 3.3: Linear regression plots of the means of (a) number of studies, (b) sample size (number of patients), and (c-l) all the CT examination parameters computed over the years (1995-2020). Please note that the plot for injection rate was omitted, as there was no observable trend of the mean injection rate (Skornitzke, Vats, Mayer, Kauczor & Stiller 2023)

different perfusion patterns among different pancreatic pathologies.

Clinical entities	Perfusion parameters		
	Blood flow (ml/100ml/min)	Blood volume (ml/100ml)	Permeability (ml/100ml/min)
Normal pancreas	100.9±30.9	20.0±6.0	36.9±13.4
Pancreatitis	64.0±22.4	13.1±5.0	33.7±15.6
PDAC	29.3±10.9	9.5±8.9	23.7±10.8
Non-PDAC	109.6±39.9	14.4±7.7	30.2±16.5

Table 3.2: Mean±SD of the quantitative parameters (blood flow, blood volume, and permeability) for the respective clinical entity. PDAC - Pancreatic ductal adenocarcinoma

Table 3.3 provides an overview of the statistically significant difference observed in studies comparing various pancreatic pathologies based on quantitative perfusion measurements. The table delineates the number of studies that reported statistically significant differences for each comparison, compared to the total number of studies reporting results of statistical analysis for each parameter and for each comparison. For example, in the comparison between normal pancreas and pancreatitis, a total of 8 studies have reported perfusion values. All 8 studies have found significant differences between normal pancreas and pancreatitis. Specifically, all 8 studies reported significant statistical results for BF, while 7 out of 8 studies also found significant results for BV. However, only 4 out of 8 studies reported measurements for permeability, and among these, only 2 studies demonstrated significant results. Similarly to the distribution of the total number of studies outlined in Table 3.1, the majority of the studies focused on PDAC, followed by pancreatitis. Conversely, findings for non-PDAC conditions are comparatively less. In particular, with two exceptions, all studies examining BF and BV demonstrated significant differences in their results. In contrast, only half of the studies investigating permeability reported statistically significant differences between the clinical entities analyzed.

3.1.3 Effects of CT examination parameters and perfusion model on the quantitative measurements

The comprehensive summary of the effects of CT examination parameters and perfusion model on the quantitative measurements are provided in Table 3.4. In particular, the amount of contrast agent administered, the injection rate, and the

Results

Studies reporting significant statistical results/Studies reporting perfusion values					
Compared clinical entities	Total studies combined	Blood flow	Blood volume	Permeability	
Normal pancreas versus Pancreatitis	8/8	8/8	7/8	2/4	
Normal pancreas versus PDAC	14/16	14/14	10/10	3/7	
Normal pancreas versus non-PDAC	3/3	2/3	2/3	0/2	
Pancreatitis versus PDAC	3/4	3/3	3/3	2/3	
Pancreatitis versus non-PDAC	0	0	0	0	
PDAC versus non-PDAC	0	0	0	0	

Table 3.3: Overview of the studies reporting significant statistical results for comparing the pancreatic pathologies based on perfusion measurements versus the studies (total studies: 19) reporting the perfusion parameters. PDAC - Pancreatic ductal adenocarcinoma

3.1. Meta-analysis of pancreatic CT perfusion studies

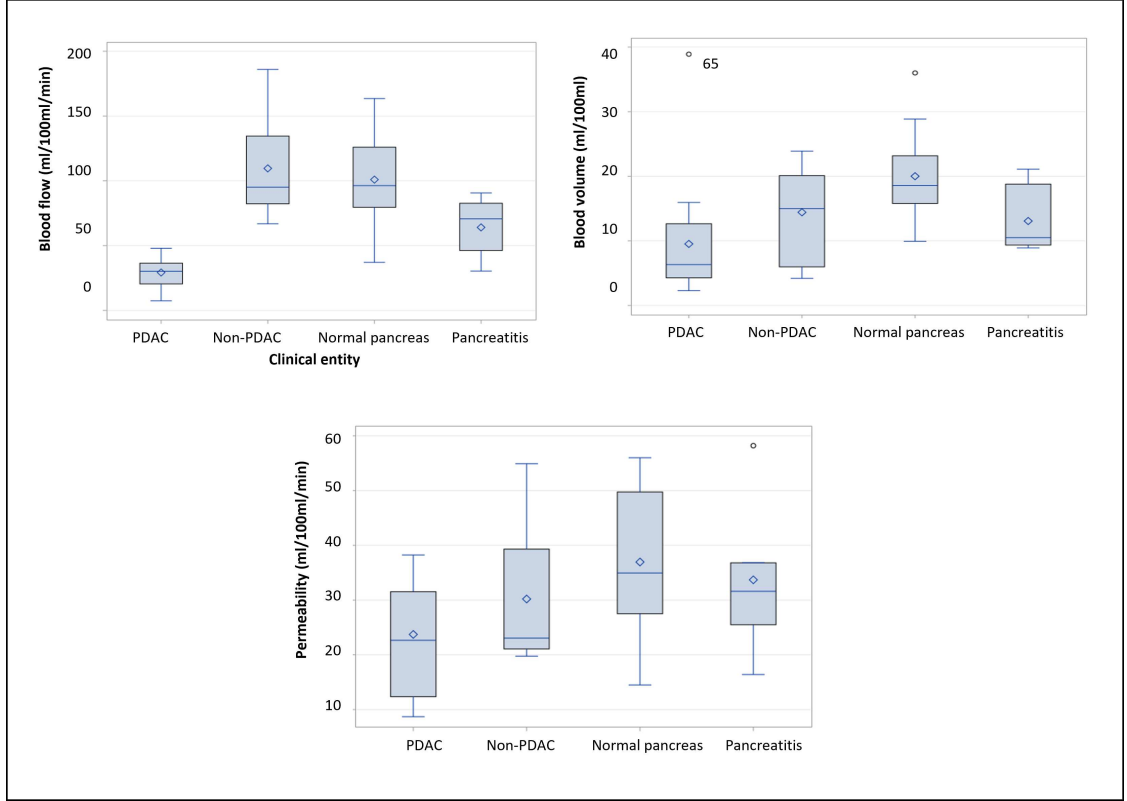


Figure 3.4: Boxplots for comparing the reported results of quantitative measurements of blood flow, blood volume, and permeability within the different pancreatic pathologies. PDAC - Pancreatic ductal adenocarcinoma (Skornitzke, Vats, Mayer, Kauczor & Stiller 2023)

incorporation of a saline flush demonstrate a significant influence on the reported BF. Additionally, the tube current-time product, the highest temporal sampling, and the use of variable temporal sampling have a significant effect on reported BV. Interestingly, none of the evaluated parameters demonstrate a statistically significant impact on reported permeability. This analysis underscores the intricate relationship between specific CT examination parameters, perfusion models, and their distinct effects on quantitative measurements of BF, BV, and permeability.

Figure 3.6 shows examples of box plots comparing the effect of CT examination parameters (which were reported as significant, refer to Table 3.4) on quantitative measurements such as BF and BV within different pancreatic pathologies. For example, the graphs reveal that in the absence of a saline flush, the normal pancreas exhibits higher BF values (mean BF 127.69 ± 37.21 ml/100ml/min) compared to when a saline flush is injected (mean BF 90.35 ± 20.97 ml/100ml/min). Similarly, variations in BV are observed with different temporal sampling rates, indicating higher values with variable sampling rates (mean BV 22.81 ± 5.68 ml/100ml) compared to constant sampling rates (mean BV 17.40 ± 4.37 ml/100ml). These findings underscore the influence of acquisition parameters on quantitative measurements in different pancreatic pathologies.

Results

Effects on quantitative measurements	Blood flow	Blood volume	Permeability
Amount of contrast agent	✓ (0.0422)	×(0.6681)	×(0.5636)
Amount of iodine	×(0.9605)	×(0.3591)	×(0.5063)
Total amount of iodine	×(0.0767)	×(0.7626)	×(0.5480)
Injection rate	✓ (0.0150)	×(0.4055)	×(0.3556)
Effective dose	×(0.7755)	×(0.1162)	×(0.3293)
Anatomical coverage	×(0.5885)	×(0.1600)	×(0.6122)
Tube potential	×(0.5329)	×(0.1386)	×(0.5088)
Tube current–time product	×(0.5742)	✓ (0.0152)	×(0.6112)
Lowest temporal sampling	×(0.2455)	×(0.1390)	×(0.9258)
Highest temporal sampling	×(0.0811)	✓ (0.0348)	×(0.6057)
Slice thickness	×(0.0960)	×(0.3996)	×(0.6851)
Total acquisition time	×(0.9281)	×(0.5947)	×(0.3858)
Use of variable temporal sampling	×(0.1041)	✓ (0.0078)	×(0.9196)
Use of saline flush	✓ (0.0067)	×(0.4341)	×(0.9693)
Perfusion model	×(0.1619)	×(0.2880)	×(0.3007)

Table 3.4: Effects of the CT examination parameters and evaluation technique on the quantitative measurements with the obtained p -values stated in parentheses. Bold values indicate a significant effect of the respective parameters on the quantitative measurements whereas non-bold values indicate a non-significant effect

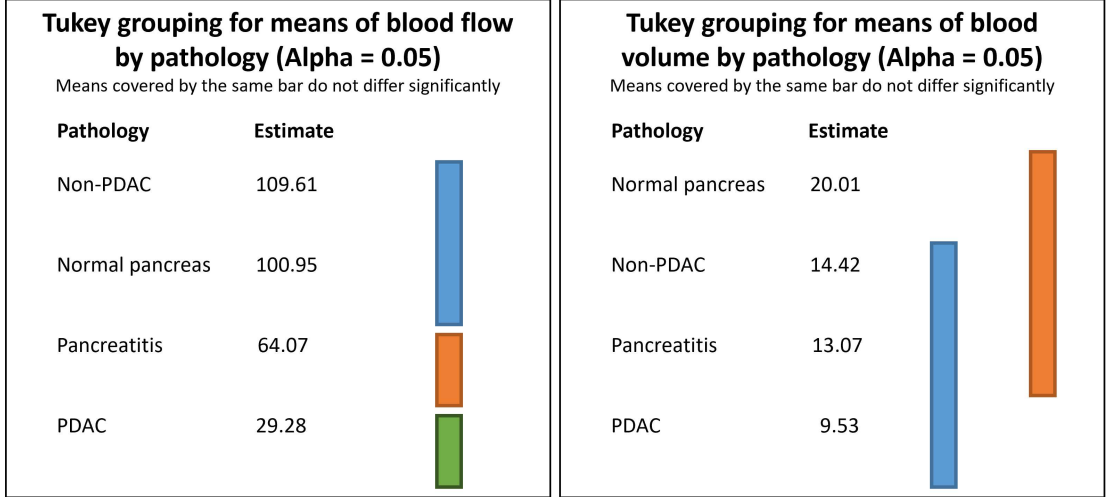


Figure 3.5: W-ANOVA Tukey grouping for comparing the weighted means of quantitative measurements (blood flow (ml/100 ml/min) and blood volume (ml/100 ml)) between the different pancreatic pathologies. Please note that no groupings are shown for permeability, as the W-ANOVA model was not significant for permeability ($p=0.11$). PDAC - Pancreatic ductal adenocarcinoma (Skornitzke, Vats, Mayer, Kauczor & Stiller 2023)

A statistically significant difference in total acquisition time emerged when comparing studies with single temporal sampling rates to those with variable temporal sampling rates ($p=0.03$). Longer acquisition times were found for studies with variable temporal sampling rates. Despite this variance, the contrast in effective dose between studies with single temporal sampling rates and those with variable temporal sampling rates did not show statistical significance ($p=0.19$).

3.2 Noise-correction algorithm analysis

3.2.1 Digital perfusion phantom

The mean \pm SD values of GTBF, noise-impacted BF, and corrected BF obtained by applying a noise correction algorithm in digital perfusion phantoms are mentioned in Table 3.5. The measured noise-impacted BF and noise-corrected BF measurements for the whole pancreatic region were 140.3 ± 111.7 ml/100ml/min and 131.9 ± 125.9 ml/100ml/min, respectively, whereas GTBF was 131.3 ± 127.7 ml/100ml/min. Similarly, GTBF, measured noise-impacted BF and noise-corrected BF measurements for the parenchyma tissue region were 225 ± 120.9 ml/100ml/min, 218.4 ± 112.4 ml/100ml/min, and 224.1 ± 119.2 ml/100ml/min, respectively, and the GTBF, measured noise-impacted BF and noise-corrected BF measurements for the carcinoma tissue region were 37.5 ± 20.2 ml/100ml/min, 62.1 ± 11.5 ml/100ml/min, and 39.7 ± 21.9 ml/100ml/min, respectively. An example of ground truth, noise-impacted, and noise-corrected BF perfusion maps of a digital perfusion phantom

Results

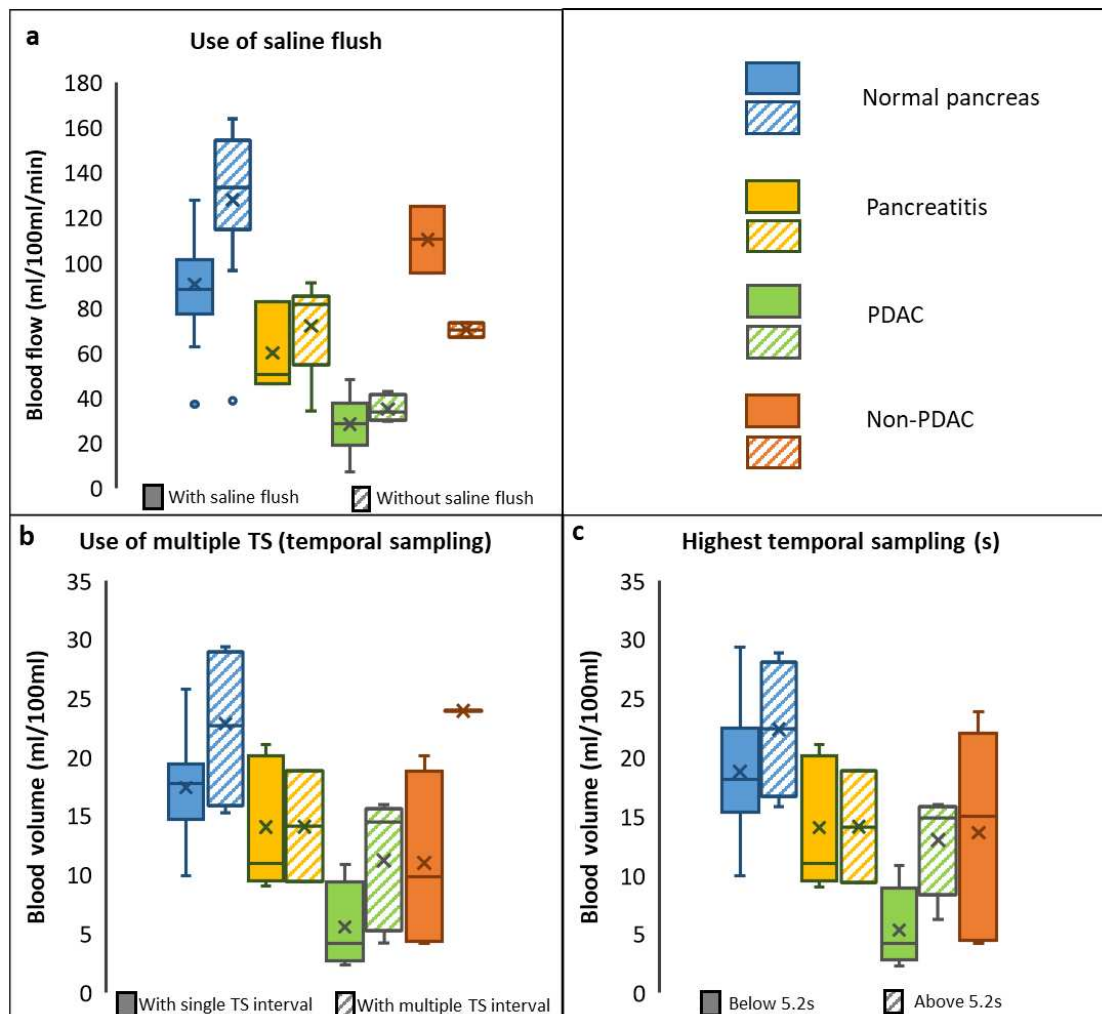


Figure 3.6: Boxplots comparing the effect of acquisition parameters on the quantitative measurements (blood flow and blood volume) within different pancreatic pathologies: (a,b) show the binary effect of saline flush and temporal sampling on the blood flow and blood volume, respectively; (c) shows the effect of highest temporal sampling on blood volume. Please note the differences in sample sizes between the groups (cf. Table 3.1). PDAC- Pancreatic ductal adenocarcinoma (Skornitzke, Vats, Mayer, Kauczor & Stiller 2023)

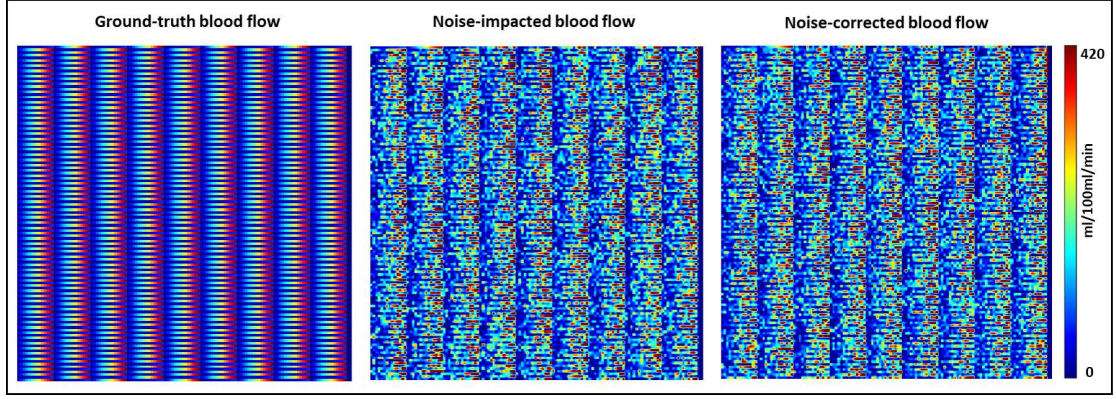


Figure 3.7: An example of ground truth, noise-impacted and noise-corrected blood flow perfusion maps of a digital perfusion phantom

is shown in Figure 3.7, which exemplifies the contrast in $\text{mean} \pm \text{SD}$ values.

After noise correction, the average absolute difference between the calculated BF measurements with each iteration and the ground truth decreased significantly from 18.77 to 3.56 ml/100 ml/min, as mentioned in Table 3.6. Additionally, the model error decreased from 12.63 to 11.03 ml/100 ml/min, while the random error decreased from 4.02 to 3.96 ml/100 ml/min, as detailed in Table 3.6. For a visual representation, refer to Figure 3.8, which illustrates the absolute difference, model error, and random error curves for each iteration.

	BFD	BFD	BFD	BFD	BFD	BFD	BFD	BFD
		corr(1)	corr(2)	corr(3)	corr(4)	corr(5)	corr(6)	corr(7)
Absolute difference	18.77	7.28	5.25	4.63	4.17	3.27	3.27	3.56
Model error	12.63	12.54	9.53	10.97	10.78	9.18	9.31	11.03
Random error	4.02	4.64	4.09	3.54	3.71	4.14	4.65	3.96

Table 3.6: The absolute difference between the calculated blood flow (BF) measurements and the ground truth; the model error, and the random error for each iteration and noise-impacted BF measurements. BFD represents the noise-impacted BF measurements and BFDcorr(1)-BFDcorr(7) represents the BF values through the noise correction algorithm with respective iterations

The student's t-test p-value showed a significant difference between carcinoma

Mean±SD (Ground truth BF) (ml/100ml/min)		GTBF (Noise-impacted BF)	BFD corr(1)	BFD corr(2)	BFD corr(3)	BFD corr(4)	BFD corr(5)	BFD corr(6)	BFD corr(7)
Pancreas	131.3	140.3	137.0	134.6	133.4	131.4	132.0	132.0	131.9
	±127.7	±111.7	±122.3	±125.2	±125.6	±124.7	±127.7	±126.9	±125.9
Parenchyma	225	218.4	225.8	225.8	225.8	223.3	225.7	225.2	224.1
	±120.9	±112.4	±117.6	±119.7	±118.4	±117.1	±120.6	±120.1	±119.2
Carcinoma	37.5	62.1	48.1	43.4	40.9	39.5	38.3	38.9	39.7
	±20.2	±11.5	±16.8	±19.2	±20.9	±22.7	±22.5	±21.2	±21.9
T-test (p-value)	<0.0001	<0.0001	<0.0001	<0.0001	<0.0001	<0.0001	<0.0001	<0.0001	<0.0001
CNR	2.66	2.52	2.64	2.63	2.65	2.63	2.62	2.64	2.61

Table 3.5: Mean±SD blood flow (BF) values of the whole pancreatic region, pancreatic parenchyma, and carcinoma tissue using digital perfusion phantoms. GTBF and BFD represent the ground truth measurements and the noise-impacted BF measurements, respectively. BFDcorr(1)-BFDcorr(7) represents the BF values through the noise correction algorithm with respective iterations. The student's t-test p-value shows a significant difference between carcinoma and the parenchyma tissue based on calculated BF values. Contrast to noise ratio (CNR) shows an improvement from 2.52 to 2.61 between noise-impacted and noise-corrected BF maps

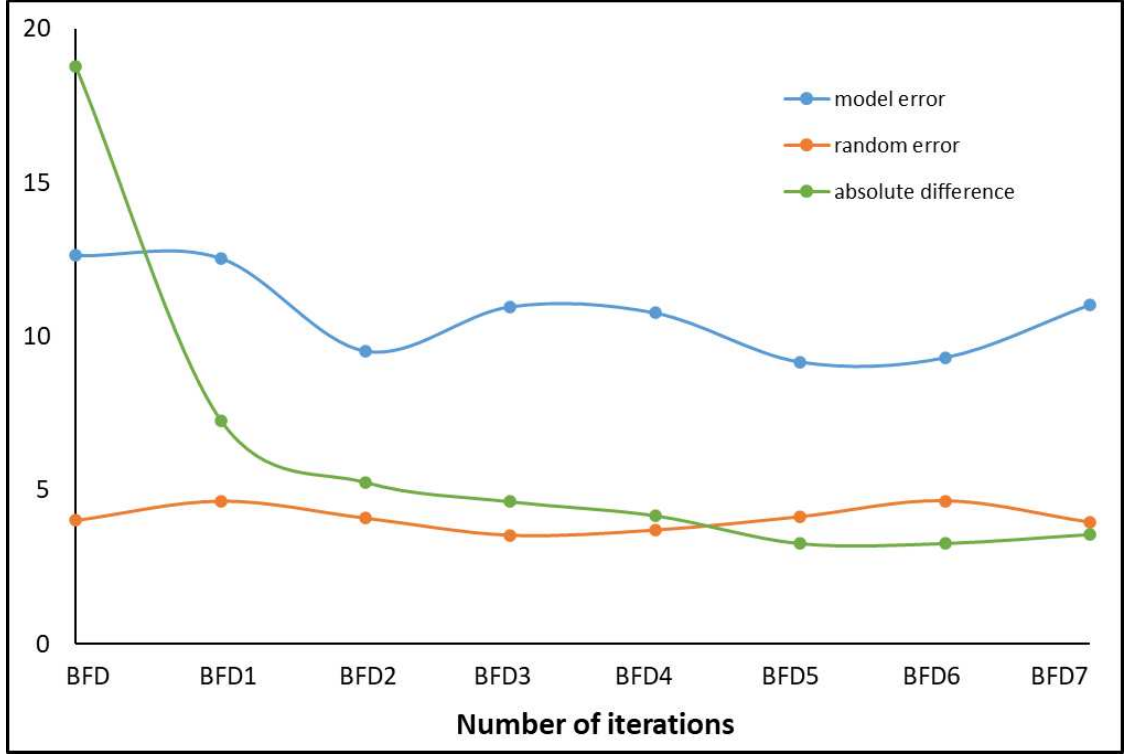


Figure 3.8: The absolute difference, model error, and random error curves through the noise correction algorithm with respective iterations

and the parenchyma tissue based on calculated noise-impacted and noise-corrected BF values. After noise correction, the CNR improved from 2.52 to 2.61 between noise-impacted and noise-corrected BF maps (refer to Figure 3.7).

Figure 3.9 illustrates the Bland-Altman analysis for the digital perfusion phantom. Subfigure (a) specifically highlight the analysis between ground truth (GTBF) and noise-corrected BF (BFDcorr) measurements and subfigure (b) show the analysis between noise-impacted BF (BFD) and the noise-corrected BF (BFDcorr) measurements. The Bland-Altman limits of agreement for each measurement are shown in the Figure 2.8. The limits of agreement were -9.63 to 8.42 ml/100ml/min between GTBF and BFDcorr and -27.18 to 44.01 ml/100ml/min between BFD and BFDcorr.

3.2.2 Validation on clinical dataset

The mean \pm SD GTBF, noise-impacted BF, and the corrected BF values using the noise correction algorithm applied to the clinical data set are mentioned in Table 3.7. The measured noise-impacted BF and noise-corrected BF measurements for the whole pancreatic region were 97.1 ± 64.2 ml/100ml/min and 84.1 ± 96.9 ml/100ml/min, respectively. Similarly, the measured noise-impacted BF and noise-corrected BF measurements for the parenchyma tissue region were 148.3 ± 50.8 ml/100ml/min, and 155.0 ± 91.5 ml/100ml/min, respectively, and the measured

Results

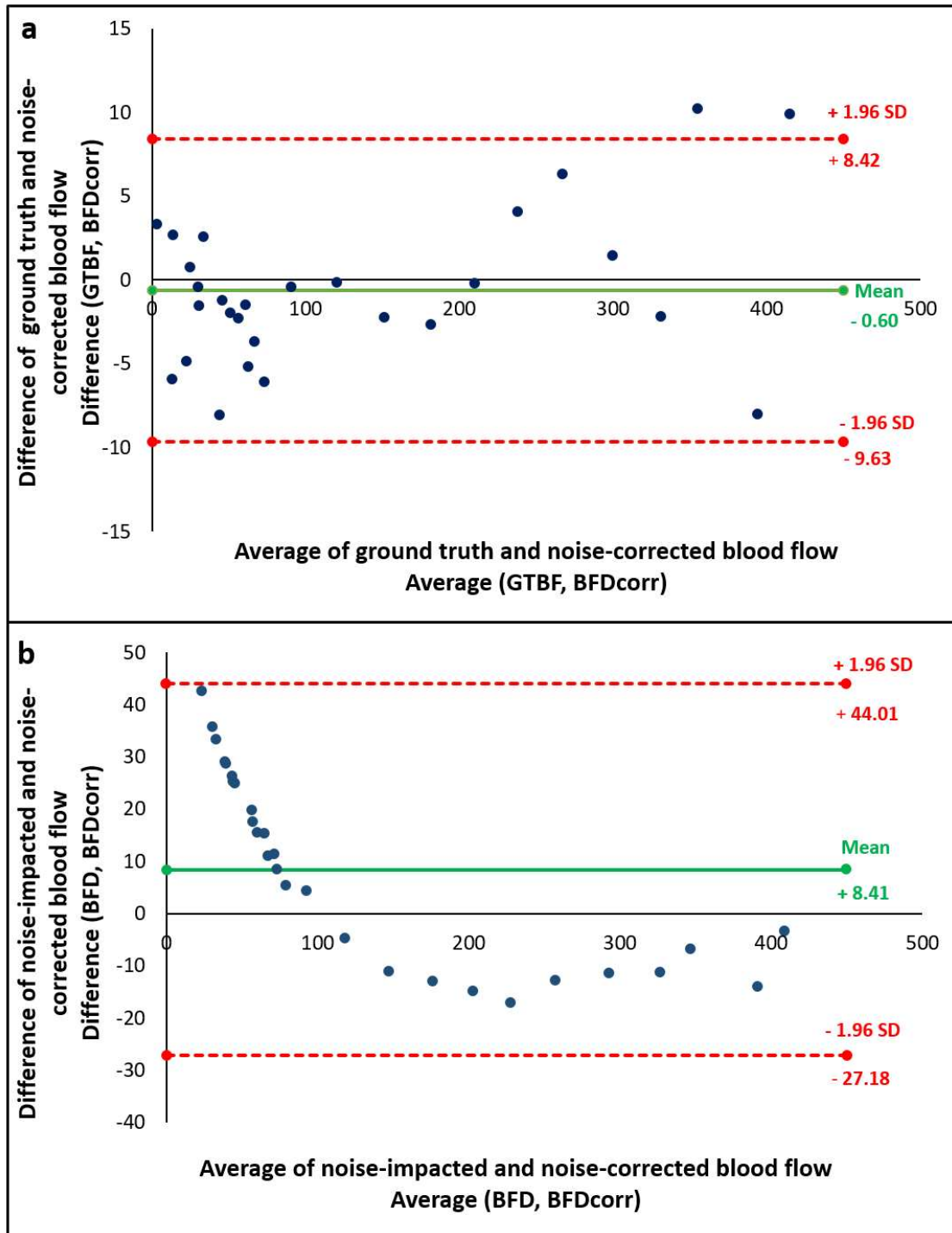


Figure 3.9: Bland-Altman plots for digital perfusion phantom including the limits of agreement, showcasing a comparison between (a) groundtruth (GTBF) and noise-corrected blood flow (BFDcorr) measurements and (b) noise-impacted (BFD) and noise-corrected blood flow (BFDcorr) measurements

noise-impacted BF and noise-corrected BF measurements for the carcinoma tissue region were 45.8 ± 20.3 ml/100ml/min, and 13.3 ± 18.7 ml/100ml/min, respectively.

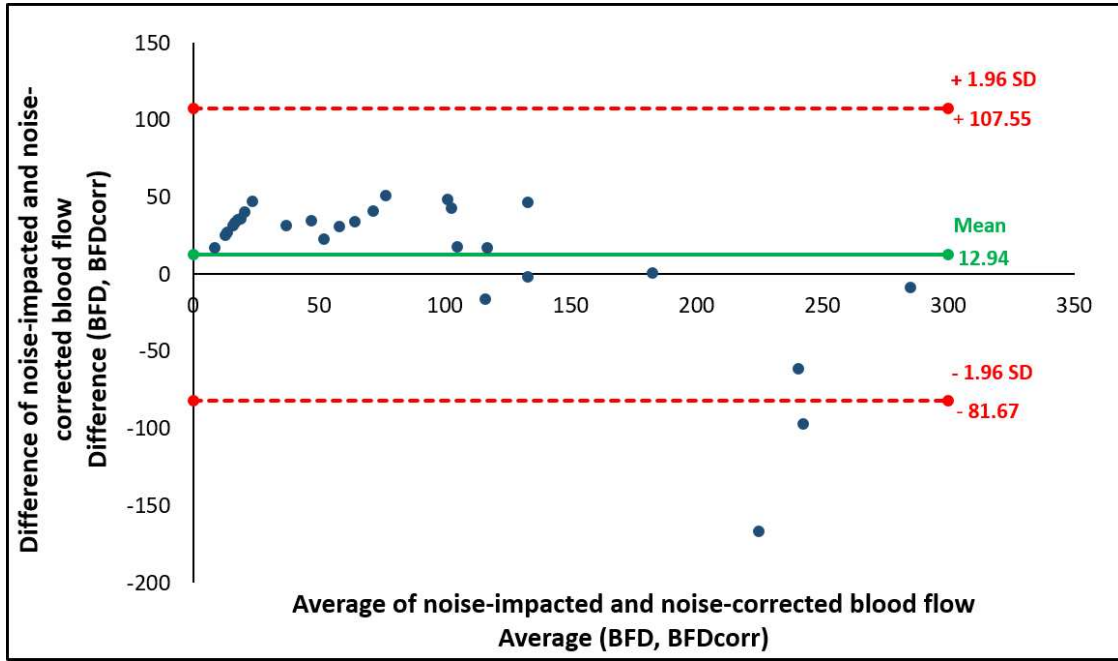


Figure 3.10: Bland-Altman plot including the limits of agreement, showcasing a comparison between the noise-impacted (BFD) and noise-corrected blood flow (BFDcorr) measurements in the clinical dataset

The student's t-test p-value ($p < 0.0001$) shows a significant difference between carcinoma and the parenchyma tissue based on calculated noise-impacted and noise-corrected BF values. In particular, after implementing noise correction, there was a notable change in CNR from 2.88 to 2.57 when comparing the noise-impacted and noise-corrected BF maps.

Figure 3.10 illustrates the Bland-Altman analysis, showcasing a comparison between the noise-impacted (BFD) and noise-corrected BF (BFDcorr) measurements in the clinical dataset. The Bland-Altman limit of agreement for each measurement of a clinical data set are mentioned in Figure 3.10. The limits of agreement were -81.67 to 107.55 ml/100ml/min for the clinical dataset.

For the visual representation, an example of noise-impacted and noise-corrected BF perfusion maps from a pancreatic adenocarcinoma patient is shown in Figure 3.7, which exemplifies the contrast in $\text{mean} \pm \text{SD}$ values.

3.3 First pass analysis

3.3.1 FPA1

An example of BF maps obtained using FPA1 is shown in Figure 3.12, exemplifying the contrast in $\text{mean} \pm \text{SD}$ values. The $\text{mean} \pm \text{SD}$ BF values for FPA1 were 30.3 ± 19.2 ml/100ml/min in the case of carcinoma (within the circular ROI2), while

	BFD (Noise- impacted BF)	BFD corr(1)	BFD corr(2)	BFD corr(3)	BFD corr(4)	BFD corr(5)	BFD corr(6)	BFD corr(7)
Mean\pmSD (ml/100ml/min)								
Pancreas	97.1	86.9	83.5	84.3	84.5	82.5	83.6	84.1
	± 64.2	± 79.5	± 85.1	± 89.0	± 91.5	± 92.2	± 94.2	± 96.9
Parenchyma	148.3	147.2	147.0	149.9	152.5	151.0 \pm 85.1	153.4	155.0
	± 50.8	± 67.9	± 75.9	± 81.1	± 83.4		± 87.5	± 91.5
Carcinoma	45.8	26.6	20.0	18.7	16.4	14.0	13.8	13.3
	± 20.3	± 27.7	± 25.8	± 25.7	± 22.8	± 19.2	± 18.8	± 18.7
T-test(p-value)	<0.0001	<0.0001	<0.0001	<0.0001	<0.0001	<0.0001	<0.0001	<0.0001
CNR	2.88	2.52	2.50	2.46	2.56	2.63	2.63	2.57

Table 3.7: Mean \pm SD blood flow (BF) values of pancreatic region, pancreatic parenchyma, and carcinoma tissue in clinical dataset. BFD represents the noise-impacted BF measurements and BFDcorr(1)-BFDcorr(7) represents the BF values through the noise correction algorithm with respective iterations. Student's t-test p-value shows a significant difference between carcinoma and parenchyma tissue based on calculated BF values. The contrast-to-noise ratio (CNR) does not show any improvement, but lies in a reasonable range

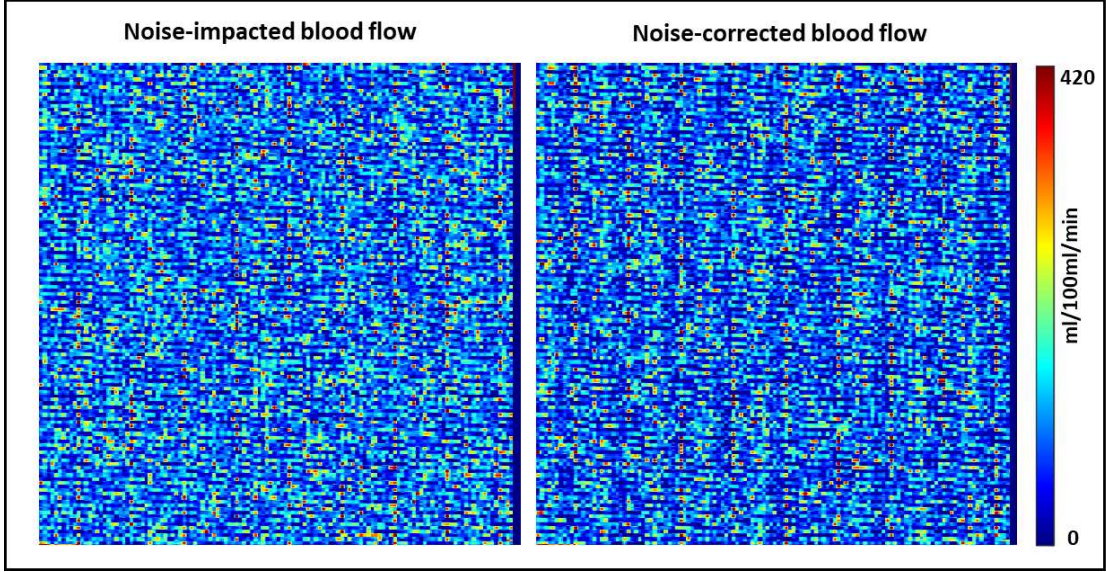


Figure 3.11: An example of noise-impacted and noise-corrected blood flow perfusion maps for pancreatic adenocarcinoma patient dataset

the parenchyma exhibited a higher perfusion rate of 89.0 ± 31.7 ml/100ml/min (within the circular ROI3) as mentioned in Table 3.8. Similarly, in the case of carcinoma (polygonal ROI4) and parenchyma (polygonal ROI5), FPA1 registered mean \pm SD values of 42.3 ± 16.4 ml/100ml/min and 74.6 ± 29.6 ml/100ml/min, respectively as mentioned in Table 3.9.

3.3.2 FPA2

Figure 3.12 illustrates BF maps obtained using FPA2. The mean \pm SD BF values calculated for carcinoma tissue region (enclosed within the circular ROI2) ranged from 27.3 ± 18.8 ml/100ml/min to 39.5 ± 26.6 ml/100ml/min and for parenchyma region (enclosed within the circular ROI3) ranged from 85.6 ± 37.5 ml/100ml/min to 117.7 ± 44.5 ml/100ml/min at ten-time points for FPA2, as detailed in Table 3.8. Furthermore, Table 3.9 provides the mean \pm SD BF values for the entire carcinoma tissue (within polygonal ROI4) and the entire parenchyma tissue (within polygonal ROI5) over the same ten time-points for FPA2.

3.3.3 Validation using Maximum slope model

The mean \pm SD of MSM BF values obtained from circular ROIs were 42.0 ± 24.8 ml/100 ml/min for carcinoma (ROI2) and 106.8 ± 41.5 ml/100 ml/min for parenchyma (ROI3), respectively (see Table 3.8). Additionally, BF values derived from polygonal ROIs exhibited mean \pm SD values of 53.7 ± 23.9 for carcinoma (ROI4) and 91.2 ± 37.1 for parenchyma (ROI5) (refer to Table 3.9). BF values were observed to be slightly lower for FPA compared to MSM. These results provide notable distinctions between carcinoma and parenchyma BF measurements in circular and polygonal ROIs. Figure 3.12 shows the BF maps generated using MSM.

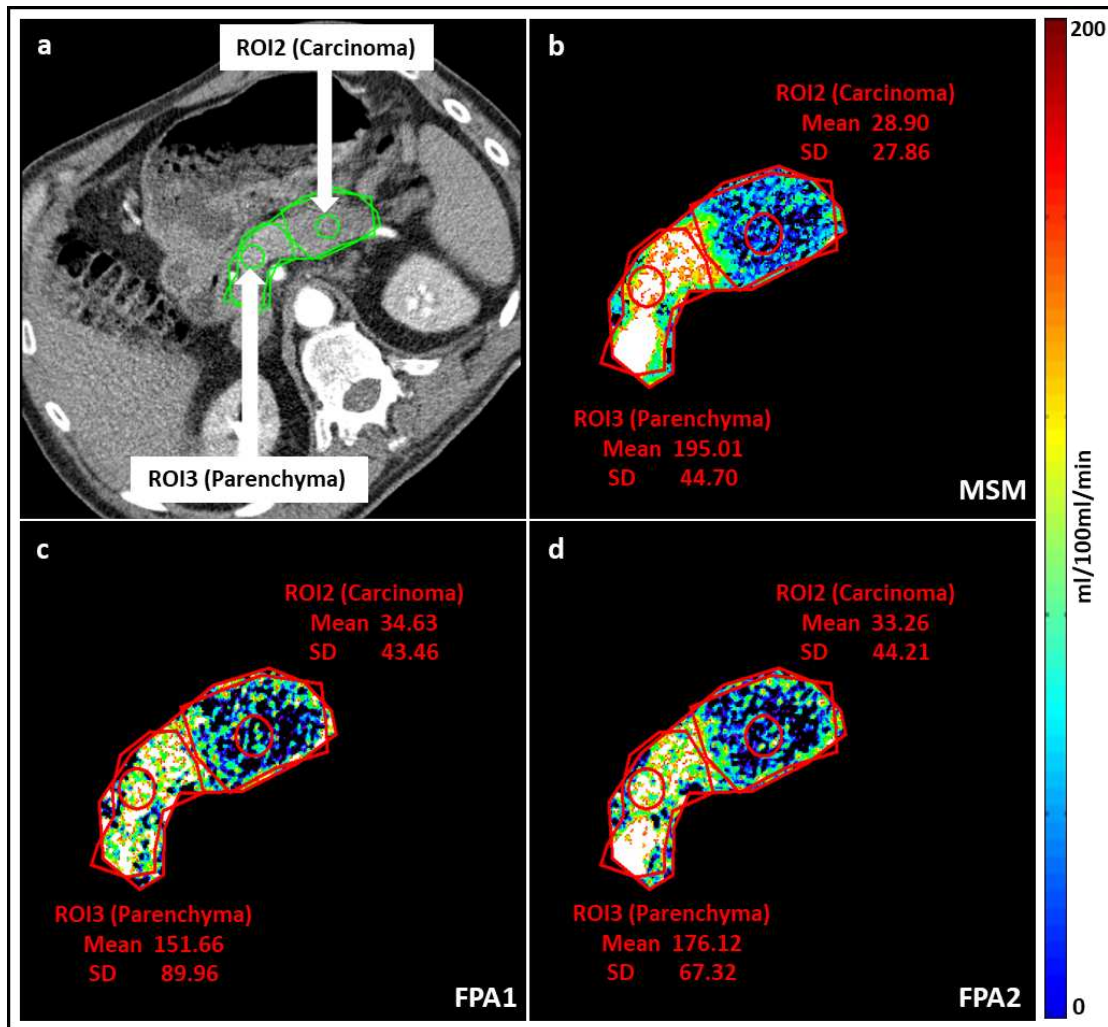


Figure 3.12: First pass analysis (FPA) and maximum slope model (MSM) perfusion maps. The conventional dynamic CT image (a), MSM perfusion map (b), FPA1 perfusion map at tmax (c), and FPA2 perfusion map at t9 (d) are shown for a pancreatic adenocarcinoma patient. The blood flow (BF) perfusion maps show mean and SD values for circular ROI2 (carcinoma) and ROI3 (parenchyma). Note the higher mean BF of parenchyma tissue as compared to carcinoma for FPA1, FPA2, and MSM. Mean values are comparable between FPA1, FPA2, and MSM for the corresponding tissue regions

BF measurements obtained using FPA2 were found to be comparable to those obtained with FPA1. Box plot analysis, illustrating BF values through circular ROIs at various acquisition times for both carcinoma and parenchyma tissue, is shown in Figure 3.13. Notably, the box plot reveals that the acquisition range from t4 to t9 demonstrates a narrowed spread in BF values compared to other time points. Moreover, parenchyma tissue exhibits an overall reduction in the spread of BF values compared to carcinoma. Despite variations in acquisition tim-

Tissue	FPA1			FPA2										MSM		
type	tmax	t1	t2	t3	t4	t5	t6	t7	t8	t9	t10					
			Circular ROI blood flow (ml/100ml/min) measurement													
Carcinoma	30.3	36.7	34.4	32.8	29.9	29.8	31.9	27.3	32.2	37.9	39.5			42.0		
	±19.2	±20.8	±17.6	±15.6	±17.3	±16.1	±20.0	±18.8	±21.0	±23.0	±26.6			±24.8		
Parenchyma	89.0	105.4	102.7	99.6	92.1	91.4	85.6	89.	98.2	102.0	117.7			106.8		
	±31.7	±56.7	±56.1	±45.5	±32.1	±40.2	±37.5	±31.3	±36.8	±41.5	±44.5			±41.5		
T-test (p value)	<0.0001	0.0001	<0.0001	<0.0001	<0.0001	<0.0001	<0.0001	<0.0001	<0.0001	<0.0001	<0.0001			<0.0001		
Pearson's correlation (r)	0.95	0.82	0.86	0.87	0.93*	0.94*	0.91*	0.93*	0.93*	0.92*	0.90					

Table 3.8: Mean±SD blood flow (BF) values of carcinoma (ROI2) and parenchyma (ROI3) tissue for **circular ROI** using FPA1, FPA2 at all ten acquisition times and MSM. Circular ROIs were used to indicate the respective tissues with a high degree of confidence. The p-value of Student's t-test shows a significant difference between carcinoma and parenchyma tissue. The correlation values marked with an asterisk show the acquisition time range (t4 to t9) with the highest correlation (r > 0.90) between FPA2 and MSM

Tissue	FPA1	FPA2								MSM		
type	tmax	t1	t2	t3	t4	t5	t6	t7	t8	t9	t10	
Carcinoma	Polygonal ROI blood flow (ml/100ml/min) measurement											
	42.3	49.5	44.2	46.9	44.2	39.6	42.5	41.9	44.7	51.4	54.1	53.7
	±16.4	±18.0	±15.7	±18.3	±18.7	±14.7	±16.3	±16.9	±17.8	±19.4	±22.5	±23.9
Parenchyma	74.6	82.6	84.9	80.5	78.5	76.0	73.7	76.1	80.5	87.8	7.9	91.2
	±29.6	±34.7	±34.8	±32.3	±31.4	±32.7	±30.8	±28.8	±32.5	±34.9	±38.9	±37.1
T-test (p value)	<0.0001	<0.0001	<0.0001	<0.0001	<0.0001	<0.0001	<0.0001	<0.0001	<0.0001	<0.0001	<0.0001	<0.0001
Pearson's correlation (r)	0.66	0.38	0.55	0.57	0.56	0.66	0.72*	0.75*	0.73*	0.72*	0.67	

Table 3.9: Mean±SD blood flow (BF) values of carcinoma (ROI4) and parenchyma (ROI5) tissue for **polygonal ROI** using FPA1, FPA2 at all ten acquisition times and MSM. Polygonal ROIs were used to circumscribe respective tissues for voxel-by-voxel analysis. Student's t-test p-value for voxel values in polygonal ROIs shows a significant difference between carcinoma and parenchyma at all ten acquisition times. The correlation values marked with an asterisk show the acquisition time range (t6-t9) with the highest correlation (r > 0.7) between FPA2 and MSM for each voxel value in the polygonal ROI

ing, the COV which measures the relative variability of a set of data points, plays a crucial role in assessing the consistency of BF values. A low COV indicates that the BF values exhibit less variability and sensitivity across different time points. For instance, the COV for carcinoma and parenchyma were found to be 11.6% and 9.5%, respectively, suggesting relatively consistent BF measurements. Moreover, the use of polygonal ROI further reduces the COV between time points to 9.9% for carcinoma and 8.7% for parenchyma. This highlights the robustness of the BF measurements between different acquisition times and tissue types.

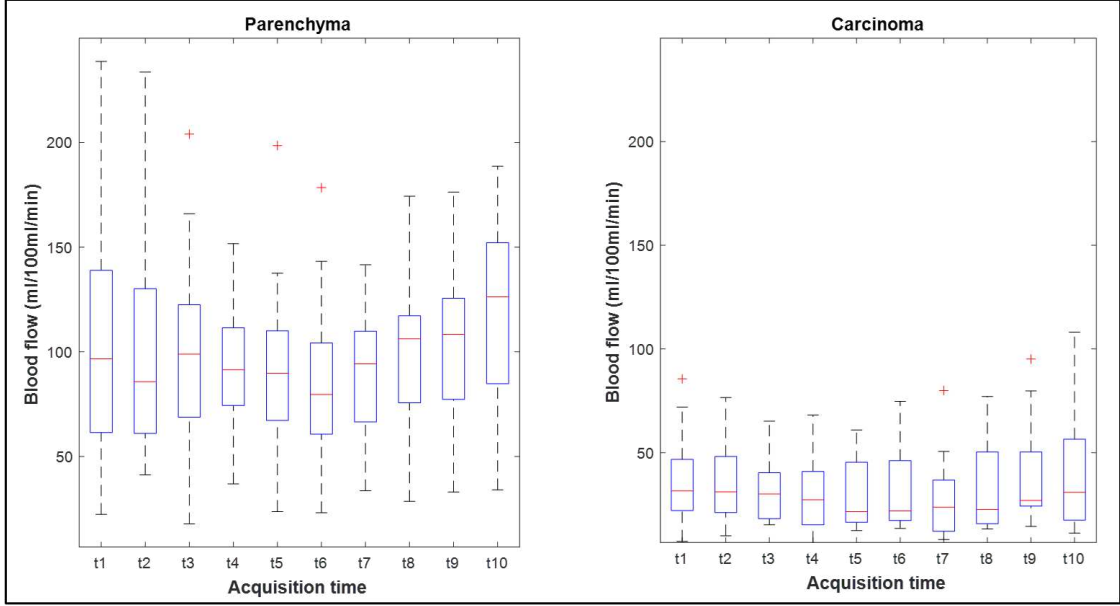


Figure 3.13: Box plot analysis at different acquisition timings. Box plots for FPA2 blood flow (BF) measurements at the investigated acquisition times for both carcinoma (circular ROI2) and parenchyma (circular ROI3) tissue

Correlation analysis between mean values of BF measurements within a high degree of confidence region, that is, circular ROIs (ROI2 and ROI3), revealed a significant association between FPA1 and MSM, with a correlation coefficient of 0.95. Similarly, the correlation between FPA2 and MSM ranged from 0.82 to 0.94, depending on the acquisition time. In particular, the highest correlations for FPA2 and MSM occurred during acquisitions from t4 to t9 (ranging from 0.91 to 0.94), as illustrated in Table 3.8.

Additionally, an analysis of BF measurements at the voxel level within polygonal ROIs (ROI4 and ROI5) demonstrated strong correlations between FPA1 and MSM ($r = 0.66$) and between FPA2 and MSM ($r = 0.38$ – 0.75). Peak correlations for FPA2 and MSM were observed during acquisitions between t6 and t9 (ranging from 0.72 to 0.75), as detailed in Table 3.9. For a visual representation, refer to Figure 3.14, which illustrates the correlation curves between FPA2 and MSM for both mean values and individual voxels, highlighting the optimal time range for

Results

FPA2.

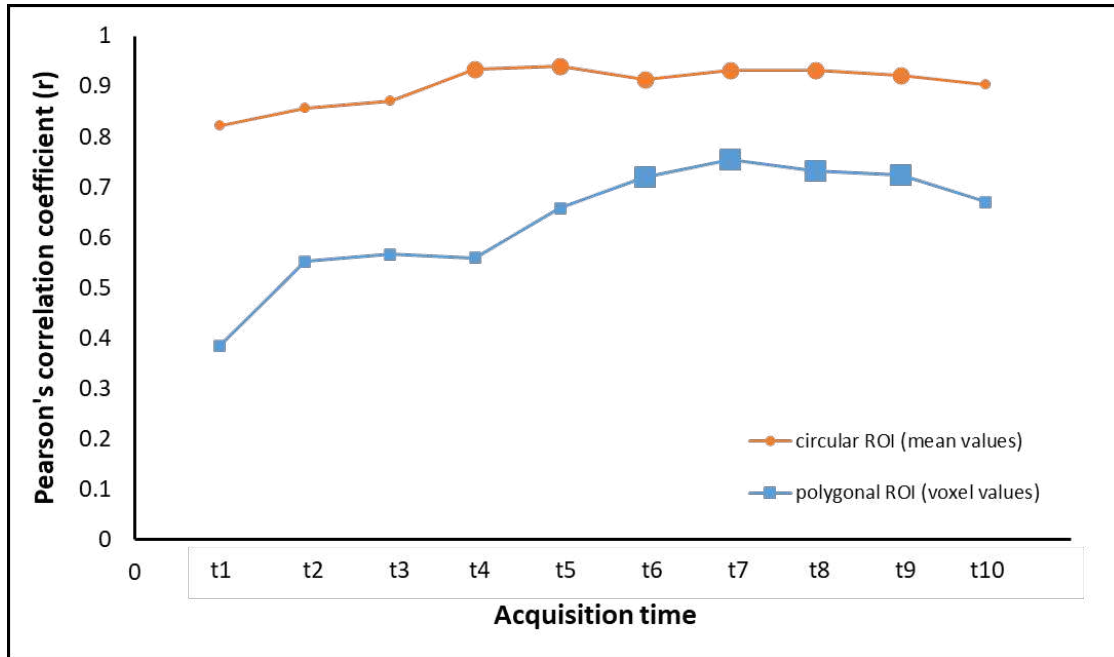


Figure 3.14: Correlation curves between FPA2 and MSM. Pearson's correlation curves between FPA2 and MSM at the investigated acquisition times (t1–t10) for carcinoma and parenchyma tissue combined. Acquisitions with a high correlation are highlighted by bold markers.

Significant distinctions in mean values within circular ROIs were observed in both parenchyma and carcinoma (ROI2 and ROI3) for FPA1, FPA2, and MSM, with p values indicating statistical significance ($p < 0.0001$). Furthermore, notable variations in voxel values within polygonal ROIs (ROI4 and ROI5) were found to be statistically significant for FPA1, FPA2, and MSM ($p < 0.0001$). These findings show discernible differences between tissue types using FPA methods.

In the context of FPA acquisition using only two volume scans, the effective radiation dose of the patient was found to be 0.27 ± 0.14 mSv, with a total acquisition time of 27.02 seconds. On the contrary, a conventional CT perfusion acquisition at a tube voltage of 80 kVp exhibited significantly higher values, with a radiation dose of 4.64 ± 2.32 mSv and an acquisition time of 49.68 seconds. Figure 3.15 shows a comparison of effective radiation dose and scan time between MSM and FPA. This underscores the potential benefits of employing FPA as a more efficient and patient-friendly CT perfusion technique.

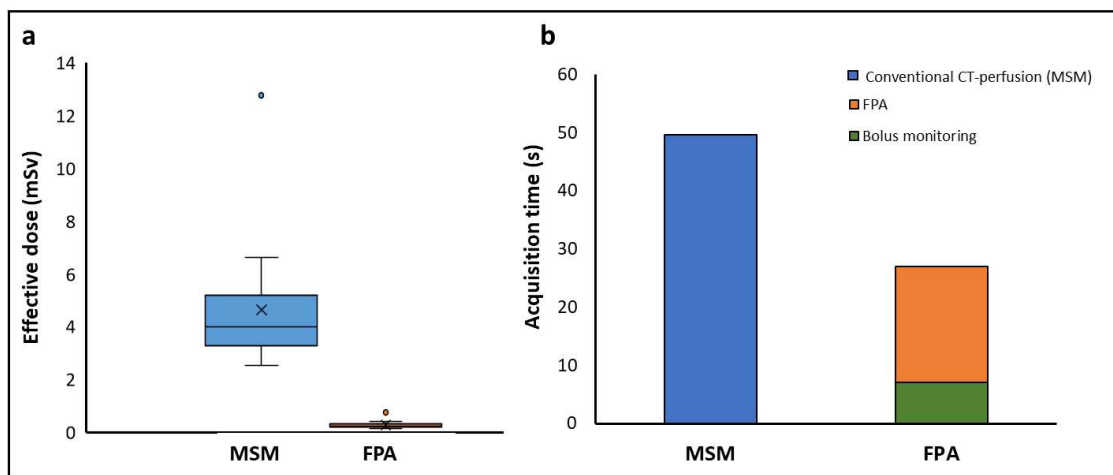


Figure 3.15: Comparison of effective dose and scan time between MSM and FPA. Box plot (a) and a bar graph (b) show the patient radiation exposure, indicated by effective dose (mSv), and total acquisition time (s) of MSM and FPA, respectively

The more we know, the more mystery there is.
Albert Einstein

4

Discussion

Numerous research studies have shown that the quantitative results of CT perfusion measurements vary according to CT examination parameters and evaluation procedures. The factors influencing this variability include the temporal sampling rate as observed in the studies (Wintermark et al. 2004, Klotz et al. 2015, Skornitzke et al. 2019, Schneeweiß et al. 2016). The presence of such variability poses a challenge to the direct comparison of quantitative measurements in various studies and hinders their applicability in clinical practice. Therefore, the need for standardization of acquisition protocols and evaluation procedures is emerging to achieve reliable and clinically meaningful CT perfusion measurements.

In addition to issues related to acquisition parameters, some studies have mentioned the negative impact of image noise on the precision of CT perfusion measurements, as highlighted by (Skornitzke et al. 2019, Juluru et al. 2013). The presence of image noise in CT perfusion introduces inaccuracy in perfusion measurements, necessitating further exploration and reducing the impact of image noise on perfusion parameters. By minimizing noise inaccuracies, researchers and clinicians can more confidently interpret perfusion parameters, leading to a more accurate understanding of tissue perfusion and, consequently, improved clinical decision-making.

Furthermore, the relatively high radiation exposure to patients during the acquisition of CT perfusion limits its clinical applications. The radiation dose associated with CT perfusion has been reported to be often significantly higher than that of a standard unenhanced CT scan (Othman et al. 2017). This increased radiation dose is mainly due to the prolonged duration of the scan, which poses potential risks to patients. To address this concern, an innovative approach involving the dynamic CT perfusion model, FPA as outlined in studies by Hubbard et al. (2018) and Zhao et al. (2020) (Hubbard et al. 2018, Zhao et al. 2020) was developed. This model, requiring only two acquisitions at two specific time points, serves as a

Discussion

promising strategy to reduce radiation exposure while maintaining diagnostic efficacy. Interestingly, previous studies have shown the potential of the FPA technique in the diagnosis and detection of pulmonary diseases and myocardial measurements (Hubbard et al. 2016, Hubbard, Malkasian, Zhao, Abbona, Kwon & Molloy 2019, Hubbard et al. 2022). Intriguingly, despite these promising applications, it should be noted that to date no studies have investigated the potential of the FPA technique in the diagnosis of pancreatic diseases.

Therefore, the objective of this thesis was to standardize and optimize the CT perfusion techniques, focusing on correction of uncertainties in the perfusion measurements and reducing radiation dose. First, a comprehensive quantitative meta-analysis of clinical studies of pancreatic CT perfusion was performed. This investigation focused specifically on evaluating the study parameters and evaluation procedures included in these studies. Furthermore, the objective was to quantitatively discriminate pancreatic diseases based on quantitative perfusion measurements and to identify the acquisition parameters that exert the most significant influence on quantitative results, facilitating further investigation and standardization of CT perfusion protocols. To quantitatively assess and correct the impact of image noise on the precision of CT perfusion BF measurements, a noise correction algorithm using digital perfusion phantoms was developed in this thesis. For further validation of the noise correction algorithm, it was applied to the clinical dataset to evaluate the results of an earlier CT perfusion study and provide an estimate of the precision of the measured perfusion parameters. Additionally, implementation and optimization of a novel FPA CT perfusion technique for pancreatic patients was performed with the aim of reducing radiation exposure and the acquisition time of CT perfusion scans in a clinical setting. This optimized technique was rigorously compared with the MSM reference method, further validating its efficacy and reliability in a clinical context.

In essence, this thesis represents a multifaceted exploration, ranging from a comprehensive meta-analysis of existing pancreatic CT perfusion clinical studies to the development of novel methodologies, all directed toward advancing the precision, reliability, and clinical applicability of pancreatic CT perfusion. The ultimate objective was not only to deepen our understanding of quantitative perfusion measurements in pancreatic diseases, but also to improve the general utility of CT perfusion as a diagnostic modality.

In this chapter, a detailed discussion of the results obtained from this thesis will be presented. To provide a structured overview, the discussion will begin with the results of a quantitative meta-analysis of clinical CT perfusion studies in the context of pancreatic research articles discussed in Section 4.1. Subsequently, the results obtained from the evaluation of the noise correction algorithm developed using digital perfusion phantoms on the accuracy of CT perfusion measurements will be discussed in Section 4.2. Following that, results obtained from the implementation and optimization of the FPA CT perfusion technique for its clinical applications in

the pancreas will be discussed in Section 4.3. In addition, Section 4.4 will discuss the limitations of this thesis and offer an outlook on future developments. Finally, the chapter concludes with the conclusions derived from this thesis, discussed in Section 4.5.

4.1 Meta-analysis of pancreatic CT perfusion studies

The comprehensive quantitative meta-analysis conducted on clinical studies focusing on pancreatic CT perfusion provided valuable insights into the existing trends and patterns of dynamic CT perfusion. The results of the meta-analysis emphasize the significant variations in perfusion measurements in various pancreatic pathologies and healthy tissues. These findings validate the use of CT perfusion as a robust quantitative imaging biomarker in clinical applications of pancreatic diseases. Despite the inherent heterogeneity of the dataset, the research findings are consistent with the individual results of the evaluated studies. This shows consistent and significant differences in perfusion parameters among various pancreatic pathologies and when comparing pathological to non-pathological tissues (see Table 3.3).

However, one of the significant observations from the meta-analysis is the inconsistency observed in permeability measurements and limited number of studies reported permeability for differentiating pancreatic pathologies. This highlights the need for more focused investigations into permeability and its role in differentiating between various pancreatic pathologies. Furthermore, the significant differences reported between non-PDAC and normal pancreas, as seen in individual studies, could not be replicated in this quantitative meta-analysis (Delrue et al. 2012, Zhu et al. 2016). This discrepancy can be explained by the heterogeneous definition of non-PDAC in this meta-analysis, which includes insulinomas and endocrine tumors, to compensate for the limited number of available studies. Furthermore, histopathological studies show an increase in microvascular density in PDAC compared to the normal pancreas, in contrast to a decrease in BF in CT perfusion (see Fig. 3.4), prompting further investigation (Barău et al. 2013)). One hypothesis is that the increased fluid pressure in the tumor stroma leads to reduced BF through the compressed vessels despite high microvessel density (Hessmann et al. 2020), but further in-depth research is necessary.

In this meta-analysis, the evaluations focused mainly on differences between different pathologies, limiting the clinical applicability of the results. For example, the results show significant differences in BF between PDAC and pancreatitis. However, this thesis did not perform a subgroup analysis of mass-forming chronic pancreatitis, which can be challenging to distinguish from PDAC, a notable limitation. This kind of specific clinical application falls beyond the scope of this meta-analysis. However, some individual studies, such as the work of Lu et al. (Lu et al. 2011), have reported promising results for CT perfusion in precisely such

Discussion

challenging clinical scenarios. These promising findings suggest a potential application of the CT perfusion technique in overcoming the challenges associated with distinguishing between mass-forming chronic pancreatitis and PDAC. Although the meta-analysis may not directly address this clinical situation, the promising results reported by specific studies underscore the potential of CT perfusion in complex and challenging pancreatic pathologies.

The observed heterogeneity in study parameters and their evolution over time underscores the need for standardization in CT perfusion measurements. This is particularly crucial to ensure the comparability of findings between studies conducted in different institutions. The variability in quantitative results observed in all studies highlights the importance of addressing the influence of CT examination parameters and evaluation procedures on CT perfusion measurements. Statistical analysis shows the significant impact of multiple acquisition parameters on the quantitative results reported, necessitating the need for standardized protocols. Achieving standardization in acquisition protocols and evaluation procedures is crucial for ensuring the comparability of results between studies and clinical practice. This requires a comprehensive understanding of the specific factors that contribute to variability and the development of guidelines for standardizing key parameters. However, the limited adherence to reporting guidelines and the variability in reporting further underscore the challenges associated with achieving standardization.

Furthermore, the meta-analysis results indicate which parameters might be most important for standardization, while the box-plot analysis provides a qualitative investigation of effect sizes. However, when interpreting these results, different sample sizes for parameters and pathologies must be considered (see Table 3.1). Many studies did not fully comply with the reporting guidelines proposed by the Experimental Cancer Medicine Centre Imaging Network Group in 2012 (Miles et al. 2012), reporting only some acquisition parameters, further limiting sample sizes. In consequence, results regarding BF and normal pancreas should be considered most reliable when interpreting Table 3.3 and Figure 3.6.

Although the current dataset does not allow the recommendation of specific acquisition settings, the results are consistent with previous studies, highlighting the importance of acquisition parameters such as temporal sampling rate (Wintermark et al. 2004), contrast agent injection protocols (Kandel et al. 2009), and image noise (Skornitzke et al. 2019). An additional noteworthy finding underlines the importance of variable temporal sampling, which can be used to reduce the sampling rate after the first pass of the contrast agent, allowing for longer acquisition times without increasing radiation exposure.

It should be noted that the present thesis encountered challenges in replicating previous findings on the influence of the perfusion model on quantitative measurements, as reported by (Schneeweiß et al. 2016). This could be explained by the

absence of consistent reporting on the mode of perfusion by many studies and the wide range of perfusion models used (see Figure 3.2). This aspect emphasizes the necessity for standardized reporting practices in future studies to allow for more robust comparisons and generalized conclusions regarding the influence of perfusion models on perfusion measurements.

4.2 Development of noise correction algorithm

Recognizing the negative impact of image noise on the precision of quantitative CT perfusion measurements, as highlighted in studies (Skornitzke et al. 2019, Juluru et al. 2013), a noise correction algorithm was developed. This algorithm utilized digital perfusion phantoms to quantitatively evaluate and correct the influence of image noise on the accuracy of CT perfusion BF measurements. The successful convergence of the BF measurements observed using the developed algorithm, both in simulated and clinical datasets, signifies the efficiency of the algorithm. This convergence indicates the algorithm’s effectiveness in improving measurement accuracy by correcting for the detrimental impact of image noise and that further iterations are unlikely to significantly improve the performance of the algorithm.

The results obtained from the noise correction algorithm demonstrated a substantial improvement in the BF perfusion measurements in both the pancreatic parenchyma, and pancreatic adenocarcinoma tissue, as detailed in Tables 3.5 and 3.7. Taking into account the results obtained using the noise correction algorithm, the measured noise-corrected BF values showed an estimated relative difference of 36% from the noise-impacted BF values in the case of pancreatic carcinoma. In contrast, the noise-corrected BF values showed a minimal estimated relative difference of only 2.6% from the noise-impacted BF values in pancreatic parenchyma.

Specifically, for the parenchyma tissue region, the GTBF, the measured noise-impacted BF and the noise-corrected BF measurements were recorded as 225 ± 120.9 ml/100ml/min, 218.4 ± 112.4 ml/100ml/min, and 224.1 ± 119.2 ml/100ml/min, respectively (See Table 3.5). In comparison, the GTBF measurements, the noise-impacted BF measurements measured, and the noise-corrected BF measurements for the carcinoma tissue region were 37.5 ± 20.2 ml/100ml/min, 62.1 ± 11.5 ml/100ml/min, and 39.7 ± 21.9 ml/100ml/min, respectively. Therefore, the findings suggest that perfusion measurements in parenchyma tissue can be considered accurate despite image noise, while quantitative evaluations of measurements in pancreatic adenocarcinoma should be treated with caution. These findings underscore the critical importance of precise BF evaluations in understanding and managing pancreatic adenocarcinoma. It should be noted that similar effects may be observed in other organs and pathologies, prompting a broader consideration of these outcomes beyond the scope of pancreatic studies.

Furthermore, the absolute difference between the GTBF and noise-corrected BF values shows a major convergence from 18.77 to 3.56 ml/100ml/min after cor-

Discussion

rection, thus indicating the efficacy of the noise correction algorithm in correcting the impact of image noise on perfusion measurements. The evaluation of model error, representing the systematic component of errors in BF measurements, showed a reduction of 12.63 to 11.03 ml/100ml/min, as indicated in Table 3.6 after noise correction. This decrease signifies a more accurate alignment of the calculated values with the expected model, indicating an improvement in the algorithm's ability to account for systematic errors inherent in the measurement process. Additionally, the random error, reflecting the non-systematic and unpredictable component of errors, decreased from 4.02 to 3.96 ml/100 ml/min, as indicated in Table 3.6. The curve in Figure 3.8 shows that the absolute difference reaches below or almost at the same level of model error and random error after a few iterations. This shows that the algorithm effectively accounts for the variability in the BF measurements and indicates that the algorithm has converged to a stable state.

The improvements in CNR from 2.52 to 2.61, detailed in Table 3.5, indicate a more refined ability to distinguish between tissue types, specifically highlighting the contrast between pathological and non-pathological tissues. Therefore, improved CNR helps improve the detection and diagnosis of pancreatic lesions.

For the digital perfusion phantom, as illustrated in Figure 3.9, the Bland-Altman limits of agreement were calculated and revealed a range of -9.63 to 8.42 ml/100ml/min between GTBF and BFDcorr and -27.18 to 44.01 ml/100ml/min between BFD and BFDcorr. This interval signifies the degree of agreement between GTBF and BFDcorr, and BFD and BFDcorr in the controlled environment of the digital perfusion phantom. The narrow range observed between GTBF and BFDcorr suggests a high level of agreement, indicating that the noise correction algorithm effectively corrected the impact of noise, resulting in consistent and accurate BF measurements. In contrast, the Bland-Altman limits of agreement between BFD and BFDcorr are comparatively wider, signifying greater variability between the two measurements. Additionally, for the clinical dataset, depicted in Figure 3.10 presented a considerably wider range, ranging from -81.67 to 107.55 ml/100ml/min. This broader interval signifies greater variability in agreement between the BFD and BFDcorr measurements within the clinical dataset. The discrepancy observed in the clinical dataset may be attributed to the inherent complexities and dynamic nature of clinical scenarios, where factors such as tissue heterogeneity and physiological variations may contribute to a more diverse range of BF measurements. These Bland-Altman plot results emphasize the effectiveness of the noise correction algorithm in enhancing the precision of BF measurements, particularly within the controlled environment of the digital perfusion phantom. However, the wider limits of agreement in the clinical dataset highlight the inherent challenges and variability associated with real-world clinical applications, emphasizing the need for continued refinement and adaptation of noise correction techniques in complex clinical settings.

While the impact of image noise on quantitative assessments is more pronounced

in certain pathologies, the application of noise correction algorithm proves instrumental in mitigating potential inaccuracies in perfusion measurements. The differential effects observed between pancreatic parenchyma and adenocarcinoma highlight the need for interpretation in clinical practice and reinforce the importance of implementing noise correction techniques, not only in the pancreas but also in broader medical imaging contexts. Further research on the generalizability of these findings to various organs and pathologies will contribute to advancing our understanding of the robustness and limitations of CT perfusion measurements in clinical applications.

The comparison with existing studies highlights the unique contribution of the algorithm developed, which demonstrates its effectiveness in mitigating the impact of noise on quantitative measurements. This not only adds to the current body of literature, but also positions our research as a pioneering effort to refine the accuracy of BF perfusion measurements in the context of pancreatic diseases. This comprehensive correction mechanism not only improves the reliability of our measurements, but also introduces a novel approach to noise reduction in specific imaging conditions relevant to pancreatic patients. The clinical implications of these improved BF values are noteworthy. Accurate perfusion measurements have great potential to improve diagnostic precision and refine treatment planning for pancreatic patients. The enhanced data obtained through our algorithm can empower clinicians with more reliable information, ultimately contributing to improved patient care.

4.3 First pass analysis

Dynamic CT perfusion is an important potential biomarker for enhancing the detection and diagnosis of pancreatic tumors. However, clinical applications of dynamic CT perfusion are restricted by increased patient radiation exposure due to the use of multiple volume acquisitions (Mayer et al. 2021, Xu et al. 2009). Increased radiation exposure raises concerns about patient safety. To address this issue, a novel perfusion measurement approach, the FPA perfusion technique, was implemented and optimized, using only two volume acquisitions. The reduction in the number of volume acquisitions reduces the radiation dose, thus, overcoming one of the critical limitations of dynamic CT perfusion. By addressing the safety concerns related to radiation exposure, the FPA perfusion technique enables broader and more secure clinical applications, offering a promising solution to enhance the feasibility and safety of dynamic CT perfusion in the context of pancreatic imaging.

The findings reveal a high correlation between FPA perfusion measurements and dynamic CT perfusion in pancreatic adenocarcinoma. This correlation suggests that the FPA technique, with its low radiation dose approach, has the potential to serve as a reliable imaging biomarker for perfusion measurements in pancreatic tumors in clinical practice in the near future. The prospect of using FPA as a reliable and low-dose alternative for perfusion measurements in pancreatic tumors

Discussion

could significantly impact patient care by providing clinicians with valuable information while minimizing radiation exposure, thus balancing diagnostic efficacy with patient safety.

Within the scope of this thesis, two FPA approaches were explored. The first FPA approach denoted as FPA1, exhibited the highest correlation ($r = 0.95$) with the reference method, MSM (see Table 3.8). Despite its impressive correlation, FPA1 was deemed unsuitable for clinical applications due to its dependence on knowing the exact acquisition time when the AIF reaches its maximum (t_{max}) before the commencement of the acquisition. This requirement poses challenges in real-world clinical scenarios, where obtaining precise and timely information about AIF may not be practically feasible.

However, the second FPA approach, referred to as FPA2, with a high correlation (Taylor 1990) ($r = 0.82$ to 0.94), depending on the acquisition time) with MSM for a range of acquisition times (see Table 3.8), offers a more practical solution. This approach only requires information on contrast agent injection to estimate the acquisition time of the second volume scan, which is available before the scan. This characteristic makes FPA2 more feasible for clinical implementation compared to FPA1, overcoming the limitation associated with the exact timing requirement. The robustness to changes in perfusion measurements (BF) with changes in acquisition timing within the optimal time range (t_4 - t_9) further underscores the practicality of FPA2. A high correlation of $r = 0.91$ to 0.94 (see Table 3.8) with MSM can be achieved depending on the selection of the acquisition time within the optimum time range. The results showed that half of the injection time plus a fixed dispersion delay provides a high correlation coefficient value at that time, as stated by Hubbard et al. (Hubbard, Malkasian, Zhao, Abbona & Molloy 2019). The determined timings for FPA2 in this thesis also yield results that are almost as good as the theoretical optimum implemented by FPA1. Thus, FPA2 seems to be a practical solution to the theoretical concept of FPA.

However, it's noteworthy that the dispersion delays providing a high correlation with MSM in this thesis differed from the optimum dispersion delay 'd' as reported by Hubbard et al. (Hubbard, Malkasian, Zhao, Abbona & Molloy 2019). In the study by Hubbard et al., the optimum dispersion delay 'd' was reported to be 1 second, whereas the optimum dispersion delay obtained in this study ranges between 7.5 and 12.0 seconds. The reason for this difference in dispersion delays might be the difference in investigated organs, specifically the pancreas in this thesis compared to the myocardium in Hubbard et al.'s study. Hence, it is crucial to consider calculating different dispersion delays based on the specific organ or anatomical region under investigation.

Furthermore, despite variations in acquisition time, the differences in FPA2 perfusion values were minimal, as indicated by the small coefficient of variation (COV). This implies that slight changes in acquisition timing have a negligible

impact on perfusion measurements and, consequently, the accuracy of disease diagnosis. The robustness of FPA2 to changes in acquisition timing or patient perfusion underscores its reliability. Therefore, measuring FPA perfusion within the optimum acquisition time range of t6-t9 could improve the diagnosis of pancreatic carcinoma. Hence, the FPA2 approach seems feasible for application in clinical practice, offering a reliable method for assessing pancreatic diseases.

In the clinical application of FPA2, the process begins with intravenous injection of a non-ionic iodinated contrast agent, followed by a bolus saline solution (NaCl) (Hubbard et al. 2018). Specifically for pancreatic imaging, the first volume scan of FPA is scheduled to be acquired after the contrast agent bolus reaches a threshold of 120 HU in the abdominal aorta, which can be precisely achieved by bolus tracking. Subsequently, the second volume scan is planned for acquisition after a delay ranging from 15.5 to 20.0 seconds, based on the findings of the current thesis. This outlined procedure provides a clear and practical guideline for implementing the FPA2 technique in clinical settings, ensuring optimal timing for accurate perfusion measurements in pancreatic imaging.

Theoretically, the implementation of FPA, utilizing only two volume scans, presents a substantial reduction in total scan time compared to conventional CT perfusion. As depicted in Figure 3.15 in the proposed FPA technique, the potential reduction in scan time has been noticed, decreasing from 49.68 seconds in conventional CT perfusion to 27.02 seconds. This represents a potential reduction of up to 45.62% in scan time, offering a solution to the motion artifacts present in other CT perfusion measurements due to prolonged breath hold during a more prolonged scan duration.

Furthermore, FPA considerably limits radiation exposure to the patient, by using only two volume acquisitions compared to multiple volume scans required by conventional CT perfusion. For the implementation of the FPA, the two-volume scans would have been achieved at an effective radiation dose of only 0.27 ± 0.14 mSv as compared to 4.64 ± 2.32 mSv radiation dose required by dynamic CT perfusion (see Figure 3.15). This represents a potential reduction of up to 94% in the effective radiation dose, excluding the effective dose of bolus tracking. Considering the substantial reduction in radiation exposure and scan time achieved by the proposed FPA2 compared to conventional CT perfusion, this technique could be established as a potential imaging biomarker for the quantitative detection, diagnosis of disease, and treatment planning, particularly in the context of pancreatic tumors in clinical practice.

4.4 Limitations and future developments

The primary limitation of this meta-analysis lies in the limited number of included studies, which is based on the limited availability of research articles specifically focused on pancreatic CT perfusion. This constraint is further compounded by

Discussion

incomplete reporting of CT perfusion parameters in some studies, which limits the sample size for some of the evaluations in this thesis. Consequently, the sample size was also even more limited for some of the investigated pancreatic pathologies, which resulted in the pooling of all tumor entities that are not pancreatic adenocarcinoma in a heterogeneous non-PDAC group.

Similarly, some studies reported measurements for normal pancreatic tissue and pathological tissue from the same patients. However, it is essential to acknowledge that the influence of the investigated diseases on normal tissue cannot be entirely ruled out. Therefore, a further distinction between patients with and without pancreatic disease might be necessary (Barău et al. 2013). Due to the small sample size, multivariate statistical analysis was not feasible, and only the detection and distinction of tumors/PDAC and pancreatitis were statistically validated in this thesis.

Additionally, exploring studies conducted for different organs, such as the brain, where a larger number of studies might be available, could provide further insights. However, caution is necessary when interpreting and comparing results across different organs and body regions due to physiological differences. Consequently, findings from this meta-analysis should not be directly extrapolated to perfusion studies of other organs and regions of the body.

Moreover, this meta-analysis incorporated studies spanning over 25 years, during which there were substantial advancements in CT technology. Despite these technological developments, the reported perfusion values across this period remained compatible with each other. The statistical analysis conducted in this meta-analysis did not reveal a significant effect for many parameters indicative of technological progress, such as anatomical coverage. It's important to note that all study parameters from individual studies were included in the analysis as reported to avoid any bias toward certain sets of parameters.

It is crucial to acknowledge that, while this meta-analysis highlights the study parameters significantly influencing the reported quantitative measurements, prospective studies are needed to determine optimum settings for these parameters.

In view of its use in clinical practice, both CT perfusion and MRI play a valuable role in tumor detection, particularly when a suspected pancreatic tumor is not visible on routine pancreatic CT imaging (National Comprehensive Cancer Network 2023). Direct comparisons between CT perfusion and diffusion-weighted (DW) MRI in PDAC patients have been reported in two small studies. These studies concluded that CT perfusion and (DW)-MRI parameters are comparably applicable for differentiating PDAC lesions from non-neoplastic pancreatic tissue (Kovač et al. 2019, Mayer et al. 2021). Furthermore, the performance of PET / CT and CT perfusion has been reported to exceed the performance of standard CT for the detection of insulinoma (Zhu et al. 2017, Yang et al. 2021). However, studies

that directly compare these imaging modalities are lacking. These findings underscore the complementary roles of CT perfusion and MRI in enhancing diagnostic capabilities, especially in scenarios where conventional imaging methods may not provide sufficient visibility of suspected pancreatic tumors.

Furthermore, a major limitation of standard pancreatic CT lies in its inability to reliably assess the response of PDAC lesions to (radio-)chemotherapy (RCT) since standard CT faces challenges in differentiating post-treatment fibroinflammatory changes from residual viable tumor tissue (Soloff et al. 2022). In this context, both diffusion-weighted MRI (DW-MRI) and perfusion CT have shown potential for predicting histopathological response after RCT (Hamdy et al. 2019, Soloff et al. 2022). However, there is currently a lack of studies directly comparing these imaging modalities in their ability to assess the response of PDAC lesions to RCT. This highlights the need for further research to establish the comparative effectiveness of DW-MRI and perfusion CT in evaluating treatment response in PDAC patients, offering potential advancements in the management and monitoring of therapeutic interventions.

The noise correction algorithm focused exclusively on correcting the accuracy of BF perfusion measurements, neglecting other perfusion parameters such as BV, FEP or MTT, etc. Furthermore, only the effect of image noise on TACs was considered during the development of the algorithm, leaving out the potential effects of AIF in a clinical setting. While AIF measurements are typically averaged over a region of interest, which reduces the impact of image noise to some extent, preliminary measurements indicate that a noisy AIF can still influence perfusion measurements. However, evaluating the effect of noise on AIF is challenging in practice, primarily due to limitations in commercially available CT perfusion software. With the digital perfusion phantoms used in this thesis, 16128 TACs can be evaluated simultaneously, while only one AIF can be evaluated at a time. In consequence, it is not feasible to evaluate AIFs in this manner.

It is essential to note that the evaluations in this study were based on the commercial implementation of only one perfusion model, Deconvolution, and by one vendor. However, the results obtained are expected to have similar implications for other vendors. However, it's important to exercise caution when generalizing these findings to other models and vendors, as variations in software implementations and algorithms may introduce differences.

Additionally, the unavailability of GTBF measurements in the patient dataset and instances where BF approached zero even after correction underscore the need for further refinement and broader implementation of the noise correction algorithm. Future research should consider applying the algorithm to different perfusion models and datasets, taking into account the potential impact of image noise on various perfusion parameters. This iterative process of refinement and expansion will contribute to a more comprehensive understanding of noise correction

Discussion

algorithms in the context of clinical CT perfusion studies.

Furthermore, while the novel CT perfusion approach, the FPA technique, developed in this thesis holds promise as a potential alternative to dynamic CT perfusion, it is essential to recognize its current limitations. The relatively small sample size limited to 16 patients in this thesis, emphasizes the need for further implementation of the FPA technique on larger datasets to enhance the reliability and generalizability of the findings. Larger datasets allow for a more robust statistical analysis and a better understanding of the technique's performance across a broader patient population.

Moreover, it is crucial to recognize that this FPA analysis is retrospective, and prospective validation of the proposed acquisition time seems necessary to ensure the reliability and effectiveness of the technique in real-time clinical practices. Prospective studies would provide more controlled settings for validation and contribute to establishing the clinical utility of the FPA technique.

Additionally, the absence of qualitative evaluation and investigation of the diagnostic use of FPA perfusion maps represents a limitation that requires further verification. Qualitative assessments and clinical validations are essential steps in confirming the diagnostic efficacy of the FPA technique. These aspects should be addressed in future studies to comprehensively evaluate the clinical applicability and diagnostic value of FPA in comparison to established technique dynamic CT perfusion.

Thus, future research aims to further refine the noise correction algorithm developed and explore other perfusion parameters as well such as BV and permeability. Additionally, further investigation is needed to assess the applicability of the noise correction algorithm across different perfusion models and various vendors. This comparative analysis will focus on potential variations introduced by different software implementations and vendors. Further, correcting the inter and intra-vendor, as well as inter and intra-model differences in the perfusion measurements based on image noise, will be a critical step toward standardization and ensuring the reproducibility of results across different settings. Future research may also include exploring additional parameters other than image noise that contribute to the variability in CT perfusion measurements. Furthermore, further investigation of the FPA model is required before the actual application of this model in routine clinical practice. Prospective studies, along with qualitative evaluations, will be necessary to establish the reliability and diagnostic utility of the FPA technique. In general, future research should focus on addressing these aspects to enhance the robustness and clinical relevance of CT perfusion measurements.

4.5 Conclusion

In conclusion, this thesis has addressed critical challenges in CT perfusion studies of the pancreas, emphasizing the need for standardization, the impact of image noise, and concerns related to radiation exposure. The development and application of the noise correction algorithm and the FPA technique represent significant steps toward making CT perfusion scans more clinically acceptable.

The meta-analysis provided valuable information on the importance of CT perfusion in pancreatic pathologies, as the results of individual studies could be reproduced in the pooled data set despite the heterogeneity in CT protocols between studies. In addition, the need for standardization of CT perfusion protocols is highlighted, as a significant influence of study parameters on the reported quantitative results was observed.

Additionally, the thesis further demonstrates the effectiveness of the noise correction algorithm in improving BF measurements in pancreatic patients. The convergence of BF in both simulated and patient data signifies the efficacy of the algorithm developed to improve the accuracy of the measurement by correcting the negative influence of image noise. With further refinement, the algorithm has the potential to standardize perfusion measurements, improving comparability between patients, imaging centers, and equipment vendors, thus contributing to more accurate diagnosis and treatment planning.

The proposed FPA approach for perfusion measurements uses only two volume scans, where the first scan is acquired after the threshold of 120 HU is reached in the abdominal aorta, followed by the second scan acquired 15.5 to 20.0 seconds after the first scan, has the potential to provide an alternative imaging biomarker to conventional dynamic CT perfusion for the pancreas. FPA shows the ability to differentiate pancreatic adenocarcinoma from pancreatic parenchyma tissue with a high correlation to the reference standard, MSM. Most importantly, FPA could also allow for a large decrease in patient radiation exposure and scan time compared to conventional dynamic CT perfusion to evaluate pancreatic diseases.

In general, this thesis makes significant contributions to the advancement of CT perfusion studies in the pancreas, addressing key issues, and presenting innovative approaches that have the potential to enhance the clinical utility of this imaging modality.

The greatest discovery of my generation is that a human being can alter his life by altering his attitudes.

William James

5

Summary

The pancreas located in abdominal cavity of the human body, plays essential role in digestion and blood sugar regulation. Various medical conditions such as pancreatic tumors or cystic lesions can disrupt its normal functioning. CT perfusion is the most commonly used functional imaging technique in diagnosing these tumors. However, its widespread adoption in clinical practice has been limited by several challenges. One significant obstacle is the absence of standardized protocols for image acquisition. Moreover, image noise can negatively impact perfusion measurements, resulting in inaccuracies when quantifying tissue perfusion, thereby compromising its clinical effectiveness. Efforts to mitigate image noise and improve image quality are essential to enhance the accuracy of CT perfusion measurements. Another critical limitation of CT perfusion is the associated radiation exposure, which poses risks to patients, particularly in vulnerable populations such as children and pregnant women.

The objective of this thesis was to conduct a comprehensive meta-analysis of CT perfusion within the context of pancreatic research articles. This involves collecting and analyzing a large number of published research articles related to pancreatic CT perfusion, with a focus on including studies that report quantitative perfusion parameters derived from CT perfusion. Furthermore, the aim was to identify acquisition parameters that influence quantitative measurements, facilitating standardization of those parameters. Additionally, noise correction algorithm was developed using digital perfusion phantoms to mitigate the negative impact of image noise on BF perfusion measurements. Further, for reducing radiation exposure and acquisition time of CT perfusion, a novel perfusion technique namely, FPA was implemented. FPA model was validated using the most commonly used CT perfusion model, MSM. In contrast to CT perfusion using multiple volume acquisitions, FPA uses only two volume acquisitions. The timing for these two volume acquisitions was estimated and optimized based on the information about contrast agent injection. The reduction in number of volume acquisitions reduces the radi-

Summary

ation dose, hence, overcoming one of the critical limitations of CT perfusion.

The meta-analysis findings indicated an upward trend in number of CT perfusion studies and sample size since 2009. Furthermore, there was an increase in amount of contrast agent and iodine levels used over the years. The tube potential showed a slight decrease, while tube current-time product increased gradually. Anatomical coverage expanded, and slice thickness decreased over time. Most studies reported significant differences in BF and BV between normal pancreatic tissue and pathological conditions. However, the findings for permeability were less consistent, with only about half of the studies showing significant differences. Additionally, most research studies preferred vendor-supplied software for post-processing, and MSM is the most commonly used model to quantify pancreatic perfusion. It has been found that certain CT acquisition parameters had statistically significant effect on quantitative perfusion measurements, particularly when comparing normal versus pathological pancreatic tissue.

The findings from noise correction algorithm demonstrated a significant improvement in the accuracy of BF measurements. Detailed analysis of GTBF, noise-impacted BF, and corrected BF values across various tissue regions showed the efficacy of noise correction in mitigating the adverse effects of noise on BF perfusion measurements, leading to more precise quantification of tissue perfusion. Moreover, the observed enhancements in CNR and agreement between GTBF and noise-corrected BF measurements further underscored the utility of noise-correction algorithms in refining BF measurements.

The results from FPA technique demonstrated a strong correlation in perfusion measurements when compared to the reference method, MSM. Small COV and box plot analysis revealed reduced BF variation over acquisition time, particularly in parenchyma tissue. Therefore, a high correlation to MSM could be achieved depending upon selection of acquisition time within the optimum time range. Variations across tissue types were statistically significant, emphasizing the discriminative capabilities of FPA. Moreover, FPA exhibited advantages in terms of reduced radiation exposure and acquisition times compared to conventional CT perfusion techniques.

For clinical application of FPA, the process begins with intravenous injection of a nonionic iodinated contrast agent, followed by a bolus of saline solution (NaCl). Specifically for pancreatic imaging, first volume scan is to be acquired after contrast agent bolus reaches a threshold of 120 HU in the abdominal aorta, which can be precisely achieved by bolus tracking. Subsequently, the second volume scan is planned after a delay ranging from 15.5 to 20.0 seconds, based on the findings of current thesis.

In conclusion, this thesis has addressed critical challenges of CT perfusion, emphasizing the need for standardization of protocols, the impact of image noise, and concerns related to radiation exposure. The development and application of the noise correction algorithm and FPA technique represent significant steps toward making CT perfusion scans more clinically acceptable.

Wenn Sie keine Fehler machen, arbeiten Sie nicht an schwierigen Problemen. Und das ist ein Fehler.

Frank Wilczek

6

Zusammenfassung

Die Bauchspeicheldrüse befindet sich in der Bauchhöhle des menschlichen Körpers und spielt eine wichtige Rolle bei der Verdauung und der Blutzuckerregulierung. Verschiedene Erkrankungen wie Tumore oder zystische Läsionen der Bauchspeicheldrüse können ihre normale Funktion stören. Die CT-Perfusion ist die am häufigsten verwendete funktionelle Bildgebungstechnik zur Diagnose dieser Tumore. Ihre breite Anwendung in der klinischen Praxis wird jedoch durch mehrere Probleme behindert. Ein wesentliches Hindernis ist das Fehlen von standardisierten Protokollen für die Bildaufnahme. Darüber hinaus kann sich das Bildrauschen negativ auf die Perfusionsmessungen auswirken, was zu Ungenauigkeiten bei der Quantifizierung der Gewebedurchblutung führt und damit die klinische Aussagekraft des Verfahrens beeinträchtigt. Um die Genauigkeit der CT-Perfusionsmessungen zu erhöhen, sind Anstrengungen zur Verringerung des Bildrauschens und zur Verbesserung der Bildqualität unerlässlich. Eine weitere kritische Einschränkung der CT-Perfusion ist die damit einhergehende Strahlenbelastung, die - insbesondere für gefährdete Bevölkerungsgruppen wie Kinder und Schwangere - ein Risiko darstellt. Ziel dieser Arbeit war es, eine umfassende Meta-Analyse der CT-Perfusion im Kontext von wissenschaftlichen Publikationen zur Bauchspeicheldrüse durchzuführen. Dazu wurde eine große Anzahl von veröffentlichten Forschungsartikeln zur CT-Perfusion der Bauchspeicheldrüse gesammelt und analysiert. Dabei lag der Schwerpunkt auf der Einbeziehung von Studien, die über - aus der CT-Perfusion abgeleiteten - quantitative Perfusionsparameter berichten. Darüber hinaus wurde versucht, Aufnahmeparameter zu identifizieren, welche die quantitativen Messungen beeinflussen, um eine Standardisierung dieser Parameter zu ermöglichen. Zudem hinaus wurde ein Algorithmus zur Rauschkorrektur unter Verwendung digitaler Perfusionsphantome entwickelt, um die negativen Auswirkungen des Bildrauschens auf die BF-Perfusionsmessungen abzuschwächen. Um die Strahlenbelastung und die Aufnahmezeit der CT-Perfusion zu reduzieren, wurde eine neuartige Perfusionstechnik, namens FPA, implementiert. Das FPA-Modell wurde anhand des

Zusammenfassung

am häufigsten verwendeten CT-Perfusionsmodells (MSM) validiert. Im Gegensatz zur CT-Perfusion mit mehreren Volumenaufnahmen werden bei der FPA nur zwei Volumenaufnahmen durchgeführt. Das Timing für diese beiden Volumenaufnahmen wurde auf der Grundlage der Informationen über die Kontrastmittelinjektion geschätzt und optimiert. Durch die Verringerung der Anzahl der Volumenaufnahmen wird die Strahlendosis reduziert und somit eine der kritischen Einschränkungen der CT-Perfusion überwunden.

Die Ergebnisse der Meta-Analyse deuten auf einen Aufwärtstrend bei der Anzahl der CT-Perfusionsstudien und der Stichprobengröße seit 2009 hin. Außerdem nahmen die Menge des verwendeten Kontrastmittels und die Jodmenge im Laufe der Jahre zu. Die Röhrenspannung ging leicht zurück, während das Strom-Zeit-Produkt der Röhre allmählich anstieg. Die anatomische Abdeckung nahm zu, und die Schichtdicke nahm im Laufe der Zeit ab. Die meisten Studien berichteten über signifikante Unterschiede bei BF und BV zwischen normalem Pankreasgewebe und pathologischen Zuständen. Die Ergebnisse für die Permeabilität waren jedoch weniger konsistent, wobei nur etwa die Hälfte der Studien signifikante Unterschiede zeigte. Darüber hinaus bevorzugten die meisten Forschungsstudien eine vom Hersteller bereitgestellte Software für die Nachbearbeitung. MSM ist das am häufigsten verwendete Modell zur Quantifizierung der Pankreasperfusion. Es wurde festgestellt, dass bestimmte CT-Aufnahmeparameter statistisch signifikante Auswirkungen auf die quantitativen Perfusionsmessungen hatten, insbesondere beim Vergleich von normalem mit pathologischem Pankreasgewebe.

Die Ergebnisse des Rauschkorrekturalgorithmus zeigten eine signifikante Verbesserung der Genauigkeit der BF-Messungen. Eine detaillierte Analyse der GTBF-, rauschbeeinflussten BF- und korrigierten BF-Werte in verschiedenen Geweberegionen zeigte die Wirksamkeit der Rauschkorrektur bei der Abschwächung der nachteiligen Auswirkungen des Rauschens auf die BF-Perfusionsmessungen, was zu einer präziseren Quantifizierung der Gewebepfusion führte. Darüber hinaus unterstrichen die beobachteten Verbesserungen der CNR und der Übereinstimmung zwischen GTBF und rauschkorrigierten BF-Messungen den Nutzen von Algorithmen zur Rauschkorrektur bei der Verfeinerung von BF-Messungen.

Die Ergebnisse der FPA-Technik zeigten eine starke Korrelation der Perfusionsmessungen im Vergleich zur Referenzmethode MSM. Eine kleine COV- und Boxplot-Analyse ergab eine geringere BF-Variation über die Erfassungszeit, insbesondere im Parenchymgewebe. Daher konnte eine hohe Korrelation zu MSM erreicht werden, wenn die Aufnahmezeit innerhalb des optimalen Zeitbereichs gewählt wurde. Die Variationen zwischen den Gewebetypen waren statistisch signifikant, was die Unterscheidungsfähigkeit der FPA unterstreicht. Darüber hinaus wies die FPA im Vergleich zu konventionellen CT-Perfusionsverfahren Vorteile in Bezug auf eine geringere Strahlenbelastung und kürzere Aufnahmezeiten auf.

Bei der klinischen Anwendung der FPA beginnt das Verfahren mit der intravenösen Injektion eines nichtionischen jodhaltigen Kontrastmittels, gefolgt von einem Bolus mit Kochsalzlösung (NaCl). Speziell für die Bildgebung der Bauchspeicheldrüse ist der erste Volumenscan zu erstellen, nachdem der Kontrastmittelbolus einen Schwellenwert von 120 HU in der Bauchaorta erreicht hat, was durch Bolus-

Tracking präzise erreicht werden kann. Anschließend wird der zweite Volumenscan, basierend auf den Ergebnissen der aktuellen Arbeit, nach einer Verzögerung von 15,5 bis 20,0 Sekunden geplant.

Zusammenfassend lässt sich sagen, dass in dieser Arbeit kritische Herausforderungen der CT-Perfusion angesprochen wurden, wobei die Notwendigkeit der Standardisierung von Protokollen, die Auswirkungen des Bildrauschens und die Bedenken bezüglich der Strahlenbelastung hervorgehoben wurden. Die Entwicklung und Anwendung des Rauschkorrekturalgorithmus und der FPA-Technik sind wichtige Schritte, um CT-Perfusionsscans klinisch akzeptabler zu machen.

Science is the bridge that connects our dreams with reality, and empowers us to shape the future we envision.

Michio Kaku

7

Bibliography

- Abels, B., Klotz, E., Tomandl, B. F., Villablanca, J. P., Kloska, S. P. & Lell, M. M. (2011), ‘CT Perfusion in Acute Ischemic Stroke: A Comparison of 2-Second and 1-Second Temporal Resolution’, *American Journal of Neuroradiology* **32**(9), 1632–1639.
- Aksoy, F. G. & Lev, M. H. (2000), ‘Dynamic contrast-enhanced brain perfusion imaging: Technique and clinical applications’, *Seminars in Ultrasound, CT and MRI* **21**(6), 462–477.
- Almeida, R. R., Lo, G. C., Patino, M., Bizzo, B., Canellas, R. & Sahani, D. V. (2018), ‘Advances in Pancreatic CT Imaging’, *American Journal of roentgenology* **211**(1), 52–66.
- Alomary, A., Sulieman, A., Alsufayan, M., Alabdurazaq, F., Faisal, N., Qari, A., Alanazi, B. M., Alsaadi, M., Tamam, N., Alkhybari, E. & Bradley, D. A. (2022), ‘Evaluation of radiation exposure for patients undergoing computed tomography perfusion procedure for acute ischemic stroke’, *Radiation Physics and Chemistry* **201**, 110447.
- American Society of Clinical Oncology (ASCO) Cancer.Net (2023), ‘Pancreatic cancer: Statistics’. [date assessed 08 Feb 2024].
URL: <https://www.cancer.net/cancer-types/pancreatic-cancer/statistics>
- Aslan, S., Nural, M. S., Camlidag, I. & Danaci, M. (2019), ‘Efficacy of perfusion CT in differentiating of pancreatic ductal adenocarcinoma from mass-forming chronic pancreatitis and characterization of isoattenuating pancreatic lesions’, *Abdominal Radiology* **44**(2), 593–603.
- Bao, J., Liu, A., Zhao, C., Hao, F., Su, X., Bao, L. & Zhao, L. (2019), ‘Correlation Between Dual-Energy Computed Tomography Single Scan and Computed To-

- mography Perfusion for Pancreatic Cancer Patients: Initial Experience', *Journal of Computer Assisted Tomography* **43**(4), 599–604.
- Barău, A., Ruiz-Sauri, A., Valencia, G., Gómez-Mateo, M. d. C., Sabater, L., Ferrandez, A. & Llombart-Bosch, A. (2013), 'High microvessel density in pancreatic ductal adenocarcinoma is associated with high grade', *Virchows Archiv* **462**, 541–546.
- Bhatt, S., Srivastava, A. K., Meena, N. & Thakur, S. (2017), 'Appraisal of radiation dose with 64-slice computed tomography perfusion in lung cancer patients with special reference to SSDE: An initial experience in a tertiary care hospital', *The Indian Journal of Radiology and Imaging* **27**(4), 389–396.
- Bivard, A. (2013), Perfusion imaging in acute and evolving brain ischemia, Phd thesis, University of Newcastle, Australia.
- Bize, P. E., Platon, A., Becker, C. D. & Poletti, P. A. (2006), 'Perfusion measurement in acute pancreatitis using dynamic perfusion MDCT', *American Journal of Roentgenology* **186**(1), 114–118.
- Cenic, A., Nabavi, D. G., Craen, R. A., Gelb, A. W. & Lee, T.-Y. (1999), 'Dynamic CT Measurement of Cerebral Blood Flow: A Validation Study', *American Journal of Neuroradiology* **20**(1), 63–73.
- Chen, F.-M., Ni, J.-M., Zhang, Z.-Y., Zhang, L., Li, B. & Jiang, C.-J. (2016), 'Presurgical Evaluation of Pancreatic Cancer: A Comprehensive Imaging Comparison of CT Versus MRI', *American Journal of Roentgenology* **206**(3), 526–535.
- Chu, L. L., Knebel, R. J., Shay, A. D., Santos, J., Badawi, R. D., Gandara, D. R. & Knollmann, F. D. (2018), 'CT perfusion imaging of lung cancer: benefit of motion correction for blood flow estimates', *European Radiology* **28**(12), 5069–5075.
- Cuenod, C. & Balvay, D. (2013), 'Perfusion and vascular permeability: Basic concepts and measurement in DCE-CT and DCE-MRI', *Diagnostic and Interventional Imaging* **94**(12), 1187–1204.
- D. Piparo, G. Quast, M. Z. (2024), 'A ROOT Guide For Beginners'. [date accessed 01 February 2024].
URL: <https://root.cern.ch/root/html/doc/guides/primer/ROOTPrimer.html>
- Deak, P. D., Smal, Y. & Kalender, W. A. (2010), 'Multisection CT Protocols: Sex- and Age-specific Conversion Factors Used to Determine Effective Dose from Dose-Length Product', *Radiology* **257**(1), 158–166.
- Delrue, L., Blanckaert, P., Mertens, D., Cesmeli, E., Ceelen, W. P. & Duyck, P. (2011), 'Assessment of tumor vascularization in pancreatic adenocarcinoma using 128-slice perfusion computed tomography imaging', *Journal of Computer Assisted Tomography* **35**(4), 434–438.

- Delrue, L., Blanckaert, P., Mertens, D., Van Meerbeeck, S., Ceelen, W. & Duyck, P. (2012), 'Tissue perfusion in pathologies of the pancreas: assessment using 128-slice computed tomography', *Abdominal Imaging* **37**, 595–601.
- Do R. K., Reyngold M., Raudyal R., Oh J. H., Konar A. S., LoCastro E., Goodman K. A., Dave A. S. (2020), 'Diffusion-Weighted and Dynamic Contrast-Enhanced MRI Derived Imaging Metrics for Stereotactic Body Radiotherapy of Pancreatic Ductal Adenocarcinoma: Preliminary Findings', *Tomography* **6**(2), 261–271.
- Donahue, J. & Wintermark, M. (2015), 'Perfusion CT and acute stroke imaging: Foundations, applications, and literature review', *Journal of Neuroradiology* **42**(1), 21–29.
- D'Onofrio, M., Gallotti, A., Mantovani, W., Crosara, S., Manfrin, E., Falconi, M., Ventriglia, A., Zamboni, G. A., Manfredi, R. & Pozzi Mucelli, R. (2013), 'Perfusion CT can predict tumoral grading of pancreatic adenocarcinoma', *European Journal of Radiology* **82**(2), 227–233.
- Doğan, N. Ö. (2018), 'Bland-Altman analysis: A paradigm to understand correlation and agreement', *Turkish Journal of Emergency Medicine* **18**(4), 139–141.
- Fieselmann, A., Kowarschik, M., Ganguly, A., Hornegger, J. & Fahrig, R. (2011), 'Deconvolution-Based CT and MR Brain Perfusion Measurement: Theoretical Model Revisited and Practical Implementation Details', *International Journal of Biomedical Imaging* **2011**, 467563.
- Garcia, P., Genin, G., Bret, P. M., Bonaldi, V. M., Reinhold, C. & Atri, M. (1999), 'Hepatic CT enhancement: effect of the rate and volume of contrast medium injection in an animal model', *Abdominal Imaging* **24**(6), 597–603.
- Garnett, R. (2020), 'A comprehensive review of dual-energy and multi-spectral computed tomography', *Clinical Imaging* **67**, 160–169.
- Gaspard d'Assignies, Anne Couvelard, S., Vullierme, M.-P., Pascal Hammel, O. H., Sauvanet, A., Bedossa, P., Ruszniewski, P. & Valérie Vilgrain (2009), 'Pancreatic endocrine tumors: Tumor blood flow assessed with perfusion CT reflects angiogenesis and correlates with prognostic factors', *Radiology* **250**(2), 407–416.
- Gibaud, B. (2008), The DICOM Standard: A Brief Overview, in Y. Lemoigne & A. Caner, eds, 'Molecular Imaging: Computer Reconstruction and Practice', Springer Netherlands, Dordrecht, pp. 229–238.
- Goh, V., Shastry, M., Engledow, A., Reston, J., Wellsted, D. M., Peck, J., Endozo, R., Rodriguez-Justo, M., Taylor, S. A., Halligan, S. & Groves, A. M. (2011), 'Commercial software upgrades may significantly alter Perfusion CT parameter values in colorectal cancer', *European Radiology* **21**(4), 744–749.
- Goldman, L. W. (2007), 'Principles of CT and CT Technology', *Journal of Nuclear Medicine Technology* **35**(3), 115–128.

- Hamdy, A., Ichikawa, Y., Toyomasu, Y., Nagata, M., Nagasawa, N., Nomoto, Y., Sami, H. & Sakuma, H. (2019), 'Perfusion CT to assess response to neoadjuvant chemotherapy and radiation therapy in pancreatic ductal adenocarcinoma: Initial experience', *Radiology* **292**(3), 628–635.
- Han, J. K., Kim, A. Y., Lee, K. Y., Seo, J. B., Kim, T. K., Choi, B. I., Lhee, C. S. & Han, M. C. (2000), 'Factors influencing vascular and hepatic enhancement at CT: experimental study on injection protocol using a canine model', *Journal of Computer Assisted Tomography* **24**(3), 400–406.
- Hansen, M., Norling, R., Lauridsen, C., Fallentin, E., Bæksgaard, L., Kofoed, K., Svendsen, L. & Nielsen, M. (2013), 'Computed Tomography (CT) Perfusion in Abdominal Cancer: Technical Aspects', *Diagnostics* **3**(2), 261–270.
- Harrison, J., Balonov, M., Bochud, F., Martin, C., Menzel, H.-G., Ortiz-Lopez, P., Smith-Bindman, R., Simmonds, J. & Wakeford, R. (2021), 'ICRP Publication 147: Use of Dose Quantities in Radiological Protection', *Annals of the ICRP* **50**(1), 9–82.
- Hessmann, E., Buchholz, S. M., Demir, I. E., Singh, S. K., Gress, T. M., Ellenrieder, V. & Neesse, A. (2020), 'Microenvironmental determinants of pancreatic cancer', *Physiological reviews* **100**(4), 1707–1751.
- Hosoki, T. (1983), 'Dynamic CT of pancreatic tumors', *American Journal of Roentgenology* **140**(5), 959–965.
- Hounsfield, G. N. (1980), 'Computed medical imaging. Nobel lecture, December 8, 1979', *Journal of Computer Assisted Tomography* **4**(5), 665–674.
- Hubbard, L., Lipinski, J., Ziemer, B., Malkasian, S., Sadeghi, B., Javan, H., Groves, E. M., Dertli, B. & Molloy, S. (2018), 'Comprehensive assessment of coronary artery disease by using first-pass analysis dynamic CT perfusion: Validation in a swine model', *Radiology* **286**(1), 93–102.
- Hubbard, L., Malkasian, S. & Molloy, S. (2022), 'Dynamic CT myocardial perfusion without image registration', *Scientific Reports* **12**(1), 12608–12608.
- Hubbard, L., Malkasian, S., Zhao, Y., Abbona, P., Kwon, J. & Molloy, S. (2019), 'Low-Radiation-Dose Stress Myocardial Perfusion Measurement Using First-Pass Analysis Dynamic Computed Tomography: A Preliminary Investigation in a Swine Model', *Investigative Radiology* **54**(12), 774–780.
- Hubbard, L., Malkasian, S., Zhao, Y., Abbona, P. & Molloy, S. (2019), 'Timing optimization of low-dose first-pass analysis dynamic CT myocardial perfusion measurement: validation in a swine model', *European radiology experimental* **3**(1), 16–16.
- Hubbard, L., Ziemer, B., Lipinski, J., Sadeghi, B., Javan, H., Groves, E. M., Malkasian, S. & Molloy, S. (2016), 'Functional Assessment of Coronary Artery Disease

- Using Whole-Heart Dynamic Computed Tomographic Perfusion', *Circulation: Cardiovascular Imaging* **12**, e005325.
- ICRP (2002), *Basic anatomical and physiological data for use in radiological protection: reference values*, Vol. 32, ICRP Publication 89.
- Jiang Hsieh, T. F. (2021), 'Computed tomography recent history and future perspectives - PMC', *Journal of Medical Imaging* **8**(5), 052109.
- Johnson, H. J., McCormick, M. M., Luis Ibañez & the Insight Software Consortium (2021), 'The ITK Software Guide'. [date accessed 01 February 2024].
URL: <https://itk.org/ItkSoftwareGuide.pdf>
- Juluru, K., Shih, J., Raj, A., Comunale, J., Delaney, H., Greenberg, E., Hermann, C., Liu, Y., Hoelscher, A., Al Khor, N. & Sanelli, P. (2013), 'Effects of Increased Image Noise on Image Quality and Quantitative Interpretation in Brain CT Perfusion', *American journal of neuroradiology* **34**(8), 1506–1512.
- Jung, H. (2021), 'Basic Physical Principles and Clinical Applications of Computed Tomography', *Progress in Medical Physics* **32**(1), 1–17.
- Kalpić, D., Hlupić, N. & Lovrić, M. (2011), *Student's t-Tests*, Springer Berlin Heidelberg, Berlin, Heidelberg, pp. 1559–1563.
- Kanda, T., Yoshikawa, T., Ohno, Y., Fujisawa, Y., Kanata, N., Yamaguchi, M., Seo, Y., Yano, Y., Koyama, H., Kitajima, K., Takenaka, D. & Sugimura, K. (2012), 'Perfusion measurement of the whole upper abdomen of patients with and without liver diseases: Initial experience with 320-detector row CT', *European Journal of Radiology* **81**(10), 2470–2475.
- Kandel, S., Kloeters, C., Meyer, H., Hein, P., Hilbig, A. & Rogalla, P. (2009), 'Whole-organ perfusion of the pancreas using dynamic volume CT in patients with primary pancreas carcinoma: Acquisition technique, post-processing and initial results', *European Radiology* **19**(11), 2641–2646.
- Karpińska, M. & Czauderna, M. (2022), 'Pancreas—Its Functions, Disorders, and Physiological Impact on the Mammals' Organism', *Frontiers in Physiology* **13**, 807632.
- Khammar, A., Yarahmadi, M. & Madadzadeh, F. (2020), 'What Is Analysis of Covariance (ANCOVA) and How to Correctly Report its Results in Medical Research?', *Iranian Journal of Public Health* **49**(5), 1016–1017.
- Kim, S. H., Kamaya, A. & Willmann, J. K. (2014), 'CT perfusion of the liver: Principles and applications in oncology', *Radiology* **272**(2), 322–344.
- Kitagawa, K., Goto, Y., Nakamura, S., Takafuji, M., Hamdy, A., Ishida, M. & Sakuma, H. (2018), 'Dynamic CT Perfusion Imaging: State of the Art', *Cardiovascular Imaging Asia* **2**(2), 38–48.

- Klauß, M., Stiller, W., Pahn, G., Fritz, F., Kieser, M., Werner, J., Kauczor, H. U. & Grenacher, L. (2013), ‘Dual-energy perfusion-CT of pancreatic adenocarcinoma’, *European Journal of Radiology* **82**(2), 208–214.
- Klotz, E., Haberland, U., Glatting, G., Schoenberg, S. O., Fink, C., Attenberger, U. & Henzler, T. (2015), ‘Technical prerequisites and imaging protocols for CT perfusion imaging in oncology’, *European Journal of Radiology* **84**(12), 2359–2367.
- Koell, M., Klauss, M., Skornitzke, S., Mayer, P., Fritz, F., Stiller, W. & Grenacher, L. (2021), ‘Computed Tomography Perfusion Analysis of Pancreatic Adenocarcinoma using Deconvolution, Maximum Slope, and Patlak Methods - Evaluation of Diagnostic Accuracy and Interchangeability of Cut-Off Values’, *RoFo Fortschritte auf dem Gebiet der Röntgenstrahlen und der Bildgebenden Verfahren* **193**(9), 1062–1073.
- Konstas, A. A., Goldmakher, G. V., Lee, T. Y. & Lev, M. H. (2009a), ‘Theoretic basis and technical implementations of CT perfusion in acute ischemic stroke, part 1: Theoretic basis’, *American Journal of Neuroradiology* **30**(4), 662–668.
- Konstas, A. A., Goldmakher, G. V., Lee, T.-Y. & Lev, M. H. (2009b), ‘Theoretic Basis and Technical Implementations of CT Perfusion in Acute Ischemic Stroke, Part 2: Technical Implementations’, *American Journal of Neuroradiology* **30**(5), 885–892.
- Kovač, J. D., Đurić Stefanović, A., Dugalić, V., Lazić, L., Stanisavljević, D., Galun, D. & Mašulović, D. (2019), ‘CT perfusion and diffusion-weighted MR imaging of pancreatic adenocarcinoma: can we predict tumor grade using functional parameters?’, *Acta Radiologica* **60**(9), 1065–1073.
- Lawrence, K. S. S. & Lee, T.-Y. (1998), ‘An Adiabatic Approximation to the Tissue Homogeneity Model for Water Exchange in the Brain: II. Experimental Validation’, *Journal of Cerebral Blood Flow and Metabolism* **18**(12), 1378–1385.
- Liu, Y. (2018), Research Status and Prospect for CT Imaging, in ‘State of the Art in Nano-bioimaging’, IntechOpen, Rijeka, chapter 5.
- Longnecker, D. S. (2021), ‘Anatomy and Histology of the Pancreas’, *Pancreapedia: Exocrine Pancreas Knowledge Base*.
- Lu, N., Feng, X.-Y., Hao, S.-J., Liang, Z.-H., Jin, C., Qiang, J.-W. & Guo, Q.-Y. (2011), ‘64-slice CT perfusion imaging of pancreatic adenocarcinoma and mass-forming chronic pancreatitis’, *Academic radiology* **18**(1), 81–88.
- Luna, A., Pahwa, S., Bonini, C., Alcalá-Mata, L., Wright, K. L. & Gulani, V. (2016), ‘Multiparametric MR Imaging in Abdominal Malignancies’, *Magnetic resonance imaging clinics of North America* **24**(1), 157–186.

- Manniesing, R., Brune, C., van Ginneken, B. & Prokop, M. (2016), ‘A 4D CT digital phantom of an individual human brain for perfusion analysis’, *PeerJ* **4**, e2683.
- Mathy R. M., Fritz F. , Mayer P., Klauss M., Grenacher L., Stiller W. , Kauczor H.-U., Skornitzke S. (2021), ‘Iodine concentration and tissue attenuation in dual-energy contrast-enhanced CT as a potential quantitative parameter in early detection of local pancreatic carcinoma recurrence after surgical resection’, *European Journal of Radiology* **143**, 109944.
- Mayer, P., Fritz, F., Koell, M., Skornitzke, S., Bergmann, F., Gaida, M. M., Hackert, T., Maier-Hein, K., Laun, F. B., Kauczor, H.-U., Grenacher, L., Klauß, M. & Stiller, W. (2021), ‘Assessment of tissue perfusion of pancreatic cancer as potential imaging biomarker by means of Intravoxel incoherent motion MRI and CT perfusion: correlation with histological microvessel density as ground truth’, *Cancer Imaging* **21**(1), 13.
- McGuigan, A., Kelly, P., Turkington, R. C., Jones, C., Coleman, H. G. & McCain, R. S. (2018), ‘Pancreatic cancer: A review of clinical diagnosis, epidemiology, treatment and outcomes’, *World Journal of Gastroenterology* **24**(43), 4846–4861.
- Medfloss.org (2023), ‘Grassroots DICOM (GDCM)’. [date accessed 01 February 2024].
URL: <https://www.medfloss.org/node/85>
- Miles, K. A. (1991), ‘Measurement of tissue perfusion by dynamic computed tomography’, *The British Journal of Radiology* **64**(761), 409–412.
- Miles, K. A. & Griffiths, M. R. (2003), ‘Perfusion CT: A worthwhile enhancement?’, *British Journal of Radiology* **76**(904), 220–231.
- Miles, K., Lee, T.-Y., Goh, V., Klotz, E., Cuenod, C., Bisdas, S., Groves, A., Hayball, M., Alonzi, R., Brunner, T. et al. (2012), ‘Current status and guidelines for the assessment of tumour vascular support with dynamic contrast-enhanced computed tomography’, *European Radiology* **22**, 1430–1441.
- Mnyusiwalla, A., Aviv, R. I. & Symons, S. P. (2009), ‘Radiation dose from multi-detector row CT imaging for acute stroke’, *Neuroradiology* **51**(10), 635–640.
- Mostafa, M. E., Erbarut-Seven, I., Pehlivanoglu, B. & Adsay, V. (2017), ‘Pathologic classification of “pancreatic cancers”: current concepts and challenges’, *Chinese Clinical Oncology* **6**(6), 59.
- Mottola, M. & Bevilacqua, A. (2021), ‘Reproducibility of Computed Tomography perfusion parameters in hepatic multicentre study in patients with colorectal cancer’, *Biomedical Signal Processing and Control* **64**, 102298.
- Mustra, M., Delac, K. & Grgic, M. (2008), *Overview of the DICOM standard*, Vol. 1, IEEE.

- Nakayama, Y., Awai, K., Funama, Y., Hatemura, M., Imuta, M., Nakaura, T., Ryu, D., Morishita, S., Sultana, S., Sato, N. & Yamashita, Y. (2005), ‘Abdominal CT with low tube voltage: Preliminary observations about radiation dose, contrast enhancement, image quality, and noise’, *Radiology* **237**(3), 945–951.
- National Comprehensive Cancer Network (2023), ‘NCCN Clinical Practice Guidelines in Oncology Pancreatic Adenocarcinoma’. [date accessed 23 Jan 2024].
URL: https://www.nccn.org/guidelines/category_1
- Othman, A., Afat, S., Brockmann, C., Nikoubashman, O., Bier, G., Brockmann, M., Nikolaou, K., Tai, J., Yang, Z., Kim, J. et al. (2017), ‘Low-dose volume-perfusion CT of the brain: effects of radiation dose reduction on performance of perfusion CT algorithms’, *Clinical Neuroradiology* **27**(3), 311–318.
- O’Malley, R. B., Cox, D., Soloff, E. V., Zečević, M., Green, S., Coveler, A., Busey, J. M. & Wang, C. L. (2022), ‘CT perfusion as a potential biomarker for pancreatic ductal adenocarcinoma during routine staging and restaging’, *Abdominal Radiology* **47**(11), 3770–3781.
- Pahn, G., Skornitzke, S., Schlemmer, H.-P., Kauczor, H.-U. & Stiller, W. (2016), ‘Toward standardized quantitative image quality (IQ) assessment in computed tomography (CT): A comprehensive framework for automated and comparative IQ analysis based on ICRU Report 87’, *Physica Medica* **32**(1), 104–115.
- Patel, P. R. & De Jesus, O. (2023), CT Scan, in ‘StatPearls’, StatPearls Publishing, Treasure Island (FL).
URL: <https://www.ncbi.nlm.nih.gov/books/NBK567796/>
- Petralia, G., Bonello, L., Viotti, S., Preda, L., d’Andrea, G. & Bellomi, M. (2010), ‘CT perfusion in oncology: how to do it’, *Cancer Imaging* **10**(1), 8–19.
- Pianykh, O. S. (2012), ‘Digital perfusion phantoms for visual perfusion validation’, *American Journal of Roentgenology* **199**(3), 627–634.
- Puckett, Y. & Garfield, K. (2023), Pancreatic Cancer, in ‘StatPearls’, StatPearls Publishing, Treasure Island (FL).
URL: <https://pubmed.ncbi.nlm.nih.gov/30085538/>
- Sanelli, P. C., Lev, M. H., Eastwood, J. D., Gonzalez, R. G. & Lee, T. Y. (2004), ‘The effect of varying user-selected input parameters on quantitative values in CT perfusion maps’, *Academic Radiology* **11**(10), 1085–1092.
- SAS Institute (2024), ‘SAS® Enterprise Guide® 8.3: User’s Guide’. [date accessed 03 February 2024].
URL: <https://documentation.sas.com/doc/en/egcdc/8.3/egdccc/egug/titlepage.htm>
- Schneeweiß, S., Horger, M., Grözinger, A., Nikolaou, K., Ketelsen, D., Syha, R. & Grözinger, G. (2016), ‘CT-perfusion measurements in pancreatic carcinoma with different kinetic models: Is there a chance for tumour grading based on functional parameters?’, *Cancer Imaging* **16**(1), 1–8.

- Sedgwick, P. (2012), ‘Pearson’s correlation coefficient’, *BMJ* **345**, e4483–e4483.
- Siemens-healthineers (2024), ‘syngo.via - Siemens Healthineers’. [date accessed 01 February 2024].
URL: <https://www.siemens-healthineers.com/medical-imaging-it/advanced-visualization-solutions/syngovia>
- Skornitzke, S. (2016), Dual-energy computed tomography iodine maps of tissue perfusion, PhD thesis, Dissertation, Ruprecht-Karls-Universität Heidelberg, 2017, Heidelberg.
- Skornitzke, S., Fritz, F., Klauss, M., Pahn, G., Hansen, J., Hirsch, J., Grenacher, L., Kauczor, H. U. & Stiller, W. (2015), ‘Qualitative and quantitative evaluation of rigid and deformable motion correction algorithms using dual-energy CT images in view of application to CT perfusion measurements in abdominal organs affected by breathing motion’, *British Journal of Radiology* **88**(1046).
- Skornitzke, S., Fritz, F., Mayer, P., koell, M., hancen, J., Pahn, G., hackert, T., kauczor, H.-U. & Stiller, W. (2018), ‘Dual-energy CT iodine maps as an alternative quantitative imaging biomarker to abdominal CT perfusion: determination of appropriate trigger delays for acquisition using bolus tracking’, *The British Journal of Radiology* **91**(1085), 20170351.
- Skornitzke, S., Hirsch, J., Kauczor, H. U. & Stiller, W. (2019), ‘Evaluation of the effect of image noise on CT perfusion measurements using digital perfusion phantoms’, *European Radiology* **29**(4), 2089–2097.
- Skornitzke, S., Mayer, P., Kauczor, H.-U. & Stiller, W. (2023), ‘Evaluation of optimal acquisition delays of DECT iodine maps in pancreatic adenocarcinoma: A potential alternative to the Patlak model of CT perfusion’, *Heliyon* **9**(4), e14726.
- Skornitzke, S., Vats, N., Mayer, P., Kauczor, H.-U. & Stiller, W. (2023), ‘Pancreatic CT perfusion: quantitative meta-analysis of disease discrimination, protocol development, and effect of CT parameters’, *Insights into Imaging* **14**(1), 132.
- Soloff, E. V., Al-Hawary, M. M., Desser, T. S., Fishman, E. K., Minter, R. M. & Zins, M. (2022), ‘Imaging assessment of pancreatic cancer resectability after neoadjuvant therapy: AJR expert panel narrative review’, *American Journal of Roentgenology* **218**(4), 570–581.
- St Lawrence S., K. S. & Lee, T. Y. (1998), ‘An adiabatic approximation to the tissue homogeneity model for water exchange in the brain: I. Theoretical derivation’, *Journal of Cerebral Blood Flow and Metabolism* **18**(12), 1365–1377.
- Sthle, L. & Wold, S. (1989), ‘Analysis of variance (ANOVA)’, *Chemometrics and Intelligent Laboratory Systems* **6**(4), 259–272.

- Stiller, W., Skornitzke, S., Fritz, F., Klauss, M., Hansen, J., Pahn, G., Grenacher, L. & Kauczor, H. U. (2015), ‘Correlation of Quantitative Dual-Energy Computed Tomography Iodine Maps and Abdominal Computed Tomography Perfusion Measurements: Are Single-Acquisition Dual-Energy Computed Tomography Iodine Maps More Than a Reduced-Dose Surrogate of Conventional Computed Tomography Perfusion?’, *Investigative Radiology* **50**(10), 703–708.
- Taylor, R. (1990), ‘Interpretation of the correlation coefficient: a basic review’, *Journal of diagnostic medical sonography* **6**(1), 35–39.
- Vats, N., Kauczor, H.-U., Stiller, W. & Skornitzke, S. (2021), Development of Perfusion CT and its importance for evaluating pancreatic diseases: a quantitative meta-analysis, in ‘ECR 2021 Book of Abstracts’, Vol. 12 (supp 2), Insights into imaging, p. 75.
- Vats, N., Mayer, P., Kauczor, H.-U., Stiller, W. & Skornitzke, S. (2022), Evaluation and timing optimization of CT perfusion first pass analysis in comparison to maximum slope model in pancreatic carcinoma, in ‘ECR 2022 Book of Abstracts’, Vol. 13 (supp 4), Insights into imaging, p. 205.
- Vats, N., Mayer, P., Kauczor, H.-U., Stiller, W. & Skornitzke, S. (2024), Model-based noise correction of CT perfusion blood flow measurements based on digital perfusion phantoms, in ‘ECR 2024 Book of Abstracts’, Vol. 15, Insights into imaging. (Proceedings under publication).
- Vats, N., Mayer, P., Kortes, F., Klauß, M., Grenacher, L., Stiller, W., Kauczor, H.-U. & Skornitzke, S. (2023), ‘Evaluation and timing optimization of CT perfusion first pass analysis in comparison to maximum slope model in pancreatic adenocarcinoma’, *Scientific Reports* **13**(1), 10595.
- Vendiš, T. (2022), ‘CT scan’. [date assessed 14 February 2022].
URL: https://en.wikipedia.org/wiki/CT_scan
- Wang, S., Zheng, Y., Yang, F., Zhu, L., Zhu, X.-Q., Wang, Z.-F., Wu, X.-L., Zhou, C.-H., Yan, J.-Y., Hu, B.-Y., Kong, B., Fu, D.-L., Bruns, C., Zhao, Y., Qin, L.-X. & Dong, Q.-Z. (2021), ‘The molecular biology of pancreatic adenocarcinoma: translational challenges and clinical perspectives’, *Signal Transduction and Targeted Therapy* **6**(1), 1–23.
- Wikipedia contributors (2023a), ‘Dicom - Wikipedia, the free encyclopedia’. [date assessed 01 Feb 2024].
URL: <https://en.wikipedia.org/wiki/DICOM>
- Wikipedia, Contributors (2023b), ‘GDCM-Wikipedia, The Free Encyclopedia’. [date accessed 01 February 2024].
URL: <https://en.wikipedia.org/wiki/GDCM>
- Wintermark, M., Smith, W. S., Ko, N. U., Quist, M., Schnyder, P. & Dillon, W. P. (2004), ‘Dynamic perfusion CT: optimizing the temporal resolution and contrast

- volume for calculation of perfusion CT parameters in stroke patients', *American journal of neuroradiology* **25**(5), 720–729.
- Xie, Q., Wu, J., Tang, Y., Dou, Y., Hao, S., Xu, F., Feng, X. & Liang, Z. (2013), 'Whole-organ CT perfusion of the pancreas: Impact of iterative reconstruction on image quality, perfusion parameters and radiation dose in 256-slice CT-preliminary findings', *PLoS ONE* **8**(11), e80468.
- Xu, J., Liang, Z., Hao, S., Zhu, L., Ashish, M., Jin, C., Fu, D. & Ni, Q. (2009), 'Pancreatic adenocarcinoma: dynamic 64-slice helical CT with perfusion imaging', *Abdominal Imaging* **34**(6), 759–766.
- Yang, Y., Shi, J. & Zhu, J. (2021), 'Diagnostic performance of noninvasive imaging modalities for localization of insulinoma: A meta-analysis', *European Journal of Radiology* **145**, 110016.
- Yu, L., Leng, S., Phillips, L. J., Banghart, D. & McCollough, C. H. (2018), Dose considerations in ct perfusion, Radiology Key. [date assessed 02 Nov 2023].
URL: <https://radiologykey.com/dose-considerations-in-ct-perfusion/>
- Zhao, Y., Hubbard, L., Malkasian, S., Abbona, P. & Molloy, S. (2020), 'Dynamic pulmonary CT perfusion using first-pass analysis technique with only two volume scans: Validation in a swine model', *PLoS ONE* **15**(2), e0228110.
- Zhao, Z. Y. & Liu, W. (2020), 'Pancreatic Cancer: A Review of Risk Factors, Diagnosis, and Treatment', *Technology in Cancer Research & Treatment* **19**, 1533033820962117.
- Zhu, L., Xue, H.-d., Sun, H., Wang, X., He, Y.-l., Jin, Z.-y. & Zhao, Y.-p. (2016), 'Isoattenuating insulinomas at biphasic contrast-enhanced CT: frequency, clinicopathologic features and perfusion characteristics', *European Radiology* **26**(10), 3697–3705.
- Zhu, L., Xue, H., Sun, Z., Li, P., Qian, T., Xing, X., Li, N., Zhao, Y., Wu, W. & Jin, Z. (2017), 'Prospective comparison of biphasic contrast-enhanced CT, volume perfusion CT, and 3 Tesla MRI with diffusion-weighted imaging for insulinoma detection', *Journal of Magnetic Resonance Imaging* **46**(6), 1648–1655.
- Zierler, K. L. (1962), 'Theoretical Basis of Indicator-Dilution Methods For Measuring Flow and Volume', *Circulation Research* **10**, 393–407.
- Zussman, B., Jabbour, P., Talekar, K., Gorniak, R. & Flanders, A. E. (2011), 'Sources of variability in computed tomography perfusion: implications for acute stroke management', *Neurosurgical Focus* **30**(6), E8.

*Science is a celebration of human curiosity, ingenuity,
and creativity, and its achievements are a testament
to the limitless potential of the human mind.*

Mae Jemison

8

Personal publications

This chapter outlines the author's contributions to the scientific community, categorizing them into first authorship and co-authorship contributions in international peer-reviewed journals, as well as first authorships and co-authorship conference contributions. These contributions demonstrate the active participation of the author and significant impact within their field of study. Research papers for meta-analysis were jointly compiled by the author and Dr. Stephan Skornitzke, a postdoctoral candidate. Experienced radiologists acquired the clinical data and marked the ROIs. However, study design, data evaluation, phantom simulations, execution, implementation, formal and statistical analysis, data evaluation, and phantom simulations were performed primarily by the author of this dissertation.

8.1 First authorship peer-reviewed journal contributions

1. **Vats N**, Mayer P, Kortess F, Klauß M, Grenacher L, Stiller W, Kauczor H-U, Skornitzke S (2023), 'Evaluation and timing optimization of CT perfusion first pass analysis in comparison to maximum slope model in pancreatic adenocarcinoma', Scientific Reports 13(1), 10595.
2. Skornitzke S¹, **Vats N**¹, Mayer P, Kauczor H-U and Stiller W (2023), 'Pancreatic CT perfusion: quantitative meta-analysis of disease discrimination, protocol development, and effect of CT parameters', Insights into imaging 14(1), 132.

Stephan Skornitzke and Neha Vats have contributed equally to this publication.

Personal publications

3. **Vats N**, Sengupta A, Gupta R K, Patir R, Vaishya S, Ahlawat S, Saini J, Agarwal S, Singh A (2023), 'Differentiation of Pilocytic Astrocytoma from Glioblastoma using a Machine-Learning framework based upon quantitative T1 perfusion MRI', Magn Reson Imaging. 98(76-82).

Publication 1 is based on the results of Section 3.3 and their discussion in Section 4.3 of this dissertation. My personal contribution to this publication involved methodology development, software implementation, conducting formal and statistical analyses, validating the findings, and preparing the manuscript for publication.

Publication 2 is based on the results of Section 3.1 and their discussion in Section 4.1 of this dissertation. My personal contribution to this publication consisted of data collection and interpretation, methodology, formal analysis, statistical analysis, validation, and the preparation of the manuscript.

Publication 3 - My personal contribution to this publication consisted of data collection, methodology, formal analysis, statistical analysis, software implementation, validation, and the preparation of the manuscript.

8.2 Co-authorship peer-reviewed journal contributions

1. Skornitzke S, **Vats N**, Kopytova T, Tong E, Hofbauer T, Weber T, Rehnitz C, von Stackelberg O, Maier-Hein K, Stiller W, Biederer J, Kauczor H-U, Heußel C-P, Wielpütz M and Palm V (2022), 'Asynchronous calibration of quantitative computed tomography bone mineral density assessment for opportunistic osteoporosis screening: phantom-based validation and parameter influence evaluation', Scientific Reports 12, 20729.

My personal contribution to this publication consisted of calculating the bone mineral densities and evaluating the datasets.

8.3 Manuscript under preparation

1. **Vats N**, Mayer P, Klauß M, Kauczor H-U, Stiller W, Skornitzke S, "Model-based noise correction of CT perfusion blood flow measurements based on digital perfusion phantoms"

8.4 First and co-authorship conference contributions and proceedings

1. **Vats N**, Mayer P, Klauß M, Kauczor H-U, Stiller W, Skornitzke S, "Model-based noise correction of CT perfusion blood flow measurements based on

digital perfusion phantoms", ECR 2024 book of abstracts. Insights Imaging 15. (Proceedings under publication)

2. **Vats N**, Mayer P, Kauczor H-U, Stiller W, Skornitzke S, "Evaluation and timing optimization of CT perfusion first pass analysis in comparison to maximum slope model in pancreatic carcinoma", ECR 2022 Book of Abstracts. Insights Imaging 13 (Suppl 4), 205 (2022).
<https://doi.org/10.1186/s13244-022-01337-x>
3. Skornitzke S, **Vats N**, Mayer P, Kauczor H-U, Stiller W, "Optimising CT perfusion acquisition parameters based on digital perfusion phantoms: obtaining maximum precision for a specific radiation exposure setting", ECR 2022 Book of Abstracts. Insights Imaging 13 (Suppl 4), 205 (2022).
<https://doi.org/10.1186/s13244-022-01337-x>
4. **Vats N**, Kauczor H-U, Stiller W, Skornitzke S, "Development of Perfusion CT and its importance for evaluating pancreatic diseases: a quantitative meta-analysis", ECR 2021 Book of Abstracts. Insights Imaging 12 (Suppl 2), 75 (2021).
<https://doi.org/10.1186/s13244-021-01014-5>
5. **Vats N**, Yadav V K, Awasthi M, Sasi D, Gupta M, Gupta R K, Singh A, "Segmentation of Contrast Enhancing Brain Tumor Region using a Machine Learning Framework based upon Pre and Post contrast MR Images", in 'Proc. Intl. Soc. Mag. Reson. Med.', Vol. 28, ISMRM 2020.
<https://archive.ismrm.org/2020/3554.html>
6. Singh A, **Vats N**, Yadav, V K, Sengupta V, Gupta R K, Gupta M, Patir R, Ahlawat S, Saini J (2020), "On Differentiation of Pilocytic Astrocytoma from High-Grade-Glioma Tumor using Machine Learning Based upon Quantitative T1 Perfusion MRI", in 'Proc. Intl. Soc. Mag. Reson. Med.', Vol. 28, ISMRM 2020.
<https://archive.ismrm.org/2020/1893.html>
7. Yadav V K, **Vats N**, Awasthi M, Sasi D, Gupta M, Gupta, R K, Agarwal S, Singh A (2020), "Segmenting Brain Tumor Lesion from 3D FLAIR MR Images using Support Vector Machine approach", in 'Proc. Intl. Soc. Mag. Reson. Med.', Vol. 28, ISMRM 2020.
<https://archive.ismrm.org/2020/3517.html>
8. Awasthi M, Kar B, **Vats N**, Yadav V K, Sasi D, Gupta M, Gupta R K, Agarwal S, Singh, A (2020), "Method for Automatic blood vessel removal from quantitative T1-perfusion MRI maps and evaluating its impact on tumor grading", in 'Proc. Intl. Soc. Mag. Reson. Med.', Vol. 28, ISMRM 2020.
<https://archive.ismrm.org/2020/3804.html>
9. Debnath A, Awasthi M, **Vats N**, Gupta R K, Singh A (2020), "Differentiation between Intra-Cranial Mass Lesions using Machine Learning approach on

Personal publications

- Amide Proton Transfer-weighted (APT-w) CEST MRI”, in ‘Proc. Intl. Soc. Mag. Reson. Med.’, Vol. 28, ISMRM 2020.
<https://archive.ismrm.org/2020/3106.html>
10. Parvaze S P, Gupta M, Singh A, Patir R, Ahlawat S, Ingahalikar M, **Vats N**, Gupta R K (2020), “Identifying texture features that may serve as biomarkers of various subgroups of glioblastoma segmented using T1-perfusion MRI”, in ‘Proc. Intl. Soc. Mag. Reson. Med.’, Vol. 28, ISMRM 2020.
<https://archive.ismrm.org/2020/1914.html>
 11. Gupta M, Gupta A, Saini J, Patir R, Ahlawat S, Santosh V, **Vats N**, Awasthi M, Parvaze S, Gupta R K (2020), “Comparative evaluation of Oligodendroglioma and Astrocytoma subtypes with similar grade using Conventional MRI and T1 perfusion MRI imaging”, in ‘Proc. Intl. Soc. Mag. Reson. Med.’, Vol. 28, ISMRM 2020.
<https://archive.ismrm.org/2020/1708.html>
 12. **Vats N**, Sengupta A, Sasi D, Gupta R K, Chauhan R P, Yadav V K, Agarwal S, & Singh A. “Comparing supervised and unsupervised machine learning frameworks based upon quantitative-MRI features in differentiation between non-enhancing tumor and vasogenic edema of glioma patients and validation using histopathological ground-truth”, ISMRM 2019, Proc. Intl. Soc. Mag. Reson. Med. 27 (2019).
<https://archive.ismrm.org/2019/3072.html>
 13. Sengupta A, **Vats N**, Agarwal S, Gupta R K, Sasi D, Debnath A, & Singh A., “Differentiation of Non-enhancing tumor region from Vasogenic edema in High grade glioma using a machine learning framework based upon conventional MRI feature”, ISMRM 2019, Proc. Intl. Soc. Mag. Reson. Med. 27 (2019).
<https://archive.ismrm.org/2019/3070.html>
 14. Kar B, Sengupta A, Bhattacharjee R, **Vats N**, Yadav V, Sasi D, Gupta R K, Singh A, “Grading of glioma using a machine learning framework based on optimized features obtained from quantitative DCE-MRI and SWI”, ISMRM 2019, Proc. Intl. Soc. Mag. Reson. Med. 27 (2019).
<https://archive.ismrm.org/2019/3071.html>
 15. Thaha R, Jogi S, Rajan S, Mahajan V, Venugopal V K, Mehndiratta A, Singh A, Singh D, **Vats N**, “Automated femoro-tibial cartilage segmentation of OA patients with and without bone abnormality”, ISMRM 2019, Proc. Intl. Soc. Mag. Reson. Med. 27 (2019).
<https://archive.ismrm.org/2019/4719.html>
 16. **Vats N**, Yadav V K, Sengupta A, Gupta RK, Chauhan R P, and Singh A. “Validating the utility of unsupervised machine learning in segmenting different parts of glioma with respect to histopathological ground truth”, Conference on Magnetic Resonance in Medicine & 25th NMRS Meeting (2019), Department of NMR, AIIMS, New Delhi, India.

8.4. First and co-authorship conference contributions and proceedings

17. **Vats N**, Chauhan R P, Singh A, “Validating the utility of unsupervised machine learning in segmenting different parts of glioma with respect to histopathological ground truth”, 7th National Conference on Nano science and Instrumentation Technology (NCNIT-2019), Department of Physics, NIT Kurukshetra, Haryana, India. (**Best presentation award**)

The more I learn, the more I realize how much I don't know.

Isaac Newton



In this thesis, all the image data used were present in the DICOM format. Additionally, digital perfusion phantom images were meticulously generated and stored in DICOM format. Consequently, in this chapter, a brief overview of the DICOM format has been provided to provide an understanding of its significance in medical imaging.

DICOM stands for Digital Imaging and Communications in Medicine (Mustra et al. 2008, Gibaud 2008). It is a standard protocol used in the medical imaging community for handling, storing, printing, retrieving, and transmitting of medical images. This protocol was developed by the National Electrical Manufacturers Association (NEMA) and the American College of Radiology (ACR). It ensures compatibility between various medical imaging devices and information systems.

DICOM defines a set of rules and standards for the formatting and communication of medical imaging data and related information. It encompasses not only the image data itself but also patient information, acquisition parameters, annotations, and other metadata essential for the interpretation and management of medical images.

DICOM files, typically stored in a format with the ".dcm" extension, contain both image pixel data and accompanying metadata encapsulated in a standardized structure as represented by Figure A.1. This structure enables DICOM files to be easily interpreted and exchanged between different imaging devices and healthcare information systems.

DICOM allows for the integration of various imaging modalities such as X-ray, CT, MRI, ultrasound, etc. This interoperability facilitates seamless communication and collaboration between healthcare professionals, regardless of the specific

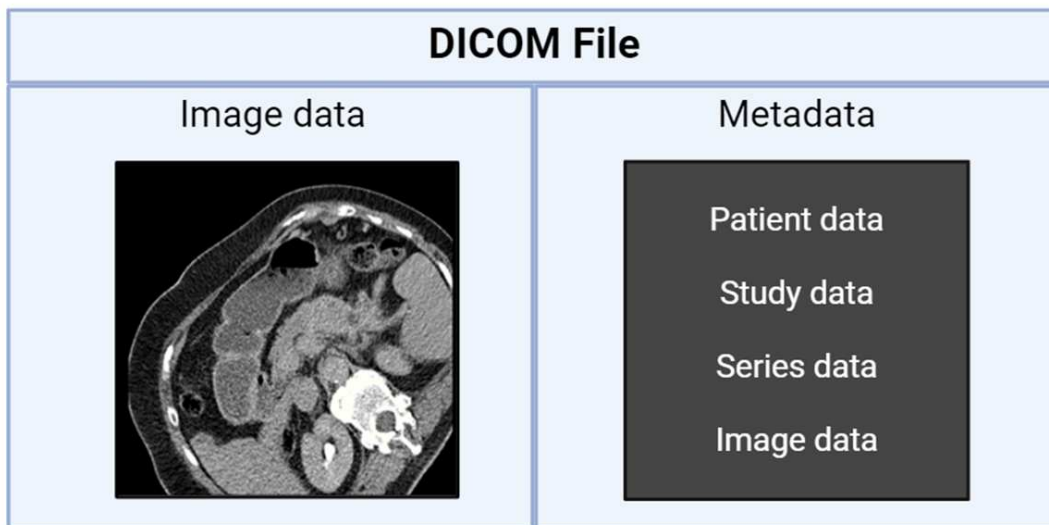


Figure A.1: DICOM file representation consisting of image data and metadata

imaging equipment or software they use.

DICOM also supports the implementation of Picture Archiving and Communication Systems (PACS), which enable healthcare providers to store, retrieve, and distribute medical images and associated information electronically. PACS streamline the workflow of medical imaging departments, improve accessibility to images for diagnosis and treatment planning, and facilitate remote consultation and telemedicine.

Furthermore, DICOM standards continue to evolve to accommodate advancements in medical imaging technology and address emerging healthcare needs. This ongoing development ensures that DICOM remains a vital component of modern healthcare infrastructure, supporting the delivery of high-quality patient care through efficient and interoperable medical imaging solutions.

The best way to predict the future is to create it.
Peter Drucker

B

Softwares

In this thesis, a variety of software tools were used for different aspects of data processing and analysis. These software tools will be briefly discussed in the following chapter. First, the software "Syngo.via" used for post-processing CT image data and for the computation of blood perfusion maps will be elaborated in Section B.1. Subsequently, the in-house developed software "SOPHIA" and external software libraries will be discussed in Section B.2. The FPA model developed in this thesis was developed based on SOPHIA software and these external libraries, using C++.

B.1 Syngo.via

Syngo.via is a software platform developed by Siemens Healthineers (Siemens-healthineers 2024), mainly designed for advanced visualization and post-processing of medical imaging data. It helps to interpret, analyze, and manipulate various types of medical images, including CT, MRI, PET, X-ray, and more.

Key features and functionalities of Syngo.via software include:

1. **Advanced Visualization:** Syngo.via offers advanced visualization tools that allow one to interactively explore and manipulate medical images in three-dimensional (3D) and four-dimensional (4D) spaces. This enables better visualization of anatomical structures, pathology, and complex relationships within the body.
2. **Post-processing Tools:** Syngo.via provides a wide range of post-processing tools and techniques for image enhancement, segmentation, and registration. These tools help improve image quality, delineate structures, and facilitate quantitative analysis for diagnostic and research purposes.

3. Clinical Applications: Syngo.via offers specialized applications, tools, and algorithms for specific imaging modalities. These include cardiovascular imaging, oncology, neurology, orthopedics, and more.
4. Automation and Workflow Optimization: Syngo.via includes automated image processing algorithms, predefined protocols, and customizable workflows that help increase efficiency and productivity.
5. Integration and Collaboration: Syngo.via is designed to integrate seamlessly with other imaging systems, such as PACS.

In general, Syngo.via serves as a powerful tool for medical image interpretation, analysis, and clinical decision making, empowering healthcare professionals with advanced visualization capabilities and workflow efficiencies to improve patient care.

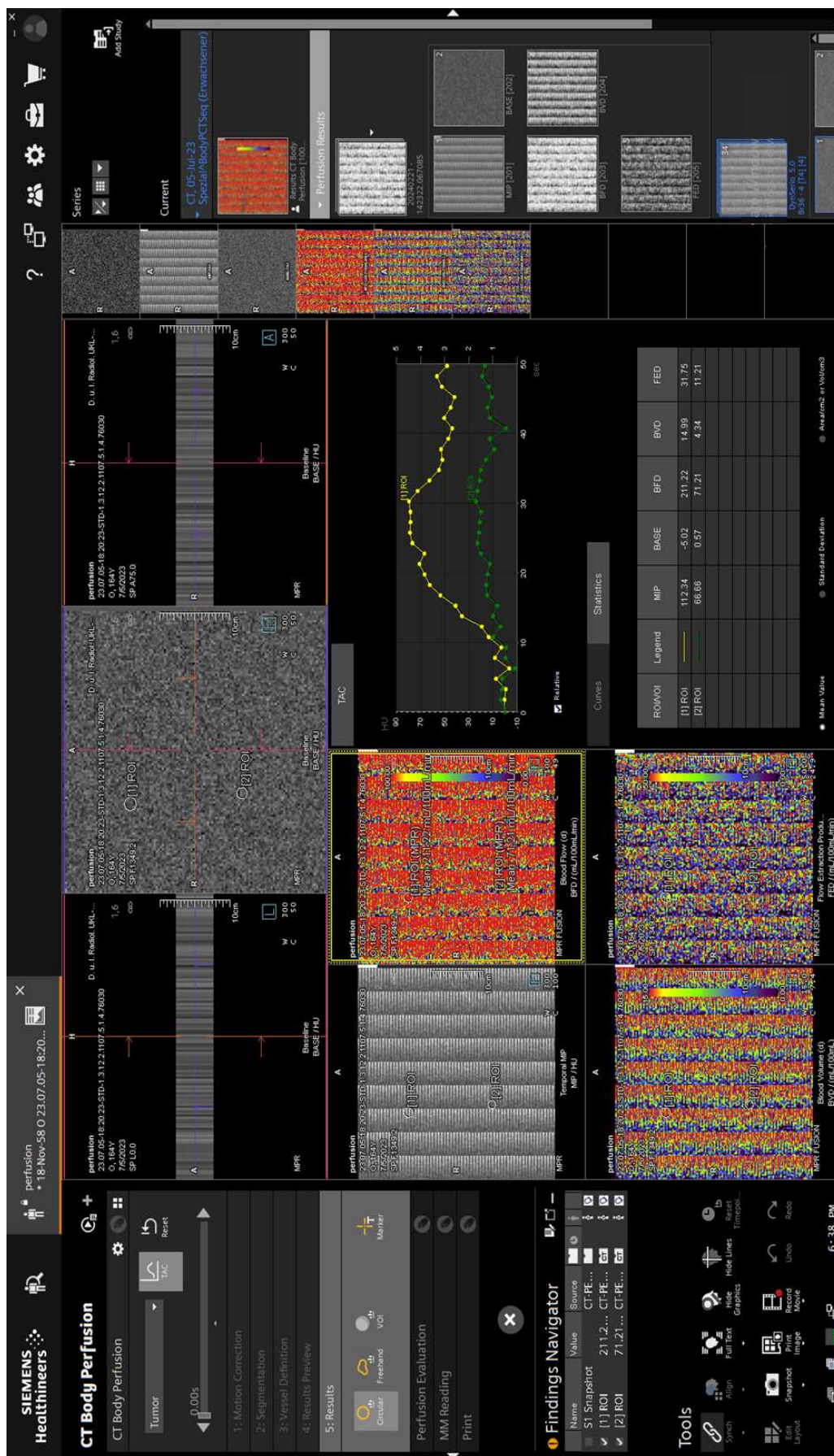
In this thesis, the syngo.via software tool was used to calculate the BF perfusion maps using the CT perfusion deconvolution model. The perfusion maps were computed to develop the noise correction algorithm using digital perfusion phantoms. Subsequently, syngo.via and the developed noise-correction algorithm were used to validate the algorithm with the clinical dataset. A screenshot of the syngo.via software is shown in Figure B.1.

B.2 SOPHIA

SOPHIA (Software for physics and image analysis) is an in-house software tool developed by Gregor Pahn, particularly focused on physics and image quality analysis in a standardized manner (Pahn et al. 2016).

The key features and functionalities of the SOPHIA software include:

1. Image Processing and Analysis: It provides tools for processing and analyzing images in the DICOM format. This includes functions such as image enhancement, segmentation, ROI selection, image registration, calculation of perfusion maps, and quantitative analysis.
2. Automated Image Quality Analysis: SOPHIA offers automated algorithms and analysis for the quantitative assessment of various aspects of image quality in CT scans. This could include metrics such as spatial resolution, noise characteristics, contrast-to-noise ratio, and other relevant parameters.
3. Integration with External Libraries: SOPHIA can be integrated with external software libraries such as GDCM B.2.1, ROOT B.2.2, and ITK B.2.3 to leverage additional functionalities or perform specific analyses.
4. Programming language: SOPHIA is implemented using C++ to provide flexibility and customization options.



119
Figure B.1: Screenshot of the syngo.via software showing perfusion maps generated from the digital perfusion phantom

Softwares

Overall, SOPHIA provides tools and functionalities such as image analysis, data processing, and quantitative analysis. The figures displaying screenshots from SOPHIA software, depicting SOPHIA Viewer and SOPHIA Perfusion, are presented in Figure B.2 and Figure B.3, respectively.

B.2.1 Grassroots DICOM (GDCM)

The GDCM library is an open source software toolkit developed for handling and manipulating DICOM files in medical imaging applications (Medfloss.org 2023, Wikipedia, Contributors 2023b). GDCM provides a comprehensive set of functionalities for reading, writing, modifying DICOM meta-data, and processing DICOM files, making it a valuable tool for medical imaging data.

Here are some key features and aspects of the GDCM library:

1. **DICOM File Handling:** GDCM offers robust support for reading and writing DICOM files in various formats and transfer syntaxes.
2. **Data Extraction and Manipulation:** The library allows users to extract meta-data and image pixel data from DICOM files, enabling access to information such as patient demographics, acquisition parameters, and image characteristics. It also provides utilities for modifying DICOM headers and pixel data, facilitating data preprocessing and manipulation tasks.
3. **Image Visualization:** GDCM includes tools for visualizing DICOM images, enabling users to display medical images in standard image viewers.
4. **Compatibility and Interoperability:** GDCM is designed to be highly compatible with the DICOM standard and thus provides integration between different imaging devices and softwares.
5. **Cross-Platform Support:** GDCM can be used on various operating systems, including Windows, macOS, and Linux.

B.2.2 ROOT

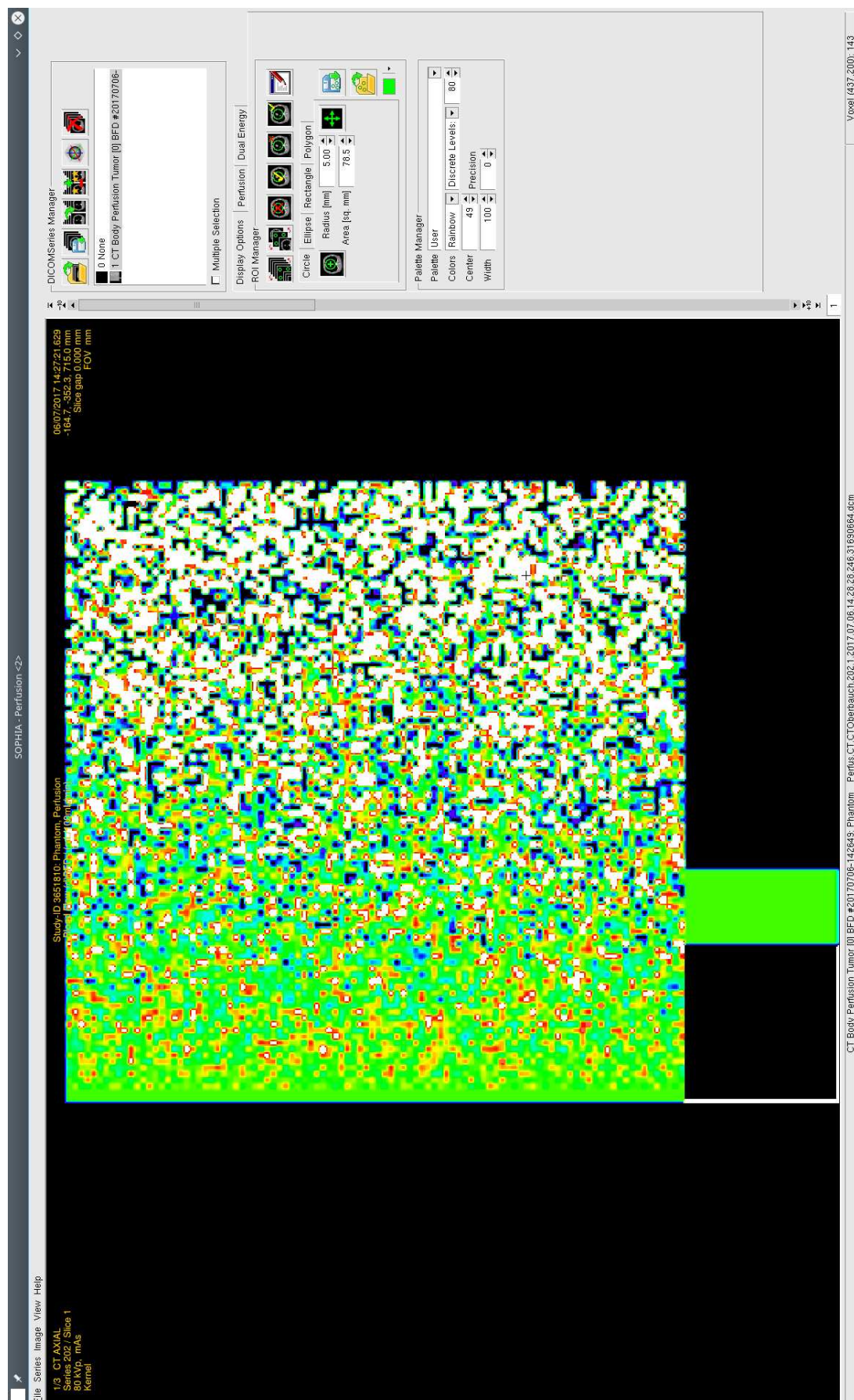
ROOT is an open-source data analysis framework, developed by CERN, the European Organization for Nuclear Research (D. Piparo 2024). ROOT provides a comprehensive set of tools for data storage, manipulation, analysis, and visualization.

Here are some key aspects and features of ROOT:

1. **Data Storage:** ROOT provides a hierarchical data storage model, allowing users to organize data into directories and files similar to a filesystem.



Figure B.2: Screenshot of SOPHIA Viewer software showing a CT image from the dynamic CT series of upper abdomen



2. **Data Analysis:** ROOT offers a wide range of tools and libraries to perform data analysis tasks, including statistical analysis, curve fitting, multidimensional histogramming, and mathematical operations. It provides a C++ interpreter that allows one to interactively execute commands and write scripts for data analysis.
3. **Visualization:** ROOT includes a powerful visualization framework to create 2D and 3D plots, histograms, graphs, and interactive graphical applications.
4. **Mathematics and Statistics:** ROOT incorporates libraries for mathematical and statistical calculations, including functions for linear algebra, probability distributions, random number generation, and numerical optimization.
5. **Parallel Processing:** ROOT supports parallel processing techniques that enable faster analysis of large datasets by distributing computation across multiple processing units.
6. **Integration with Other Tools:** ROOT can be integrated with other scientific computing tools and libraries, such as Python, NumPy, SciPy, and TensorFlow.

B.2.3 Insight Segmentation and Registration Toolkit (ITK)

ITK, known as the Insight Segmentation and Registration Toolkit (Johnson et al. 2021), is an open-source software library extensively used for image analysis and processing in medical imaging. ITK offers a comprehensive suite of tools and algorithms to address various image processing tasks, including segmentation, registration, filtering, and visualization of medical image data.

Here are some key aspects and features of ITK:

1. **Data Representation:** ITK employs a versatile data model capable of representing diverse types of data, such as structured grids, unstructured grids, polygonal meshes, image data, and point clouds.
2. **Algorithmic Diversity:** ITK provides a wide array of image processing algorithms, implemented in C++, covering functionalities like intensity-based registration, segmentation and deformable models, edge detection, feature extraction, and image filtering.
3. **Modularity:** ITK's modular design enables easy extension and customization, allowing users to integrate custom algorithms or develop new modules tailored to specific applications.
4. **Multi-Language Support:** ITK's functionality is accessible from various programming languages, including Python, through bindings, facilitating integration with existing software systems and workflows.

Softwares

5. Cross-Platform Compatibility: ITK is designed to work seamlessly across different operating systems, including Windows, macOS, and Linux, ensuring broad accessibility and compatibility.

In this thesis, SOPHIA GUI was used for image registration using an already developed algorithm. Furthermore, the CT perfusion FPA model was developed and implemented based on SOPHIA software and these external libraries. Subsequently, the FPA perfusion maps were computed and evaluated using SOPHIA GUI. Furthermore, SOPHIA was used to validate the FPA model by computing MSM perfusion maps using an already implemented MSM model.

The universe is under no obligation to make sense to you.

Neil deGrasse Tyson

C

Statistics

In this thesis, various statistical analysis methods have been used for the interpretation and analysis of data. Therefore, this chapter aims to elaborate these statistical methods in depth. Firstly, the chapter begins by explaining the student's t-test in Section C.1. Subsequently, the statistical techniques ANOVA and ANCOVA will be thoroughly discussed in the following Sections C.2 and C.3, respectively. Following this, the chapter will delve into the intricacies of linear regression analysis in Section C.4. Furthermore, a detailed explanation of box plot analysis will be presented in Section C.5. Subsequently, the concept of CNR will be explained in Section C.6. Moreover, the aspects of model error and random errors will be addressed in subsequent sections C.7 and C.8 respectively. Moving forward, a thorough examination of Bland-Altman analysis will be discussed in the Section C.9. Subsequently, the correlation method used in this thesis will be discussed in Section C.10, followed by a comprehensive discussion on COV in Section C.11. Finally, the chapter will conclude with a brief overview of the SAS software in Section C.12.

C.1 Student's t-test

The Student's t-test or simply the t-test is a statistical hypothesis test used to determine if there is a significant difference between the means of two groups. It was developed by William Sealy Gosset, who published under the pseudonym "Student" in 1908 (Kalpić et al. 2011).

There are some variations of the t-test:

1. Independent Samples t-test: This type of t-test is used when the samples from the two groups being compared are independent of each other.

2. Paired or dependent Samples t-test: This test is used when the samples in the two groups are related or matched in some way.

The general procedure for conducting a t-test involves the following steps:

1. Formulate Hypotheses: Define the null hypothesis (H0) and alternative hypothesis (H1). The null hypothesis typically states that there is no significant difference between the means of the two groups, while the alternative hypothesis states that there is a significant difference.
2. Calculate the Test Statistic: Compute the t-statistic using the formula appropriate for the type of t-test being conducted.

For the independent samples t-test, the formula is:

$$t = \frac{\bar{x}_1 - \bar{x}_2}{\sqrt{\frac{s_1^2}{n_1} + \frac{s_2^2}{n_2}}} \quad (\text{C.1})$$

Where:

- \bar{x}_1 and \bar{x}_2 are the sample means of the two groups.
- s_1^2 and s_2^2 are the sample variances of the two groups.
- n_1 and n_2 are the sample sizes of the two groups.

The formula for the paired t-test is:

$$t = \frac{\bar{x}_D}{\frac{s_D}{\sqrt{n}}} \quad (\text{C.2})$$

Where:

- \bar{x}_D is the mean of the differences between the paired observations.
 - s_D is the standard deviation of the differences.
 - n is the sample size.
3. Determine the Degrees of Freedom (df): For an independent samples t-test, df is calculated as $df = n_1 + n_2 - 2$ and for a paired t-test it is equal to $df = n - 1$.
 4. Calculate the p-value: Calculate the p-value of the t-distribution based on the desired significance level (typically 0.05 or 0.01) and the degrees of freedom. The p-value is the area under the t-distribution curve.
 5. Interpret the p-Value: If the p-value is less than or equal to the significance level, then reject the null hypothesis and conclude that there is a significant difference between the means of the two groups. Otherwise, fail to reject the null hypothesis.

The t-test is a valuable tool for comparing means and determining whether observed differences are statistically significant. However, it is essential to ensure that the assumptions of the t-test are met, including normality of the data and homogeneity of variances, to obtain valid results.

C.2 ANOVA

ANOVA, or Analysis of Variance, is a statistical method used to compare the means of three or more groups simultaneously (Sthle & Wold 1989). ANOVA assesses whether there are statistically significant differences between the means of the groups and helps identify which groups are significantly different from each other.

There are several types of ANOVA statistical method:

1. One-Way ANOVA: One-Way ANOVA is used when there is only one independent variable (factor) with three or more groups. It tests whether there are significant differences in the means of the groups.
2. Two-Way ANOVA: Two-Way ANOVA is used when there are two independent variables (factors) with multiple groups. It assesses the main effects of each variable, as well as any interactions between the variables.

The general procedure for conducting an ANOVA involves the following steps:

1. Formulate Hypotheses: Define the null hypothesis (H_0) and alternative hypothesis (H_1). The null hypothesis typically states that there are no significant differences between the means of the groups or conditions, while the alternative hypothesis states that at least one group mean is significantly different from the others.
2. Calculate the Test Statistic: Compute the F-statistic, which is the ratio of the variance between groups to the variance within groups. The formula for the F-statistic is:

$$F = \frac{\text{Between-group variability}}{\text{Within-group variability}} \quad (\text{C.3})$$

3. Determine the Degrees of Freedom: Calculate the degrees of freedom for the between-group and within-group variability.
4. Calculate the p-value: Determine the p-value of the F-distribution based on the desired significance level (typically 0.05) and the degrees of freedom.
5. Interpret the p-Value: If the p-value is less than or equal to the significance level, then reject the null hypothesis and conclude that there is a significant difference between the means of the two groups. Otherwise, fail to reject the null hypothesis.

6. **Post-Hoc Tests (optional):** If the ANOVA results are significant, post-hoc tests such as Tukey's HSD, Bonferroni, or LSD tests can be conducted to determine which specific group means differ significantly from each other.

ANOVA provides a powerful and efficient way to analyze data and comparing means within multiple groups. However, it's essential to ensure that the assumptions of ANOVA are met, including normality of data, homogeneity of variances, and independence of observations, to obtain valid results.

ANOVA consists of two variant methods that are used to analyze data with additional complexities:

1. **Weighted ANOVA:** Weighted ANOVA is used when each observation in the dataset has a different weight or importance. This weighting factor reflects the relative importance or precision of each observation in the analysis. Weighted ANOVA adjusts for these weights when calculating the variance and test statistics, giving more weight to observations that are considered more reliable or informative.

The weighted ANOVA test statistic is typically calculated similarly to the traditional ANOVA, but each observation is multiplied by its corresponding weight before the calculations. The degrees of freedom and critical values are adjusted accordingly to account for the weighted data.

Weighted ANOVA is particularly useful in situations where some observations are more precise or have higher reliability than others, and it allows incorporating this information into the analysis effectively.

2. **Factorial ANOVA:** Factorial ANOVA is an extension of the traditional ANOVA method that allows for the simultaneous analysis of two or more categorical independent variables. It assesses not only the main effects of each variable but also the interaction effects between these variables.

C.3 ANCOVA

ANCOVA, or Analysis of Covariance is a statistical method used to analyze one or more categorical independent variables and one continuous independent variable (covariate). The covariate is a variable that is related to the dependent variable and may potentially influence the outcome of the analysis. ANCOVA adjusts for the effects of the covariate(s) by incorporating them into the analysis as additional predictors (Khammar et al. 2020).

The primary goal of ANCOVA is to assess whether there are significant differences in the means of the dependent variable across the levels of the categorical

independent variable(s) after accounting for the effects of the covariate(s). It does this by testing the main effects of the categorical independent variable(s) and the covariate(s) on the dependent variable, as well as any interaction effects between them.

Like weighted ANOVA, a variant method of ANCOVA is weighted ANCOVA which is used when the observations in the dataset have different weights or importance. Weighted ANCOVA adjusts for these weights when estimating the model parameters and test statistics, giving more weight to observations that are considered more reliable or informative.

C.4 Linear regression analysis

Linear regression analysis is a statistical method used to model the relationship between a dependent variable (response variable) and one or more independent variables (predictor variables) by fitting a linear equation to the observed data. The goal of linear regression is to estimate the coefficients of the linear equation that best describe the relationship between the variables and to make predictions based on the model.

There are two main types of linear regressions:

1. Simple Linear Regression: Simple linear regression involves modeling the relationship between one independent variable (X) and one dependent variable (Y) using a linear equation of the form:

$$Y = \beta_0 + \beta_1 X + \epsilon \quad (\text{C.4})$$

Where:

- Y is the dependent variable.
- X is the independent variable.
- β_0 is the intercept (the value of Y when $X = 0$).
- β_1 is the slope (the change in Y for a one-unit change in X).
- ϵ is the error term (residuals), representing the difference between the observed and predicted values of Y .

Simple linear regression aims to find the best-fitting line (regression line) that minimizes the sum of squared differences between the observed and predicted values of Y .

2. Multiple Linear Regression: Multiple linear regression involves modeling the relationship between one dependent variable (Y) and two or more independent variables (X_1, X_2, \dots, X_n) using a linear equation of the form:

$$Y = \beta_0 + \beta_1 X_1 + \beta_2 X_2 + \dots + \beta_n X_n + \epsilon \quad (\text{C.5})$$

Where:

- Y is the dependent variable.
- X_1, X_2, \dots, X_n are the independent variables.
- β_0 is the intercept.
- $\beta_1, \beta_2, \dots, \beta_n$ are the coefficients (slopes) associated with each independent variable.
- ϵ is the error term.

Multiple linear regression aims to estimate the coefficients (slopes) that best describe the linear relationship between the dependent variable and multiple independent variables while accounting for the potential influence of each variable on the dependent variable.

C.5 Box-and-whisker plots

Box-and-whisker plots, also known as boxplots, are a graphical representation of the distribution of a dataset, summarizing the key features such as median, quartiles, and range of a dataset.

Interpretation of a box-and-whisker plot (refer to Figure C.1):

1. Box: The box in the plot represents the interquartile range (IQR), which is the range between the first quartile (Q_1) and the third quartile (Q_3). The length of the box indicates the spread of the middle 50% of the data. The line within the box represents the median (Q_2) of the dataset.
2. Whiskers: The whiskers extend from the edges of the box to indicate the range of the data. The whiskers typically extend to the minimum and maximum values within a certain range of the dataset. The specific range can vary depending on the method used to draw the plot. Sometimes, it extends to the lowest and highest data points within 1.5 times the IQR from the lower and upper quartiles, respectively.
3. Outliers: Outliers are data points that fall outside the range represented by the whiskers. They are often represented as individual points or asterisks in the plot.

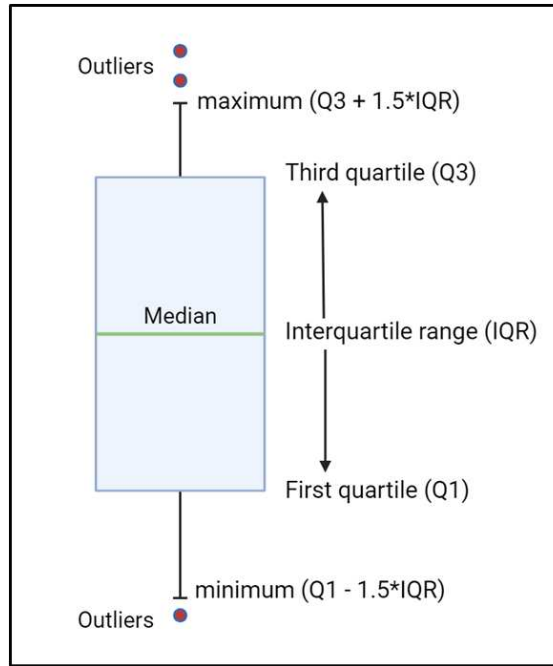


Figure C.1: A box-plot graphical representation. The box represents the interquartile range (IQR), with the median marked by a horizontal line within the box. The whiskers extend to the minimum and maximum values within 1.5 times the IQR from the lower and upper quartiles, respectively. Outliers are depicted as individual points beyond the whiskers

Box-and-whisker plots are particularly useful for comparing the distribution of a variable across different groups or categories. They allow for quick visual comparison of central tendency and variability between groups and can help identify differences or patterns in the data.

C.6 Contrast to noise ratio (CNR)

The contrast-to-noise ratio (CNR) is a measure used in various imaging modalities to assess the quality of an image. It quantifies the relative difference in contrast between two regions of interest in the image compared to the noise level present in the background of the image.

In medical imaging, while examining a particular region of interest (e.g., a tumor) against a surrounding background (e.g., healthy tissue), the CNR helps evaluate how well the feature stands out against the background noise. A higher CNR indicates a clearer contrast between the feature and the background with less interference from noise, which generally implies a better quality image for diagnostic purposes.

Mathematically, the CNR is often expressed as:

$$CNR = \frac{Contrast}{Noise} \quad (C.6)$$

Where:

- Contrast refers to the difference in signal intensity or attenuation between two ROIs.
- Noise represents the standard deviation of the background noise in the image.

A higher CNR value indicates better image quality and the effectiveness of noise reduction techniques, as it signifies a stronger contrast relative to the background noise, making it easier to distinguish important features in the image.

C.7 Model error

Model error refers to the discrepancy between the observed values and the values predicted by a statistical model. In the context of regression analysis, the model error represents the difference between the actual response values and the values predicted by the regression equation.

When performing regression analysis, the goal is to create a model that accurately captures the relationship between the independent variables and the dependent variable. However, no model is perfect, and there will always be some level of error between the predicted values and the observed values. In this thesis, this discrepancy is typically quantified by calculating the absolute difference between the calculated corrected BF value with noise and without noise with each iteration (refer to Figure 2.10).

$$Model\ error = |BF_{no\ noise} - (noise - impacted\ BFD)| \quad (C.7)$$

Where, $BF_{no\ noise}$ represents the BF value with zero noise or no noise with each iteration.

C.8 Random error

Random error, also known as random variation or stochastic error, refers to the variability in measurements that occur randomly and unpredictably. It is an inherent aspect of any measurement process and is not attributable to any systematic cause or bias. Random error affects the precision or reproducibility of measurements but does not necessarily bias the results on average when multiple measurements are taken. While individual measurements may deviate from the true value

in random directions, the average of multiple measurements tends to converge toward the true value as the sample size increases. The magnitude of random error is typically quantified using measures such as standard deviation or standard error.

In this thesis, random error calculation involves calculating the absolute difference between BF measurements obtained using two different sets of Gaussian noise with each iteration (refer to Figure 2.10).

$$\text{Random error} = |BF1 - BF2| \quad (\text{C.8})$$

Where BF1 and BF2 represents the BF measurements from different digital perfusion phantom series obtained using 2 different sets of 576 Gaussian noise levels.

C.9 Bland-Altman analysis

The Bland-Altman analysis is a statistical method used to assess the agreement or disagreement between two quantitative measurement methods or instruments. It was introduced by Martin Bland and Douglas Altman in 1986 as a graphical technique for comparing two measurement techniques without the need for assuming a gold standard (Doğan, N. Ö. 2018).

The Bland-Altman analysis involves the following steps:

1. **Data Collection:** Collect data using both measurement methods and instruments for the same set of subjects. Each subject should have paired measurements from both methods.
2. **Calculate Differences:** Calculate the differences between the paired measurements from the two methods for each subject.
3. **Calculate Mean Difference:** Calculate the mean difference (bias) between the paired measurements for the entire dataset. This represents the average disagreement between the two methods.
4. **Calculate Limits of Agreement:** Calculate the limits of agreement around the mean difference. The limits of agreement are typically defined as the mean difference plus or minus 1.96 times the standard deviation of the differences. This provides a range within which approximately 95% of the differences between the methods are expected to fall, assuming that the differences follow a normal distribution.
5. **Plot the data:** Create a scatter plot where the x-axis represents the average of the paired measurements from both methods, and the y-axis represents the differences between the paired measurements. Plot the mean difference as a horizontal line and the limits of agreement as parallel lines above and below the mean difference.

6. Interpretation: Examine the graph to assess the level of agreement between the two methods. Look for patterns or trends in the differences, as well as outliers or clusters of points. Ideally, the points should be evenly distributed around the mean difference and the limits of agreement should be narrow, indicating good agreement between the methods.

Key points about Bland-Altman analysis:

- The Bland-Altman plot provides a visual representation of the agreement between two measurement methods and allows for the identification of any systematic bias or outliers.
- It is particularly useful when comparing new measurement methods or instruments with an established gold standard or reference method.
- The Bland-Altman plot does not require assumptions about the distribution of the differences between the methods, making it robust and applicable to a wide range of datasets.
- Interpretation of the plot should consider both the magnitude and direction of the differences, as well as any clinical or practical implications of the agreement between the methods.

In general, the Bland-Altman analysis is a valuable tool for assessing the agreement between measurement methods and providing insight into the reliability and validity of quantitative measurements.

C.10 Pearson's correlation coefficient

Pearson's correlation coefficient, often denoted by r , is a statistical measure that quantifies the strength and direction of the linear relationship between two continuous variables. It was developed by Karl Pearson in the early 20th century (Sedgwick 2012).

The Pearson correlation coefficient ranges from -1 to +1, where:

1. $r = 1$: Indicates a perfect positive linear relationship. As one variable increases, the other variable increases proportionally.
2. $r = -1$: Indicates a perfect negative linear relationship. As one variable increases, the other variable decreases proportionally.
3. $r = 0$: Indicates no linear relationship between the variables.

The formula for calculating Pearson's correlation coefficient between two variables X and Y with n observations is as follows:

$$r = \frac{\sum_{i=1}^n (X_i - \bar{X})(Y_i - \bar{Y})}{\sqrt{\sum_{i=1}^n (X_i - \bar{X})^2 \sum_{i=1}^n (Y_i - \bar{Y})^2}} \quad (\text{C.9})$$

Where:

- X_i and Y_i are the individual observations of variables X and Y .
- \bar{X} and \bar{Y} are the means of variables X and Y respectively.

The numerator of the formula calculates the covariance between X and Y , which measures how the variables change together. The denominator standardizes the covariance by dividing it by the product of the standard deviations of (X) and (Y), ensuring that (r) is between -1 and +1.

Here are some key points about Pearson's correlation coefficient:

1. Strength of correlation: The magnitude of r closer to 1 or -1 indicates stronger correlations, while values closer to 0 indicate weaker correlations.
2. Direction of the correlation: The sign of r (+ or -) indicates the direction of the correlation. Positive values indicate a positive correlation (both variables increase or decrease together), while negative values indicate a negative correlation (one variable increases as the other decreases).

C.11 Coefficient of variation (COV)

The coefficient of variation (COV) is a statistical measure that expresses the relative variability of a dataset compared to its mean. It is calculated as the ratio of the standard deviation (SD) to the mean of the dataset.

The formula for calculating the COV is the following:

$$COV = \frac{\text{Standard Deviation (SD)}}{\text{Mean}} \times 100\% \quad (\text{C.10})$$

Where:

- SD is the standard deviation of the dataset.
- Mean is the mean of the dataset.

C.12 SAS (Statistical Analysis System)

SAS is a software suite developed by SAS Institute Inc., primarily used for advanced analytics, data management, and predictive analytics (SAS Institute 2024). It provides a comprehensive range of tools and capabilities for analyzing and visualizing data. SAS includes a programming language called SAS programming language (SAS/STAT, SAS/IML), which allows customizing analyses, automating repetitive

Statistics

tasks, and extending the functionality of SAS software. Overall, SAS software is widely recognized for its reliability, scalability, and versatility in handling complex data analysis tasks across various domains.

All statistical analysis methods used in this thesis were implemented using Excel 2016 (Microsoft Corporation; USA), SAS software (version 9.4, SAS Institute; USA), and MATLAB R2022a (MathWorks; USA).

The pursuit of science is a never-ending journey into the unknown, fueled by curiosity and guided by reason.

Neil Armstrong



Addition of varied noise samples during the development of noise correction algorithm

The development of a noise correction algorithm using the digital perfusion phantoms by adding 576 distinct noise levels has been explained in this thesis in section 4.2. However, the complete process involves adding varied random noise samples to the TACs to develop the noise correction algorithm.

Initially, the algorithm was implemented by adding 0 noise level to the TACs of 28 simulated datasets. Subsequently, a consistent noise level of 25 HU was introduced to the TACs. This value was selected based on meta-analysis findings from pancreatic CT perfusion studies. Additionally, to add more randomness to the data set and evaluate the effect of added random noise on perfusion measurements, 100 random noise levels samples were added to the TACs. Finally, a comprehensive evaluation involved adding 576 random noise samples to evaluate the effect on the TACs and rectify the perfusion measurements.

Evaluation of these TACs affected by noise and calculation of perfusion parameters were performed by representing these TACs affected by noise as digital images. Each digital image consisted of a 512 x 512 pixel matrix with 512 x 504 pixels of size 4 x 4, each containing the TACs, and an additional 50 x 8 pixel region on the right side containing the AIF (refer to Figure D.1). The square regions of size 4 x 4 pixels containing TACs were determined based on the smoothing strength of the CT perfusion software used. When setting the parameter for smoothing strength to 0 mm, a size of 4-by-4 pixels was identified as the minimum dimension that would yield pixels containing the expected results (i.e., the 2-by-2 patch in the middle of the region will yield values matching ground truth) undisturbed by filtering when

Addition of varied noise samples during the development of noise correction algorithm

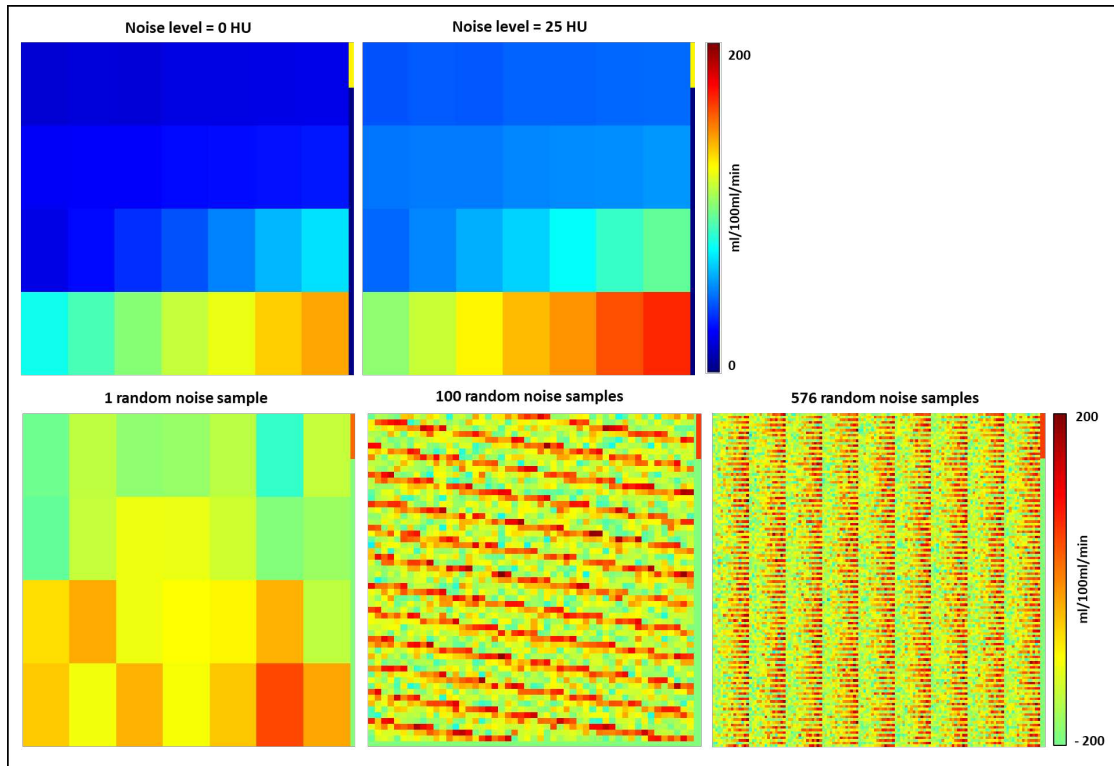


Figure D.1: Digital perfusion phantom images generated by adding varied noise samples to TACs during the process of development of the noise correction algorithm

evaluating a digital perfusion phantom (Skornitzke et al. 2019).

Finally, a single digital perfusion phantom series is comprised of 34 such digital images made up of 16128 TACs (28 sets of ground truth values * 576 random noise samples). All phantom images were stored in the DICOM format. Figure D.1 shows the digital perfusion phantom images generated during the process of development of noise correction algorithm.

The greatest enemy of knowledge is not ignorance, it is the illusion of knowledge.

Stephen Hawking



Additional approach to obtain the optimized acquisition time for FPA - an extension of FPA1

In this thesis, FPA1 was implemented considering the first volume scan at t_{base} , and the second scan at the peak of TAC (t_{peak}) as explained in Section 2.7.1. To optimize the acquisition timing of the FPA1 approach, additional second volume scans were captured consecutively one and two scans or time-points before t_{peak} (i.e. $t_{\text{peak}} - 1$ which refers to 1.5 seconds before t_{peak} and $t_{\text{peak}} - 2$ which represents 3 seconds before t_{peak} as the temporal spacing is 1.5 seconds for our dataset used in this thesis) and one and two scans after t_{peak} (i.e. $t_{\text{peak}} + 1$ which refers to 1.5 seconds after t_{peak} , $t_{\text{peak}} + 2$ which refers to 3 seconds after t_{peak} in this thesis) apart from t_{peak} . MSM perfusion maps were also computed considering these time-points for validation.

The mean \pm SD BF values for carcinoma (ROI2) and parenchyma (ROI3) tissue were calculated at all five time points, and the results are shown in Table E.1. The mean BF values were observed to be slightly higher with this FPA approach compared to MSM at all five time points. COV between BF values at five time points was higher in this approach (carcinoma: 22.3, parenchyma: 13.4) compared to MSM (carcinoma: 4.1, parenchyma: 2.1). Furthermore, this FPA model exhibits a favorable correlation with MSM for combined carcinoma and parenchyma tissue at all five time-points, with the highest correlation ($r = 0.83$) observed at t_{peak} . However, regrettably, determining exact acquisition times at maximum TAC remains a challenge with this FPA approach, making it unsuitable for clinical applications.

Model	Tissue type	Acquisition timing of second volume scan					COV (%)
		t _{peak-2}	t _{peak-1}	t _{peak}	t _{peak+1}	t _{peak+2}	
Circular ROI blood flow measurement (ml/100ml/min)							
FPA	Carcinoma	52.2	64.9	70.2	91.1	88.6	22.3
		± 28.7	± 36.2	± 48.9	± 68.5	± 57.5	
	Parenchyma	164.3	175.9	194.1	217.6	225.7	13.4
		± 84.8	± 88.0	± 91.7	± 99.0	± 126.3	
	T-test (p value)	<0.0001	<0.0001	<0.0001	0.0003	0.0006	
MSM	Carcinoma	43.1	44.0	42.0	46.0	41.5	4.1
		± 24.9	± 25.4	± 24.8	± 28.7	± 24.8	
	Parenchyma	109.1	108.0	106.8	105.0	104.5	2.1
		± 44.4	± 42.6	± 41.5	± 41.5	± 41.6	
	T-test (p value)	<0.0001	<0.0001	<0.0001	<0.0001	<0.0001	
Pearson's correlation (r)		0.73	0.79	0.83*	0.78	0.67	

Table E.1: Mean \pm SD blood flow (BF) values of carcinoma (ROI2) and parenchyma (ROI3) tissue for circular ROI using additional FPA and MSM all five acquisition time-points. Circular ROIs were used to indicate the respective tissues with a high degree of confidence. The p-value of student's t-test showed a significant difference between carcinoma and parenchyma tissue. The correlation value marked with an asterisk showed the highest correlation at the peak of TAC t_{peak}

Curriculum Vitae

PERSONAL INFORMATION

Name	Neha Vats
Date of Birth	29 July 1993
Place of Birth	Haryana, India
Nationality	Indian
Marital Status	Unmarried

UNIVERSITY

02/2020 - present	PhD-student in Medical Physics (cand. sc. hum.) at the Diagnostic and Interventional Radiology (DIR), University Hospital Heidelberg, Heidelberg, Germany
07/2017 - 06/2019	Masters in Biomedical Engineering (Gold Medalist) at
(07/2018 - 06/2019)	Indian Institute of Technology, Delhi, India
(07/2017 - 06/2019)	National Institute of Technology, Kurukshetra, Haryana, India
	Thesis title: Brain Tumor Segmentation and Classification using Multi-parametric MRI
07/2012 - 05/2016	Bachelors in Electronics Instrumentation and Control at YMCA University of Science and Technology, Haryana, India
	Master's entrance exam: GATE (Graduate Aptitude Test in Engineering) for a scholarship

WORK EXPERIENCE

07/2019 - 01/2020	Research Associate at Indian Institute of Technology, Delhi, India
05/2018 - 06/2018	Summer Research Fellowship at Indian Institute of Technology, Delhi, India
06/2016 - 08/2016	Internship at Byju's Learning, Bangalore, India
06/2015 - 12/2015	Internship at Panipat Thermal Power Station, Haryana, India

EDUCATION

04/2009 - 03/2011	Senior secondary level Modern Vidya Niketan School Haryana, India Degree certificate - University Entrance Qualification (23/05/2011) University entrance exam: AIEEE (All India Engineering Entrance Examination)
04/2007 - 03/2009	Secondary level Mahadev Desai Public School Haryana, India Degree certificate - Senior Secondary Entrance Qualification (26/05/2009)
04/1999 - 03/2007	Primary level Mahadev Desai Public School Haryana, India

Acknowledgements

Pursuing a doctorate and writing a doctoral thesis is nothing short of a rollercoaster journey, and it requires enormous commitment with many ups and downs and important decisions along the way. Therefore, I would like to express my sincere gratitude to all those who have supported, guided, and accompanied me along this beautiful rollercoaster journey. Firstly, my special thanks go to my doctoral father, Dr. med. Hans-Ulrich Kauczor, for giving me the incredible opportunity to work with him and his team and always being very supportive and encouraging. I want to thank him especially for the very honest and open conversations, which always gave me faith to continue, and for the awesome working environment that he creates within his group. Furthermore, I would like to express my gratitude to Dr. Wolfram Stiller, my doctoral advisor, for consistently offering invaluable feedback, suggestions, and highly beneficial technical recommendations. I am also grateful to him for overseeing my vacation arrangements and assisting me throughout the university enrollment process.

My deepest appreciation is reserved for my doctoral supervisor, Dr. Stephan Skornitzke, without whom this doctoral thesis would not have been made possible. He was a pillar through my doctoral process, always supporting and encouraging me personally and professionally. He is the driving force towards the completion of this thesis. From him I have learned invaluable lessons, notably the importance of maintaining patience in all circumstances. Words cannot adequately express the depth of my gratitude towards him. I could not have imagined having a better advisor. I consider myself lucky as I got the opportunity to work with him.

In addition, I express my gratitude to Dr. Philipp Mayer for his invaluable contributions of clinical insights to my publications, which greatly enriched their content and quality. Additionally, I would like to convey my heartfelt appreciation to the entire DIR Department. This includes, but is not limited to, Dr. Stackelberg, Dr. Miklankova, Dr. Sowade, Ms. Tarallo, and Ms. Ginschel, for their dedicated management of the department and our research seminars during my doctoral tenure. I extend a particular note of gratitude to Ms. Ginschel for her assistance with personal health issues. Additionally, I am grateful to all my labmates for engaging in fruitful discussions, experiences and sharing enjoyable moments throughout these past years.

My thanks goes to all of my friends for their attentive listening, valuable advice, and unwavering support throughout this journey. Special thanks go to those who

stood by me during the most challenging phase of my doctorate, namely Kanika and Kritika. Although their presence and encouragement were online, it was invaluable, and words cannot adequately express my appreciation for their unwavering support. Now, a special acknowledgment to my friend Rohith for gracefully handling my mood fluctuations throughout the writing process and lightening my mood within a second.

Last but not least, I would like to thank my beloved parents, Hukam and Pushpa, who gave everything they had to ensure that I can live my dreams. They have blessed me with everlasting encouragement, untiring support, and understood my goals and aspirations. Their patience and sacrifices will always be my inspiration to achieve more and more in life. My heartfelt regard goes to my lovely grandmother Angoori and I fondly remember my late grandfather Jayanti, whose love remains invaluable to me. A special thanks goes out to my brother, sister and other family members for their love, encouragement, and any kind of help. I consider myself fortunate to belong to such a loving and supportive joint family. Above all, I wish to express my gracious faithfulness to the Almighty God Shiva, for making me feel His presence every time and for choosing me to believe in Him. As I do believe "We do not choose Him, He chooses us". Without his blessings, this achievement would not have been possible.

This research was supported by the German Federal Ministry of Education and Research (BMBF) under grant number 031L0163.

Eidesstattliche Versicherung

1. Bei der eingereichten Dissertation zu dem Thema "**Optimization and Standardization of computed tomography perfusion and development of low radiation exposure CT perfusion alternative for clinical applications in oncologic imaging**" handelt es sich um meine eigenständig erbrachte Leistung.
2. Ich habe nur die angegebenen Quellen und Hilfsmittel benutzt und mich keiner unzulässigen Hilfe Dritter bedient. Insbesondere habe ich wörtlich oder sinngemäß aus anderen Werken bernommene Inhalte als solche kenntlich gemacht.
3. Die Arbeit oder Teile davon habe ich bislang nicht an einer Hochschule des In- oder Auslands als Bestandteil einer Prüfungs- oder Qualifikationsleistung vorgelegt.
4. Die Richtigkeit der vorstehenden Erklärungen bestätige ich.
5. Die Bedeutung der eidesstattlichen Versicherung und die strafrechtlichen Folgen einer unrichtigen oder unvollständigen eidesstattlichen Versicherung sind mir bekannt. Ich versichere an Eides statt, dass ich nach bestem Wissen die reine Wahrheit erkläre und nichts verschwiegen habe.

Heidelberg, 2024

Neha Vats

Place, Date

doctoral candidate's signature